ISSN en trámite

Geofísica Internacional

Revista Trimestral Publicada por el Instituto de Geofísica de la
Universidad Nacional Autónoma de México

México
Volume 60 Number 2
April - June
2021

— Geofísica Internacional —

Dr. José Luis Macías Vázquez
Director of Instituto de Geofísica

Dra. Vanessa Magar Brunner
President of Unión Geofísica Mexicana

Editor Chief
Dr. Servando De la Cruz-Reyna
Instituto de Geofísica, UNAM
sdelacrr@geofisica.unam.mx

Technical Editor
Mtra. Andrea Rostan Robledo
Instituto de Geofísica, UNAM
arostan@igeofisica.unam.mx

Editorial Board
Donald Bruce Dingwell
Earth and Environment
Ludwig Maximilian University of Munich, Germany

Eric Desmond Barton
Departamento de Oceanografía
Instituto de Investigaciones Marinas, Spain

Jorge Clavero
Amawta Consultores, Chile

Gerhardt Jentzsch
Institut für Geowissenschaften
Friedrich-Schiller-Universität Jena, Germany

Peter Malischewsky
Institut für Geowissenschaften
Friedrich-Schiller-Universität Jena, Germany

François Michaud
Géosciences Azur
Université Pierre et Marie Curie, France

Olga Borisovna Popovicheva
Scobeltzine Institute of Nuclear Physics
Moscow State University, Rusia

Jaime Pous
Facultad de Geología
Universidad de Barcelona, Spain

Joaquín Rui
UA Science
University of Arizona, United States

Angelos Vourlidas
Solar Physics Branch
NASA Goddard Space Flight Center, United States

Théophile Ndougsa Mbarg
Department of Physics
University of Yaounde I, Cameroon

Associate Editors
José Agustín García Reynoso
Atmospheric Science Centro de Ciencias de la Atmósfera UNAM, Mexico

Tereza Cavazos
Atmospheric Science
Departamento de Oceanografía Física CICESE, Mexico

Dante Jaime Morán-Zenteno
Geochemistry
Instituto de Geología, UNAM, Mexico

Margarita López
Geochemistry
Instituto de Geología UNAM, Mexico

Avto Gogichaisvilii
Geomagnetism And Paleomagnetism
Instituto de Geofísica UNAM, Mexico

Jaime Urrutia-Fucugauchi
Geomagnetism And Paleomagnetism
Instituto de Geofísica, UNAM, Mexico

Felipe I. Arreguín Cortés
Hydrology
Instituto Mexicano de Tecnología del Agua IMTA, Mexico

William Lee Bandy
Marine Geology And Geophysics
Instituto de Geofísica UNAM, Mexico

Fabian García-Nocetti
Mathematical And Computational Modeling
Instituto de Investigaciones en Matemáticas Aplicadas y en Sistemas UNAM, Mexico

Graciela Herrera-Zamarrón
Mathematical Modeling
Instituto de Geofísica, UNAM, Mexico

Ismael Herrera Revilla
Mathematical And Computational Modeling
Instituto de Geofísica UNAM, Mexico

Rene Chávez Segura
Near-Surface Geophysics
Instituto de Geofísica UNAM, Mexico

Juan García-Abdeslem
Near-Surface Geophysics
División de Ciencias de la Tierra CICESE, Mexico

Alec Torres-Freyermuth
Oceanography
Instituto de Ingeniería, UNAM, Mexico

Jorge Zavala Hidalgo
Oceanography
Centro de Ciencias de la Atmósfera UNAM, Mexico

Shri Krishna Singh
Seismology
Instituto de Geofísica, UNAM, Mexico

Xyoli Pérez-Campos
Seismology
Servicio Sismológico Nacional, UNAM, Mexico

Blanca Mendoza Ortega
Space Physics
Centro de Ciencias de la Atmósfera, UNAM, Mexico

Inez Staciarini Batista
Space Physics
Pesquisador Senior Instituto Nacional de Pesquisas Espaciais, Brazil

Roberto Carniel
Volcanology
Laboratorio di misure e trattamento dei segnali DPIA - Università di Udine, Italy

Miguel Moctezuma-Flores
Satellite Geophysics
Facultad de Ingeniería, UNAM, Mexico

Assistance
Elizabeth Morales Hernández,
Management
eliedit@igeofisica.unam.mx

GEOFÍSICA INTERNACIONAL, Año 60, Vol. 60, Núm. 2, abril - junio de 2021 es una publicación trimestral, editada por la Universidad Nacional Autónoma de México, Ciudad Universitaria, Alcaldía Coyoacán, C.P. 04150, Ciudad de México, a través del Instituto de Geofísica, Circuito de la Investigación Científica s/n, Ciudad Universitaria, Alcaldía Coyoacán, C.P. 04150, Ciudad de México, Tel. (55)56 22 41 15. URL: http://revistagi.geofisica.unam.mx, correo electrónico: revistagi@igeofisica.unam.mx. Editora responsable: Andrea Rostan Robledo. Certificado de Reserva de Derechos al uso Exclusivo del Título: 04-2022-081610251200-102, ISSN: en trámite, otorgados por el Instituto Nacional del Derecho de Autor (INDAUTOR). Responsable de la última actualización Saúl Armendáriz Sánchez, Editor Técnico. Fecha de la última modificación: 31 de marzo 2021, Circuito de la Investigación Científica s/n, Ciudad Universitaria, Alcaldía Coyoacán, C.P. 04150, Ciudad de México.

El contenido de los artículos es responsabilidad de los autores y no refleja el punto de vista de los árbitros, del Editor o de la UNAM. Se autoriza la reproducción total o parcial de los textos siempre y cuando se cite la fuente completa y la dirección electrónica de la publicación.

Esta obra está bajo una Licencia Creative Commons Atribución-NoComercial-SinDerivadas 4.0 Internacional.

Geofísica Internacional
Vol. 60, Núm. 2, abril-junio de 2021

Contents

Original paper

GEOPHYSICAL-STRUCTURAL FRAMEWORK IN A MINERALIZED REGION OF NORTHWESTERNMOST CAMAQUÃ BASIN, SOUTHERN BRAZIL

Henrique Garcia Pereira[1*], Francisco José Fonseca Ferreira[2], César Augusto Moreira[3] and Vinicius Antunes Ferreira da Silva[4]

Received: July 28, 2020; accepted: January 1, 2021; published online: April 1, 2021

RESUMEN

Los mapas magnéticos y gravimétricos (aéreos y/o terrestres) suministran información importante sobre la distribución espacial de las fuentes del sustrato geológico, las cuales normalmente tienen propiedades físicas y geometrías diferentes. Estas fuentes también pueden estar localizadas a distintas profundidades, complicando la identificación de las correspondientes estructuras geológicas. Técnicas de filtrado y de realce de anomalías potenciales, pueden ser utilizadas para realzar ciertas características de interés (como el centro y el borde de las fuentes), para remover aquellas características asociadas a ruidos, para separar las anomalías de las fuentes superficiales y profundas, así como estimar sus profundidades. En este trabajo se analizan los resultados de la utilización de técnicas de realce y estimación de profundidad de las fuentes con datos geofísicos aéreos y terrestres potenciales, con el objetivo de delinear una imagen estructural del subsuelo en un área con dos ocurrencias de cobre en el límite noroeste, entre las rocas del Escudo Sul-Riograndense y la Cuenca del Camaquã. Los resultados confirman estructuras que han sido reconocidas previamente y revelan otras estructuras geológicas que integran una malla estructural interconectada, cuya profundidad, estimada por las soluciones de Euler, alcanzan los 170 m. Esta configuración sugiere una probable conexión entre las mineralizaciones de cobre observadas en los afloramientos, separados por un intervalo de 2,300 m.

PALABRAS CLAVE: Magnetometría, Gravimetría, Lineamientos, Escudo Sul-Riograndense, Ocurrencias de Mineralizaciones de Cobre.

ABSTRACT

Airborne and ground magnetic and gravimetric maps provide important information about the spatial distribution of causative sources in the geological substrate. These sources normally have different physical properties and geometric shapes and are located at different depths, making it difficult to identify the geological features that correspond to the sources. Filtering and enhancement techniques can be used to highlight features in potential field anomalies (such as center and edges of sources). Also, these techniques remove associated noise, isolate shallow from deep sources, and estimate depths. We applied enhancement and depth estimation techniques

*Corresponding author: ique_garcia@hotmail.com

[1] Laboratory for Research in Applied Geophysics and Geology Graduate Program, Department of Geology, Federal University of Paraná, Brazil

[2] Laboratory for Research in Applied Geophysics, Department of Geology, Federal University of Paraná, Paraná, Brazil.

[3] Department of Applied Geology, Geosciences and Exact Sciences Institute, São Paulo State University (UNESP), São Paulo, Brazil.

in airborne and ground potential field data to delineate a subsurface structural framework of two copper occurrences (Victor Teixeira and Capão Grande) in the northwestern border of Camaquã Basin with the Sul-Riograndense Shield. Our results confirmed previously recognized structures and revealed an interconnected structural framework, which has an estimated depth of 170 m by Euler solutions. This configuration suggests a possible connection between the two mineralization outcrops, which are separated by a distance of 2,300 m.

KEY WORDS: Magnetometry, Gravimetry, Lineaments, Sul-Riograndense Shield, Cupriferous Mineralizations.

INTRODUCTION

Geophysics has been applied in numerous studies to establish geological and tectonic compartmentalization in the last decades, as well as distinguishing lithotypes and identifying structures and lineaments, especially in inaccessible areas (Hallinan *et al.,* 1993; Fernandes *et al.,* 1995; Nogueira *et al.,* 2004; Carvalho *et al.,* 2006; Barbuena *et al.,* 2013; Ramos *et al.,* 2014; Castro and Ferreira, 2015; Gastal *et al.,* 2015; Kosaroglu *et al.,* 2016; Campos *et al.,* 2017; Araffa *et al.,* 2018; Weihermann *et al.,* 2018; Osinowo and Abdulmumin, 2019; Alatorre-Zamora *et al.*, 2020).

In most of these works, the qualitative geological-structural interpretation is usually facilitated when enhancement methods are applied. These emphasize certain characteristics of the geophysical data (primarily those related to potential fields). Several anomaly enhancement methods based mainly on the relationships between the derivatives of the magnetic and gravimetric fields have been published: vertical derivative (GZ – Evjen, 1936), analytic signal amplitude (ASA – Nabighian, 1972; Roest *et al.,* 1992), total horizontal gradient (THDR - Cordell and Grauch, 1985), tilt angle (TDR - Miller and Singh, 1994), total horizontal gradient of the tilt angle (TDR_THDR - Verduzco *et al.,* 2004), horizontal tilt angle (TDX - Cooper and Cowan, 2006), Theta Map (THETA - Wijns *et al.,* 2005) and tilt angle of the horizontal gradient (TAHG - Ferreira *et al.,* 2013). There are also quantitative methods used to estimate the depth and width of causative sources, such as Euler deconvolution (Thompson, 1982) and the Signum transform (de Souza and Ferreira, 2012, 2013, 2015; Oliveira *et al.,* 2015, 2017).

The purpose of this paper is to present the application of qualitative and quantitative analyses of airborne and ground potential data to infer the structural mapping of subsurface and the configuration of cupriferous mineralizations. Although the Victor Teixeira and Capão Grande occurrences have already been the subject of geophysical studies (Moreira and Ilha, 2011; Pereira *et al.,* 2016; Côrtes *et al.,* 2016; Pereira *et al.,* 2017; Côrtes *et al.,* 2019; Bitencourt *et al.,* 2020), this is the first study to our knowledge where a geophysical-structural framework is presented for the region.

STUDY AREA AND GEOLOGICAL SETTING

The study area is located on the northwestern limit of the Caçapava do Sul municipality, Rio Grande do Sul state central region, Brazil (Figure 1a). The mining activity has great importance in the region of Caçapava do Sul due to numerous prospects, occurrences, and recognized polymetallic deposits. For example, the exploration of copper and gold that dates to the beginning of the 20th century (Ronchi and Lobato, 2000).

The geological regional context of the area is demarcated by a portion of contact between the Sul-Riograndense Shield and the Camaquã Basin (Figure 1b). The Sul-Riograndense Shield comprises the southern segment of the Mantiqueira Province, which encompasses 65,000 km^2

of the south-central Rio Grande do Sul state. This shield is characterized by a wide spectrum of Precambrian igneous and metamorphic rocks, whose genesis is related to crust formation processes that occurred during the Trans-Amazonian/Eburian (Paleoproterozoic, 2.5 to 2.0 Ga) and Brasiliano/Pan-African (Neoproterozoic, 900-540 Ma) orogenic cycles (Almeida *et al.,* 1981; Soliani Jr, 1986; Brito Neves and Cordani, 1991; Babinski *et al.,* 1996; Hartmann *et al.,* 2000). Regional structures of NE-SW, NW-SE, and N-S trending separated this shield in the Taquarembó, São Gabriel, Santana da Boa Vista, and Pelotas domains (Borba *et al.,* 2006; CPRM, 2007; Borba *et al.,* 2008).

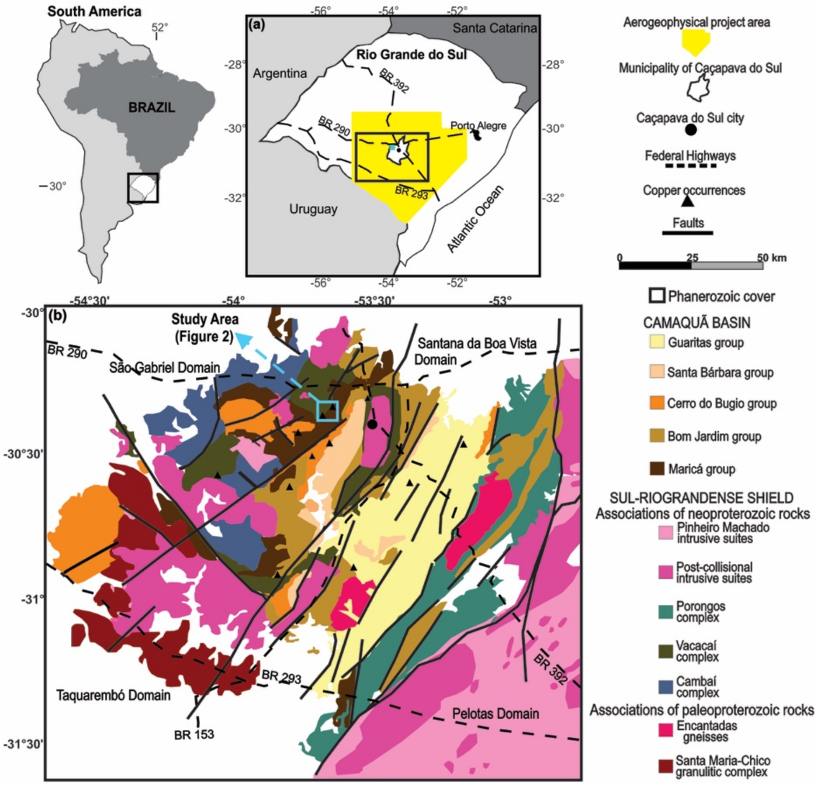

Figure 1. Location map indicating the main access roads (a) and the geological regional map of the study area (b) based on Almeida *et al.* (2005) and Borba *et al.* (2006).

The Camaquã Basin, which has the Sul-Riograndense Shield as basement, is composed of sedimentary and volcanogenic sequences (dated from 620 to 450 Ma) and has 10,000 m of thickness in an area of approximately 32,000 km^2 in the main trend, i.e. N30E (Almeida *et al.,* 1981; De Ros *et al.,* 1994; Fragoso-Cesar *et al.,* 2000; Paim *et al.,* 2000; Teixeira *et al.,* 2004; Almeida *et al.,* 2010). These sequences do not show significant features of regional metamorphism and are delimited by high-angle major faults with NNE-SSW direction and basement highs, such as Caçapava do Sul to the west, and Serra das Encantadas to the east (Almeida *et al.,* 2009).

According to Paim *et al.* (2000), Janikian *et al.* (2003), CPRM, (2007) and Almeida *et al.* (2010), the Camaquã Basin filling sequence can be subdivided into five main groups: Maricá (fluvial sandstones and marine fine-grained sandstones), Bom Jardim (lacustrine sandstones; conglomerates, rhythmites, and mudstones; intermediate, basic and acid volcanic and volcanoclastic rocks), Cerro do Bugio (volcanoclastic rocks and acidic volcanic), Santa Bárbara (alluvial sandstones, conglomerates, and rhythmites), and Guaritas (alluvial sandstones and conglomerates; aeolian sandstones). These groups are separated by angular unconformity and are also subdivided into formations, dominantly limited by unconformities.

Locally, the geological context in the study area (Figure 2a) is composed of outcropped rocks from the Vacacaí Metamorphic Complex (Sul-Riograndense Shield), the Passo da Promessa and Arroio América Formations (Maricá Group) and the Acampamento Velho Formation (Cerro do Bugio Group). Also, the area presents the Victor Teixeira and Capão Grande cupriferous occurrences and E-W, NE-SW and NW-SE trending faults.

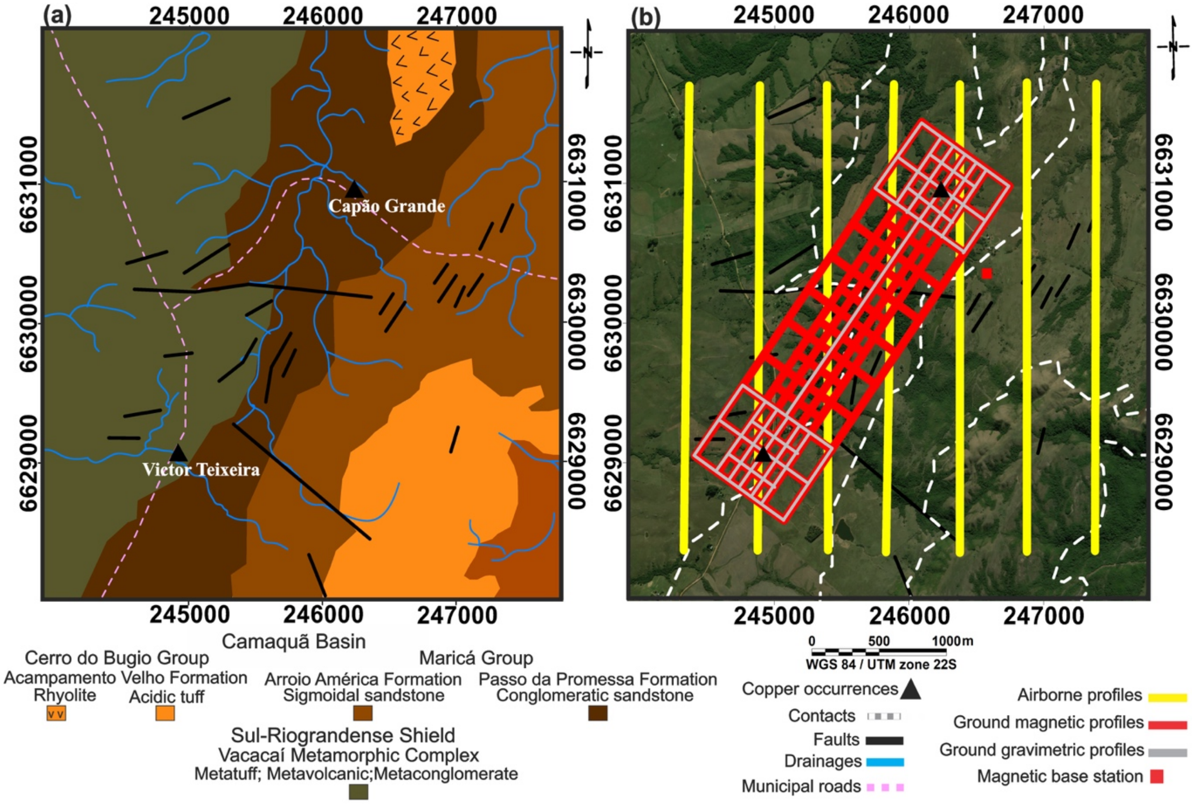

Figure 2. Geological local map of study area (a) based on CPRM (1995) and the configuration of potential field data profiles (b). Note that the ground gravimetric lines are situated over the ground magnetic ones.

The Vacacaí Metamorphic Complex (750 Ma) is constituted by a wide association of volcanic, volcanoclastic, and sedimentary rocks, which were metamorphosed primarily by younger post-tectonic Brazilian granitic intrusions into greenschist facies, phyllites, quartzites, marbles, hornblende schists, and chloritic schists, as well as magnesian sequences (Machado *et al.,* 1990; CPRM, 2000). The complex has four main deformation phases recognized by regional structures. The first three phases generated coaxial faults and folds with NE-SW oriented axes which plunge 50° to the northwest. The first two events are expressed in a tangential movement while the third is characterized by shear. The last phase of deformation resulted in faults and folds with axes oriented to NW-SE and E-W, which were produced by a strong reorientation in the stress system (Koppe, 1990; CPRM, 1995; Remus *et al.*, 1999).

In this unit, fine-grained yellowish-cream-gray quartzites with foliated texture were identified. These rocks are highly fractured and fracture-filled with quartz veins (Figure 3a). Also, subordinate metapelites outcropped in the area (Figure 3b). Both quartzites and metapelites denote low-grade metamorphism features.

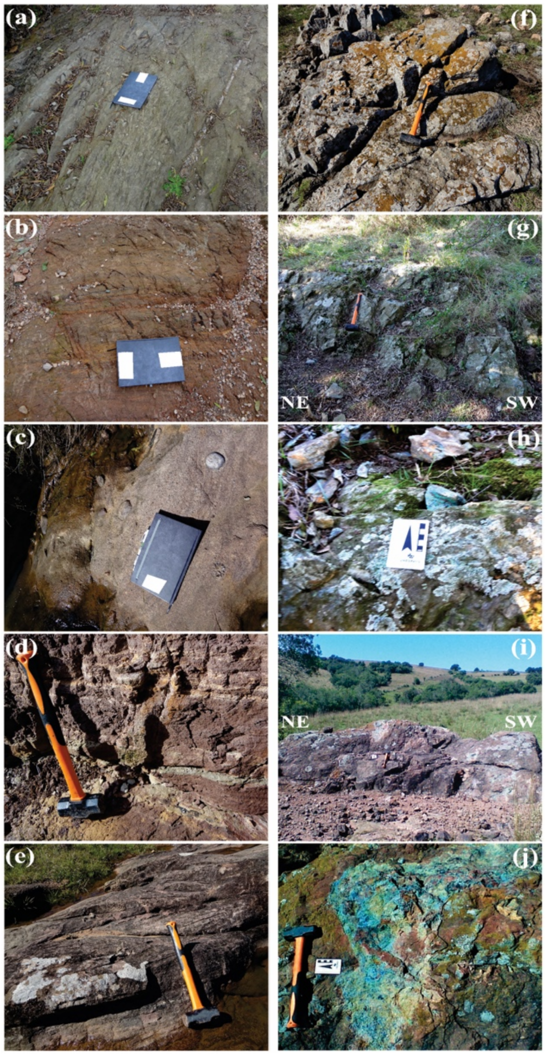

Figure 3. Main lithotypes found in the study area: (a) quartzites; (b) metapelites; (c) conglomeratic sandstones; (d) intercalations of sandstones and pelites; (e) trough cross-stratification; (f) rhyolites; (g) outcrop of Victor Teixeira copper occurrence; (h) malachite in Victor Teixeira; (i) outcrop of Capão Grande copper occurrence; and (j) azurite and malachite in Capão Grande.

The Passo da Promessa Formation corresponds to the bottom unit of the Maricá Group, dominated by cross-stratified sandstones and subordinate conglomerate lenses, interpreted as deposits of river plains of braided channels. The Arroio América Formation is the top unit of the Maricá Group and includes sandstones and conglomeratic facies generated in system of river plains of braided channels, associated with distal portions of alluvial fans. These formations were affected by a compressive tectonic event originating folds with low and high angle faults generating drags and interstrata displacements, and small sheath folds along low-angle fault planes leading to the interpretation of layer duplication (Pelosi and Fragoso-Cesar, 2003).

The Passo da Promessa Formation unit presents medium to coarse-grained reddish-brown and yellowish-white sandstones, often conglomeratic, poorly sorted, angular to subangular grains, often with rounded quartz pebbles, granites, and metamorphic rocks (Figure 3c). There are also sandstones intercalated with thin layers of pelites (Figure 3d) and trough cross-stratification of metric to decametric thickness is common (Figure 3e).

The Acampamento Velho Formation is the top unit of the Cerro do Bugio Group and represents the record of sodium alkaline affinity volcanism related to a post-orogenic extensional tectonic environment of approximately 700 m thick (Sommer *et al.,* 1999; Janikian *et al.,* 2005). This explosive-effusive volcanism is predominantly acid and formed in a subaerial environment associated with lavas and dikes of basic composition (Sommer *et al.,* 2011; Matté *et al.,* 2012). Outcrops of elongated tabular grayish-brown rhyolites oriented in the NE direction, which were described in the Acampamento Velho Formation (Figure 3f), were frequently observed in the sandstones of the Passo da Promessa Formation, near the Victor Teixeira occurrence (see Figure 2a). The rhyolites emplaced the weakened contact zone between the basement and the Camaquã Basin during the post-orogenic magmatic events (Borba *et al.,* 2007).

The Victor Teixeira cupriferous occurrence, hosted at the Metamorphic Complex Vacacaí (see Figure 2a), is characterized by an outcrop in the NE-SW direction that presents 5 m length and 2 m width (Figure 3g). Chlorite-quartz-sericite schists and sericite-chlorite-quartz schists with gray to greenish-gray colors constitute the outcropping rocks. In addition, small impregnations of malachite [$Cu_2(CO_3)(OH)_2$] were observed in fractures and in the interfoliar spaces (Figure 3h).

The Capão Grande occurrence is present in the Passo da Promessa Formation, the bottom unit of the Maricá Group in the Camaquã Basin (see Figure 2a). This mineralization is characterized by an outcrop in the NE-SW direction, showing 19 m in length and 10 m in width (Figure 3i), composed of intensely fractured medium-grained and reddish-brown arkosic sandstones. These sandstones host azurite [$Cu_3(CO_3)_2(OH)_2$] and malachite [$Cu_2(CO_3)(OH)_2$], which mainly fill fractures (Figure 3j).

The literature on the origin of several prospects, occurrences and deposits of metallic minerals (Au, Ag, Cu, Pb and Zn) present and the Camaquã Basin shows contrasting interpretations due to the variety of models proposed. The most recent explanation for their origin is that they are associated with a magmatic-tectonic system developed in the post-collisional period of the Dom Feliciano Belt, at the end of the Brasiliano Cycle. The plutono-volcanic events recorded in the basin would have acted as thermal sources in the generation of epithermal systems. In addition, these events may be responsible for the circulation of paleofluids and for the remobilization of metals from country rocks and their later concentration (Remus *et al.,* 2000; Mexias *et al.,* 2007; Toniolo *et al.,* 2007; Fontana, 2016).

The structural control of those important concentrations of metallic minerals is intrinsically associated with the tectonic episodes of generation and deformation of the Camaquã Basin over the Sul-Riograndense Shield. According to Almeida *et al.* (2010), two paleostress fields, related to forming tectonic events, and three later ones were recognized, which were associated with deforming tectonic events. The two first fields were associated with ENE-trending distension and ENE-trending compression while the others were related to NW-oriented distension, NW-oriented compression, and NE-oriented distension. Also, the first paleostress corresponds to the N20-30E trend Irapuá Fault (Ribeiro *et al.,* 1966) while the second is associated with the N50-60W oriented Cerro da Vigia Fault (Ribeiro, 1970).

MATERIAL AND METHODS

The airborne magnetic data used in the present research was acquired and processed by Lasa Prospecções S/A for the Geological Survey of Brazil (CPRM, 2010). The Aerogeophysical Rio Grande do Sul Project covered an area of approximately 75,600.00 km^2 and its survey lines were spaced 500 m (north-south oriented) while its control lines have a spacing of 10 km. The average nominal ground clearance was 100 m. The magnetic field was acquired using a Scintrex CS-2 cesium magnetometer that uses a GPS navigation system with 12-channel receivers and a TRIMBLE AgGPS 132 differential correction model. The along-line sample interval was 0.1 s, which represented a spatial sampling of approximately 6 m.

The limits of the Aerogeophysical Rio Grande do Sul Project is illustrated in Figure 1a and the flight-lines used in the 16 km^2 of study are shown in Figure 2b. The length of each of the seven lines was 3,200 m.

The ground magnetic data consisted of 1,258 measurements acquired in a parallel and perpendicular arrangement to the cupriferous occurrences of Victor Teixeira and Capão Grande (Figure 2b). These profiles were collected using a sampling interval of 25 m and they present different lengths, e.g. 400 m, 800 m, and 2,925 m. Two GSM-19 (GEM SYSTEMS) proton precession magnetometers were used for the ground survey where one of them acted as a base station to assess the daily magnetic variation. In addition, the readings were defined according to the magnetic datum (22,475 nT) obtained from the National Oceanic and Atmospheric Administration (NOAA) for the center of the study area.

The acquisition of ground gravimetric data was restricted to two smaller areas around the copper occurrences and along a NE-SW profile that connects them (Figure 2b). Gravity acceleration measurements were spaced 25 m in the profiles that crosscut the mineralized outcrops and 50 m along the others. A total of 441 stations were acquired using a Scintrex Autograv CG-5 gravimeter.

The procedure adopted in obtaining the gravimetric data was to use a known base station to start the survey, then proceeding to the stations scheduled and at the end of day measuring at the initial base station. The Autograv CG5 gravimeter was configured so that measurements were sampled at both the base station and stations of interest after a 90 s cycle of continuous readings.

The Main Church of Caçapava do Sul was used as a reference base station. This station, which is a member of the Fundamental Gravity Network of Brazil, has the following properties: absolute gravity of 979,274.670 mGal, altitude of 444.895 m, and UTM coordinates of 260,050.493 X and 6,621,240.062 Y.

The georeferencing of gravimetric stations was performed using two GPS/GLONASS/SBAS L1/L2 receivers, ProMark 700 models, from Spectra Precision. These models were developed for use in Real-time Kinematic Network (RTK) and present Global Satellite Navigation System (GNSS) with 200 channels achieving horizontal and vertical accuracies of 10 mm and 20 mm, respectively.

The Geological Survey of Brazil made the data of the Rio Grande do Sul Shield aerogeophysical project (CPRM, 2010) available in the ASCII format (.xyz). In addition, the survey data already includes routine magnetic corrections (parallax error; removal of diurnal variations; leveling and microleveling of profiles, and subtraction of the International Geomagnetic Reference Field - IGRF). Therefore, the processing carried out included clipping the area of interest and to grid its database in the dimensions 125 m x 125 m (equivalent to 1/4 of the spacing between flight lines), using the bidirectional interpolation method (Reeves, 2005; Isles and Rankin, 2013).

Regarding the ground magnetic data processing, after removal of spurious data, the magnetic field was corrected for diurnal variations and the IGRF was subtracted (Luiz and Silva, 1995; Milsom, 2003; Dentith and Mudge, 2014). In addition, the diurnal correction calculation was performed in the GEMLink software and the IGRF subtraction (according to the World Magnetic Model corrected in 2018) using the Oasis Montaj program.

The ground gravimetric data were also reduced according to standard procedures in the literature, such as instrumental drift, tidal effects, latitude, altitude, and terrain corrections, as well as the calculation of the free-air and Bouguer anomalies (Telford *et al.,* 1990; Kearey *et al.,* 2002; Lowrie, 2007; Hinze *et al.,* 2013). The free-air and Bouguer anomalies were defined according to the latitude equation of Heiskanen and Moritz (1967) and an average crustal density of 2.67 g/cm^3. The terrain correction was developed based on the correlation of altimetric data from local stations and the digital elevation model derived from the Shuttle Radar Topography Mission (SRTM) data. This correlation was based on the methods described by Kane (1962) and Nagy (1966) using the Gravity extension from the Oasis Montaj software.

The last stage of ground geophysical data processing was to generate magnetic and gravimetric maps using the minimum curvature interpolation (Briggs, 1974) in a regular mesh of 37.5 m (1/4 of the average spacing between acquisition lines).

For the stage of anomalies enhancement, qualitative and quantitative analyses were performed for all the previous corrected data. The qualitative analysis was based on enhancement techniques, such as the TDR (Miller and Singh, 1994) and THETA (Wijns *et al.,* 2005), to evaluate the study area's structural framework. These techniques were applied directly in the reduced-to-the-pole magnetic field airborne data while the ground magnetic and ground Bouguer data were upward continued to improve the signal/noise ratio.

The quantitative analysis involved the Euler deconvolution (for the airborne and ground data) and the radially averaged power spectrum (for the ground data) to estimate the depths of the causative sources and delineate the structural framework. Also, the power spectrum assisted in defining the values used for the upward continuation of the ground magnetic (40 m upward continued) and gravimetric (50 m upward continued) data.

The reduction-to-the-pole is a filter commonly used to minimize the dipolar effect of the geomagnetic field. This technique transforms the anomaly into the shape it would have if it were on the magnetic pole, i.e. inclination (I) = 90°; declination (D) = 0° (Baranov, 1957; Baranov and Naudy, 1964). Although the reduction-to-the-pole considers only the induced magnetization, it allows the anomalies to be positioned as close as possible to the causative sources by means of the following expression (Grant and Dodds, 1972; MacLeod *et al.,* 1993a, 1993b; Li, 2008):

$$RTP(\theta) = \frac{[sin(I) - icos(I)cos(D-\theta)]^2}{[sin^2(Ia) + cos^2(Ia)\ cos^2(D-\theta)] \cdot [sin^2(I) + cos^2(I)\ cos^2(D-\theta)]} \tag{1}$$

where I is the geomagnetic inclination, D is the geomagnetic declination, θ is the direction of the wavenumber, and Ia is the amplitude correction inclination, or pseudo-inclination, which is the complementary angle of the geomagnetic inclination.

MacLeod *et al.* (1993a, 1993b) introduced pseudo-inclination to obtain more stable responses at low magnetic inclinations (case of the study area). This parameter also suppresses amplitude and power in the direction of the inclination (Li, 2008).

The values used in the reduction to pole, according to Eq. 1, of the airborne magnetic survey were D = -13.47°, I = -36.60° and Ia = -53.40° while the parameters for the ground magnetic survey were D = -14.99°, I = -38.79° and Ia = -51.21°. Those parameters were adopted according to the acquisition of survey data average date, which were June 22, 2010, and December 17, 2017, for the airborne and ground magnetic surveys, respectively.

The TDR is defined as the arctangent of the ratio between the vertical derivative (Gz) and the total horizontal derivative (THDR):

$$TDR(\theta) = tan^{-1}\left(\frac{Gz}{THDR}\right) \quad (2)$$

This enhancement technique responds equally well to shallow and deep sources and can provide information about their horizontal extensions, due to its property of being positive above the sources, reaching zero values close to the edges and negative outside them (Miller and Singh, 1994). The TDR also provides estimates on the dip and the magnetic susceptibility contrast of the causative sources (Thurston and Smith, 1997; Salem *et al.,* 2007; Fairhead *et al.,* 2008).

The THETA is considered as the quotient between THDR and the analytic signal amplitude (ASA):

$$THETA(\theta) = cos^{-1}\left(\frac{THDR}{ASA}\right) \quad (3)$$

This filter is commonly used to outline contacts and it has the property of locating anomalies directly over their causative sources. Even though it was initially developed for regions with low magnetic latitudes, the THETA may be applied to reduced-to-pole data (Wijns *et al.,* 2005).

The upward continuation (UW) simulates the acquisition of data at heights higher the level at which the data were measured, that is, further from the sources. This filter minimizes or removes the high-frequency and noise signals and it does not produce edge effects. The UW is often used to compare magnetic and gravimetric data acquired at different altitudes (Jacobsen, 1987; Milligan and Gunn, 1997).

The Euler deconvolution is a quantitative technique applied in a set of potential anomalies that allows estimating the location and depth of causative sources based on data scanning through moving windows (Thompson, 1982; Blakely, 1995). These estimates, called solutions, are calculated based on the inversion of the Euler's homogeneity equation, which relates the magnetic and gravimetric fields and their horizontal and vertical derivatives alongside the location of the sources through the degree of homogeneity, interpreted as structural index:

$$(x - x_0)\frac{\partial M}{\partial x} + (y - y_0)\frac{\partial M}{\partial y}(z - z_0)\frac{\partial M}{\partial z} = \eta.(B - M) \quad (4)$$

where x_0, y_0, z_0 are the magnetic source positions, x, y, z are the positions of the detected total field M, B is the regional value of the total magnetic field, and η is the degree of homogeneity or structural index.

The structural index (SI) may be defined as the rate of change of the potential field's strength compared to the distance between the source and the detector for a given model geometry. The interpreter should always choose the index based on prior geological knowledge where features receive a corresponding structural index based on their generic geometric shape (Table 1). The degree of Euler's solutions concentration is acceptable when the solutions are aligned on 2D models, or superimposed on 3D models (Reid *et al.,* 1990).

Table 1. Structural index (SI) values for magnetic and gravimetric models (Reid *et al.* 1990).

Magnetic Bodies	Structural Index	Gravimetric Bodies	Structural Index
Contact/Step	0	Step/Sill/Dike	0
Sill/Dike	1	Cylinder/Pipe	1
Cylinder/Pipe	2	Sphere	2
Sphere	3		

The radially averaged power spectrum is another quantitative method to estimate the depth of potential field anomalies in the frequency domain, enabling the spectrum to delimit the deep, intermediate, shallow, and noise sources, which is used to perform the regional-residual separation. In addition, the power spectrum expresses the energy corresponding to the wavenumber and direction in the form of a two-dimensional graph, whose x-axis represents the wavenumber and y-axis the power spectrum energy logarithm, that is log E(r), which is equivalent to $4\pi r$. Depth to a set of statistical sources is given by the following equation (Spector and Grant, 1970; Cowan and Cowan, 1993):

$$h = -s/4\pi \qquad (5)$$

where h is the depth to the top of the sources and s is the slope of one portion of the power spectrum.

RESULTS AND DISCUSSIONS

The results generated from the airborne and ground geophysical data are illustrated (Figures 4, 5 and 7) in pseudo-colored contour maps alongside the geological map of Figure 2a. The total-field anomaly (TFA) map (Figure 4a), shows values varying between -5 nT and 10.5 nT in both Vacacaí Metamorphic Complex and Camaquã Basin. Only Acampamento Velho Formation's tuffs and rhyolites have a predominance of negative values, around -3 nT. The faults were characterized by anomalies of high magnetic intensity (above 1 nT) while the cupriferous occurrences were located at the edges of positive anomalies (NE-SW trend in the Victor Teixeira and NW-SE direction in Capão Grande).

A successful application of the RTP to the TFA (RTP-TFA) map can be seen in Figure 4b, where the total-field dipolar anomalies become monopolar and the RTP-TFA maximum values are higher than those of the TFA map. The basement metavolcanoclastic rocks are characterized mainly by high amplitudes (between 1 nT and 16 nT) while the volcano-sedimentary rocks of Camaquã Basin have low to intermediate values (from -9 nT to -0.90 nT), which are in good agreement with their lithotypes. There are also positive anomalies in the basin, above 0.30 nT, in the NE-SW (delimiting the tuffs) and NW-SE to E-W directions (parallel to the geological regional faults). The domain of intermediate magnetic field (around -0.90 nT) is associated with the cupriferous occurrences.

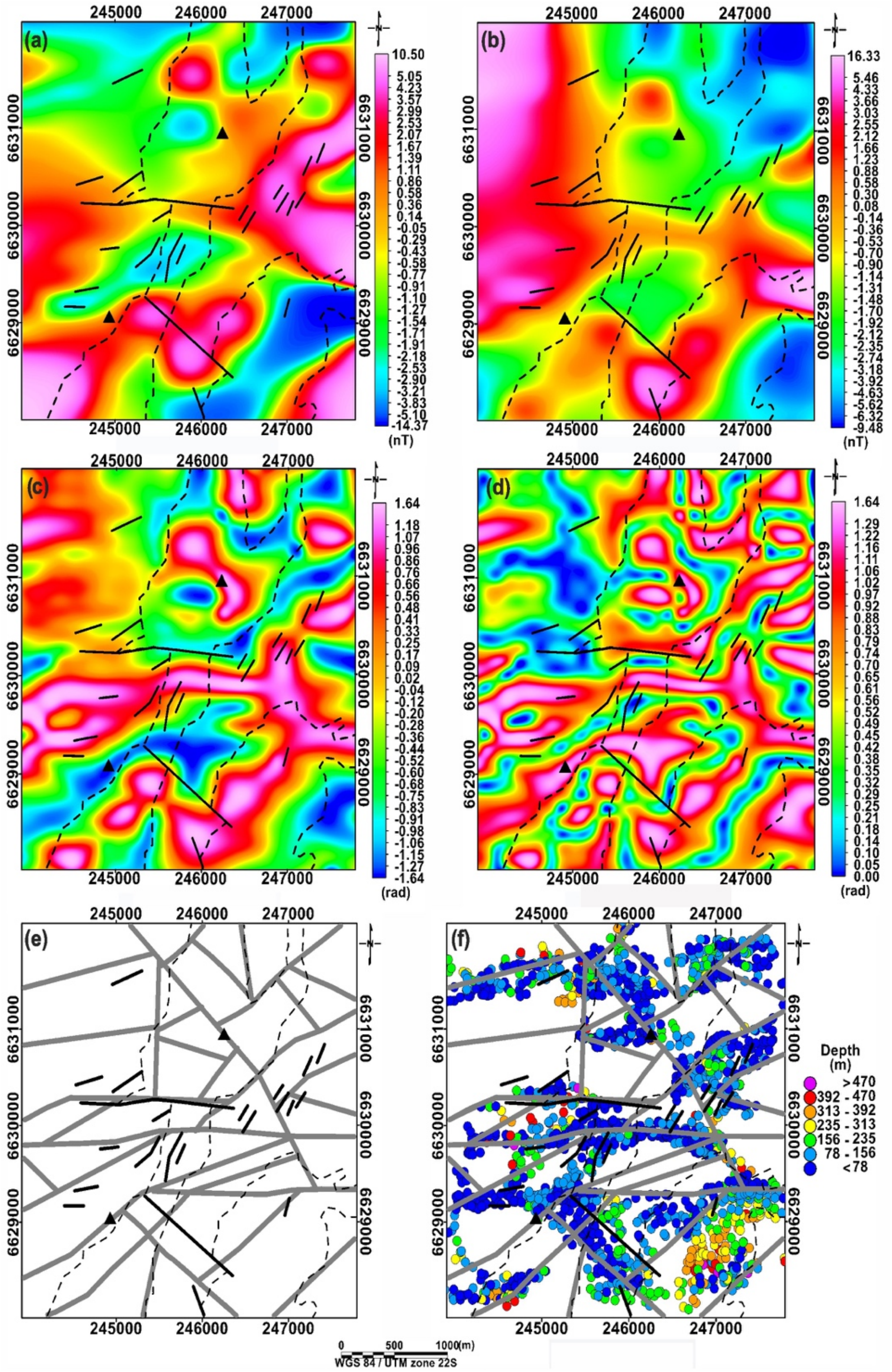

Figure 4. Airborne magnetic maps: (a) TFA; (b) RTP-TFA; (c) TDR of the data in (b); (d) THETA of the data in (b); (e) magnetic lineaments interpreted (gray lines); (f) Euler solutions. Dashed lines represent the contacts between the lithotypes while solid lines are faults (i.e, limits and structures of Figure 2a).

Figures 4c and 4d show the results of TDR and THETA enhancement techniques. These filters were used to delineate structural lineaments in the study area since they demonstrated greater coherence with the prior geological information in comparison to the results obtained from previous methods cited in the Introduction section. Moreover, both TDR and THETA equalize the amplitudes and locate the maxima over the center of the magnetic sources.

Regarding the magnetic-structural framework of the study area (Figure 4e), the metavolcanoclastic sequence of the Vacacaí Metamorphic Complex exhibits lineaments in the NE-SW and E-W directions. Moreover, the main geological structure of this complex, an E-W fault, showed a good magnetic response. Immediately to the south, another E-W magnetic structure, that crosses the region, was delineated. Magnetic lineaments with NW-SE and NE-SW direction predominate in the volcano-sedimentary sequences of the Camaquã Basin. The larger NW-SE geological fault is parallel to a magnetic lineament. The magnetic lineaments suggest that the Capão Grande copper occurrence (located at the north in the basin) is controlled by an NW-SE oriented structure while the Victor Teixeira occurrence (located at the southwestern rim of the basin) is associated with a NE-SW oriented lineament.

Figure 4f shows the Euler solutions, generated from the RTP-TFA data (Figure 4b). The parameters used for the solutions were: structural index (SI) equal to 0 (Contact/Step - Table 1), depth tolerance of 25 %; window size of 1,000 m, and flight height of 113 m (average value for the study area). The solutions were mostly located in the E-W, NE-SW, and NW-SE directions, thus in good agreement with the interpreted lineaments. The maximum and minimum depths observed were 570 m and 1 m, respectively. Most of the magnetic lineaments are situated at depths between 78 m and 156 m. Larger depths (between 235 m and 313 m) were observed mainly in the acidic tuffs of the Acampamento Velho Formation.

Figure 5a shows the RTP-TFA map of the ground magnetic data of the study area. The metavolcanoclastic rocks of the Vacacaí Metamorphic Complex are characterized mainly by high-intensity anomalies (above 36 nT), with Victor Teixeira occurrence located on the edge of one of those. From this occurrence towards the central region of the map, the contact with the Passo da Promessa Formation sandstones is practically outlined by low magnetic intensities (about -10 nT). This signature continues northward to the E-W regional geologic fault, where the magnetic field increases in the Capão Grande occurrence direction. RTP-TFA values increase as they approach the Arroio América Formation.

The RTP-TFA map upward continued to 40 m can be seen in Figure 5b, in which a smoother pattern of anomalies is observed. The height of upward continuation, 40 m, was set according to the Radially Power Averaged Spectrum (Figure 6a) analysis, which was generated from the data RTP-TFA map of ground magnetic data (Figure 5a). In addition to the values attributed to shallow and noise sources, deep sources (> 200 m depth) and intermediate sources (between 200 m and 100 m) were also interpreted.

The TDR (Figure 5c) and THETA (Figure 5d) enhancement techniques from the RTP-TFA 40 m upward continued map enabled a satisfactory qualitative interpretation of the ground magnetic-structural framework (Figure 5e), where interconnected NW-SE, NE-SW, and E-W oriented structures can be seen. In this framework, NW-SE trend lineaments are more abundant, although NE-SW trend lineaments are longer. Observed NE-SW oriented lineaments may be associated with the contact between the Vacacaí Metamorphic Complex and the Camaquã Basin, south of the E-W central geologic fault. Intersections between NE-SW and NW-SE structures are recurrent in those geological units and are also observed in the Victor Teixeira and Capão Grande copper occurrences.

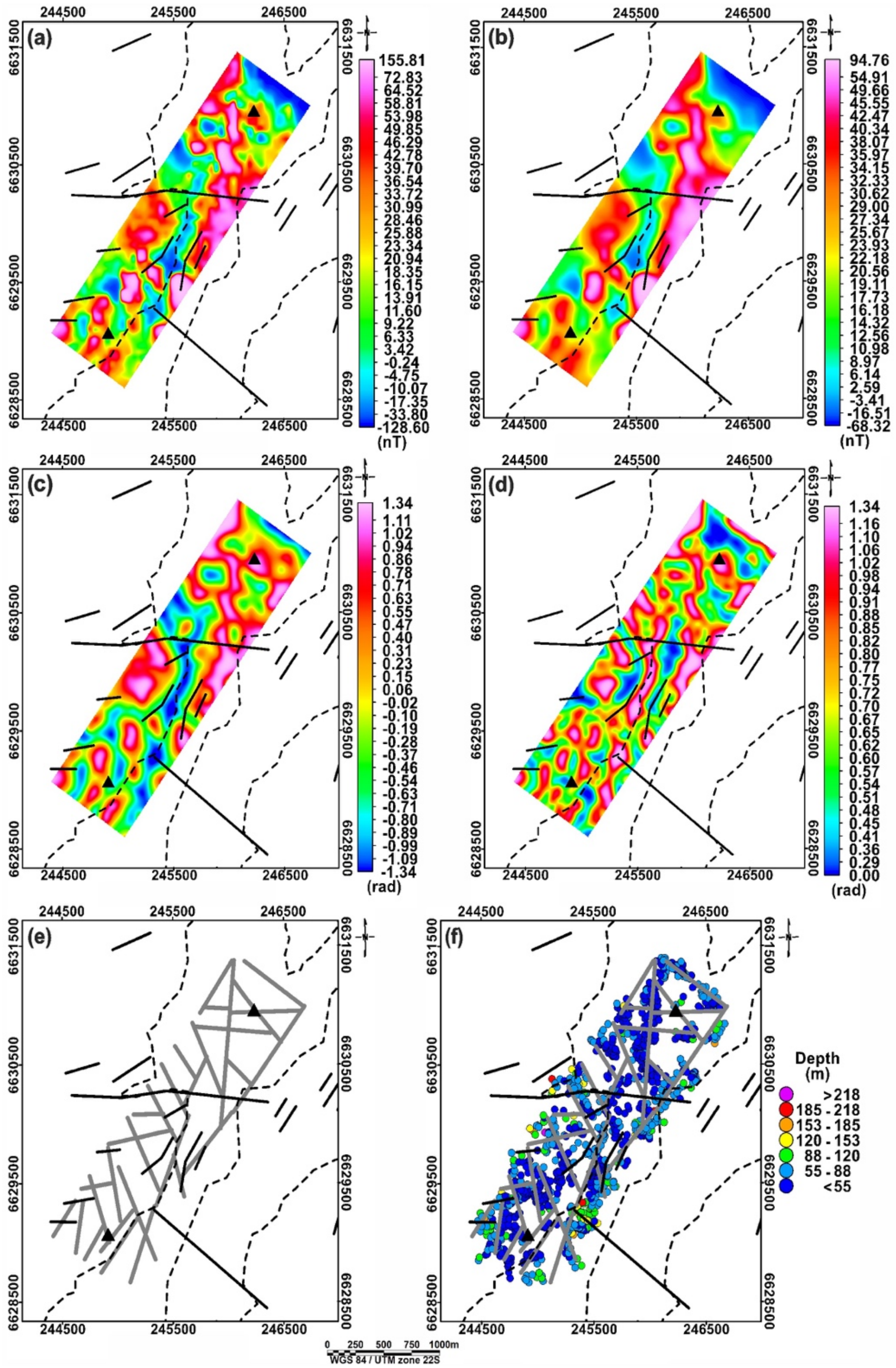

Figure 5. Ground magnetic maps: (a) RTP-TFA; (b) RTP-TFA upward continued (UW) to 40 m; (c) TDR of the data in (b); (d) THETA of the data in (b); (e) magnetic lineaments interpreted (gray lines); (f) Euler solutions. Dashed lines represent the contacts between the lithotypes while solid lines are faults (i.e, limits and structures of Figure 2a).

Euler solutions (Figure 5f) show good agreement with the interpreted lineaments. The depths were situated between 22 m and 250 m and were determined based on the following parameters: structural index (SI) equal to zero (Contact/Step); depth tolerance of 15%; window size of 300 m and distance between the sensor and the ground surface of 1.8 m. The lineaments were characterized by depths varying between 55 m and 88 m.

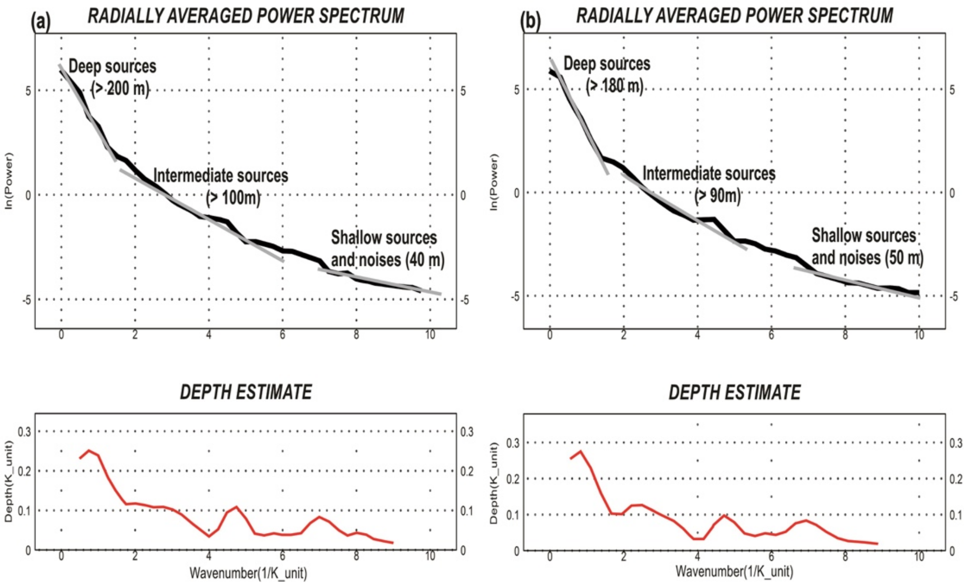

Figure 6. Radially averaged power spectrum: (a) ground magnetic data; (b) ground gravimetric data.

Ground Bouguer gravity anomalies of the study area ranged from 6.16 mGal to 14.58 mGal (Figure 7a). The southwestern area (Victor Teixeira occurrence) presents the lowest values (between 6.16 mGal and 9.21 mGal). In the central region, a strong E-W oriented anomaly (14.58 mGal) stands out. Positive anomalies of similar intensity predominate (10.09 mGal to 14.58 mGal) near the Capão Grande mineralization.

The attenuation of the signal without significant loss of geological information is evident in Figure 7b, which illustrates the ground Bouguer anomaly map upward continued to 50 m. The TDR (Figure c) and THETA (Figure 7d) enhancement techniques were applied to this map to outline the gravimetric-structural framework (Figure 7e), whose qualitative interpretation of the lineaments proved to be satisfactory with the mapped geology.

Preferential trends in the gravimetric-structural framework (Figure 7e) are observed in the NW-SE, E-W, and NE-SW directions. In the central area, E-W structures dominate (one of the lineaments is consistent with a part of the geologic regional fault) while the other lineament trends intersect near the copper occurrences.

Euler solutions (Figure 7f), based on the Bouguer anomaly data (Figure 7a), indicate depths between 19 m and 340 m, which were determined by the following parameters: SI equals to 0 (Contact/Step); depth tolerance of 15 %; window size of 300 m and height of 17 cm (distance between the gravimeter tripod and the surface). The solutions were consistent with the gravity observed structures (mainly those in the NW-SE trend). The lineaments interpreted around the copper mineralizations presented depths from 70 m to 120 m. The central E-W structures are deeper (between 120 m and 170 m). In addition, depths greater than 170 m are indicated in the innermost portions of the geological units and near to the contacts.

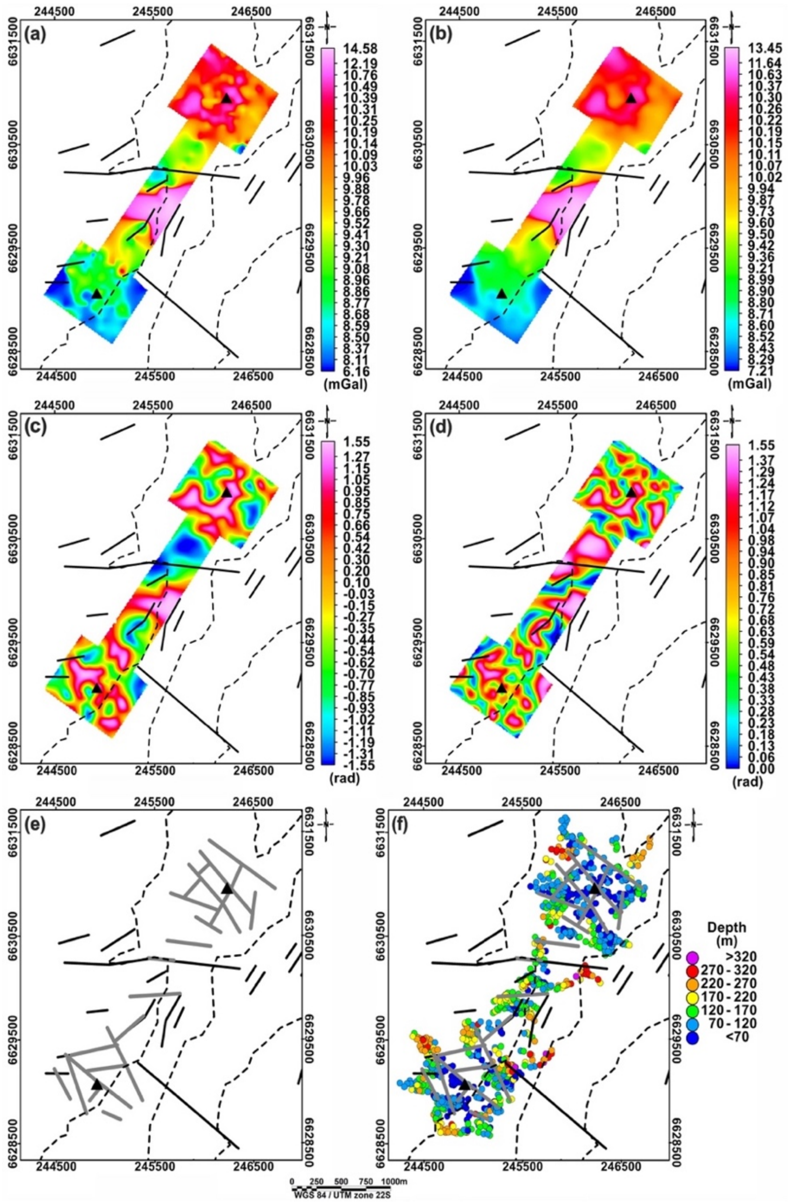

Figure 7. Ground gravimetric maps: (a) Bouguer anomaly; (b) Bouguer anomaly upward continued to 50 m; (c) TDR of the data in (b); (d) THETA of the data in (b); (e) gravimetric lineaments interpreted (gray lines); (f) Euler solutions. Dashed lines represent the contacts between the lithotypes while solid lines are faults (i.e, limits and structures of Figure 2a).

The assimilation of results obtained in the interpretative potential field maps (Figure 4e, Figure 5e, and Figure 7e) allowed us to present the interpretation of the integrated geophysical-structural framework of the study area (Figure 8a). Moreover, the surface structural lineaments can be observed in Figure 8b. They were delineated according to the analysis of shaded SRTM imagery (azimuths used: 0°, 45°, 90°, 135°, 180°, 225°, 270° and 315°) using the QGIS package.

The geophysical-structural picture of the study area (Figure 8a) reveals the interconnection of NE-SW, NW-SE and E-W lineaments, which may indicate a likely correlation between the copper mineralizations, as the lineaments may act as conduits for paleofluids, as well as for the remobilization of metals in the country rock and subsequent concentration of these elements. These processes may be related to an epithermal magmatic event associated with the post-collisional period of the Dom Feliciano orogenesis, which dates at the end of the Brasiliano Cycle (Remus *et al.,* 2000; Toniolo *et al.,* 2007; Mexias *et al.,* 2007; Fontana, 2016).

The interpretation of orbital lineaments, presented in Figure 8b, also reveals a structural framework that connects the studied cupriferous occurrences. This validates the geophysical-structural framework results and suggests that such structures are significant in both shallow and deep levels.

Figure 8a and b indicate that NE-SW and NW-SE lineaments predominate compared to the E-W trend. NE-SW trends primarily are associated with geological contacts while NW-SE lineaments often intercept them, as in the case of cupriferous occurrences. In addition, there is a good correlation between orbital and airborne (magnetic) and ground (magnetic and gravimetric) lineaments in the area of the occurrences, especially in NW-SE lineaments in Capão Grande and NE-SW in Victor Teixeira. In the central study area, there was a correspondence between orbital and geophysical lineaments in the E-W direction and the mapped geology, corroborating the main geological E-W oriented fault and still revealing another structure parallel to the south, which may crosscut all the geological units according to airborne magnetic data.

The main trends (NE-SW, NW-SE, and E-W) of the geophysical-structural framework and surface structures (Figure 8a and b) reflect the tectonic history of superposition of the four main deformation phases that affected the Vacacaí Metamorphic Complex and Maricá and Cerro do Bugio Groups in the study area. The first three phases resulted in the generation of faults and coaxial folds with NE-SW oriented axes (plunging 50° to NW) and the last deformation phase resulted in faults and folds with NW-SE and E-W oriented axes, produced by a strong reorientation in the stress system (Koppe, 1990; Machado *et al.,* 1990; CPRM, 1995; Remus *et al.,* 1999).

The remarkable interlacement of geophysical and orbital lineaments that characterizes the copper occurrences (Figure 8a e b) endorses the importance of these sites as prospective guides in mineral research campaigns in the study area. This is due to several prospects, occurrences, and polymetallic deposits from the Sul-Riograndense Shield and Camaquã Basin being located at the intersection of N20-30E (e.g. Irapuá fault system) and N50-60W oriented regional structures (e.g. Cerro da Vigia fault system) (Ribeiro *et al.,* 1966; Ribeiro, 1970; Remus *et al.,* 2000; Almeida *et al.,* 2010).

In summary, based on the prospective guide mentioned before, it is possible to suggest a target area with a high potential for mineralization in the region between the copper occurrences, near the contact between the Vacacaí Metamorphic Complex and the Passo da Promessa Formation. In addition to the intersections of NE-SW and NW-SE structures in that region, an E-W structure crosscut all geological units. Moreover, this location stands out for its high values of depth (around 170 m) from Euler solutions.

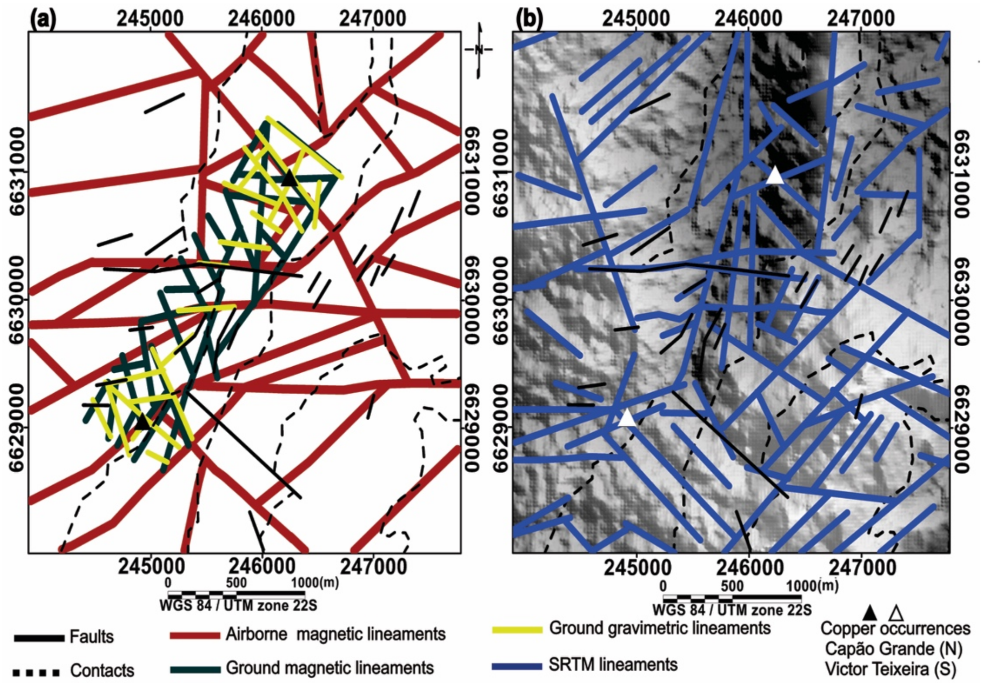

Figure 8. Geophysical-structural framework of the study area (a) and orbital lineaments (b).

CONCLUSIONS

The use of airborne and ground magnetic and gravity data confirmed its potential in the elaboration of geophysical-structural maps. These were based on the enhancements applied from qualitative techniques of the tilt angle (TDR) and the Theta Map (THETA) over the Bouguer anomalies and reduced-to-the-pole magnetic grids.

The solutions, which have structural index associated with geological contacts derived from the quantitative Euler deconvolution, proved to be consistent with the lineaments interpreted by qualitative techniques. Such solutions pointed out that most of the delineated structures extend to at least 170 m in the subsurface.

The geophysical-structural framework obtained for the study area revealed a pattern of interconnected joints, faults, and fractures that may result in vertical conduits that are suitable for the circulation of mineral-rich fluids. These fluids are relevant in the formation and control of deposits in magma-hydrothermal systems, as recognized in several occurrences of base metals in the Sul-Riograndense Shield and in the Camaquã Basin, which supports the correlation between the Victor Teixeira and Capão Grande mineralizations, which are separated by a distance of 2,300 m.

The joint use of magnetic and gravity methods enabled the recognition of structural lineaments at different depths and association with different deformation phases. Our analyses of post-processing products suggest the prospective targets of mineral occurrences where there are intersections of geophysical-structural lineaments. These lineaments may present high values of depth. However, they lack detectable indicators in the surface geology.

The intersection pattern of NE-SW and NW-SE oriented geophysical-structural lineaments, which presents in the copper outcrops and related to different depths and deformational phases, constitutes a prospective guide for similar places where there is a lack of surface evidence. This prospective guide may contribute to identifying potential new targets in mineral research campaigns, as pointed out in the central region of the study area.

ACKNOWLEDGEMENTS: The authors would like to thank the Geological Survey of Brazil (CPRM) for providing the aerogeophysical data and the Applied Geophysics Lab of Federal University of Pampa for allowing us to borrow the magnetometers and gravity meter used in the ground survey. H.G. Pereira thanks the Coordination for the Improvement of Higher Education Personnel (CAPES, Brazil), finance code 001, for granting the scholarship. F.J.F. Ferreira and C.A. Moreira were supported in this research by National Council for Scientific and Technological Development (CNPq, Brazil - contract 303826/2018-5) and São Paulo Research Foundation (FAPESP, Brazil – process nº 2019/14565-3), respectively.

REFERENCES:

Alatorre-Zamora, M. A., Campos-Enríquez, J. O., Fregoso, E., Belmonte-Jiménez, S. I., Chávez-Segura, R., Gaona-Mota, M., 2020, Basement faults deductions at a dumpsite using advanced analysis of gravity and magnetic anomalies. *Near Surface Geophysics.*, 18, 307-331, DOI: https://doi.org/10.1002/nsg.12093.

Almeida, R. P., Janikian, L., Fragoso-Cesar, A. R., Fambrini, G. L., 2010, The Ediacaran to Cambrian Rift System of Southeastern South America: Tectonic Implications. *The Journal of Geology.*, 118, 145-161, DOI: https://doi.org/10.1086/649817.

Almeida, R. P., Janikian, L., Fragoso-Cesar, A. R. S., Marconato, A., 2009, Evolution of a rift basin dominated by subaerial deposits: The Guaritas Rift, Early Cambrian, Southern Brazil. *Sedimentary Geology.,* 217, 30–51, DOI: https://doi.org/10.1016/j.sedgeo.2009.01.010.

Almeida, D. P. M., Conceição R. V., Chemale Jr, F., Koester, E., Borba, A., Petry, K., 2005, Evolution of heterogeneous Mantle in the Acampamento Velho and RodeioVelho volcanic events, Camaquã Basin, Southern Brazil. *Gondwana Research.,* 8, 479–492, DOI: https://doi.org/10.1016/S1342-937X(05)71150-3.

Almeida, F. F. M., Hasui, Y., Brito Neves, B. B., Fuck, R. A., 1981, Brazilian strucural provinces: An introduction. *Earth-Science Reviews.,* 17, 1-29, DOI: https://doi.org/10.1016/0012-8252(81)90003-9.

Araffa, S. A., El-bohoty, M., Abou Heleika M., Mekkawi, M., Ismail, E., Khalil, A., EL-Razek, E.M.A., 2018, Implementation of magnetic and gravity methods to delineate the subsurface structural features of the basement complex in central Sinai area, Egypt. *NRIAG Journal of Astronomy and Geophysics.,* 7, 162-174, DOI: https://doi.org/10.1016/j.nrjag.2017.12.002.

Babinski, M., Chemale Jr, F., Hartmann, L. A., Van Schmus, W. R., Silva, L. C., 1996, Juvenile accretion at 750-700 Ma in Southern Brazil. *Geology.,* 24, 439-442, DOI: https://doi.org/10.1130/0091-7613(1996)024<0439:JAAMIS>2.3.CO;2.

Baranov, V. and Naudy, H., 1964, Numerical calculation of the formula of reduction to the magnetic pole. *Geophysics.,* 29, 67-79, DOI: http://dx.doi.org/10.1190/1.1439334.

Baranov, V., 1957, A new method for interpretation of aeromagnetic maps: Pseudo-gravimetric anomalies. *Geophysics.,* 22, 359-383, DOI: https://doi.org/10.1190/1.1438369.

Barbuena, D., de Souza Filho, C. R., Leite, E. P., Miguel Junior, M., de Assis, R. R., Xavier, R. P., Ferreira, F. J. F., de Barros, A. J. P., 2013, Airborne geophysical data analysis applied to geological interpretation in the Alta Floresta gold province, MT. *Brazilian Journal of Geophysics.*, 31, 169-186, DOI: http://dx.doi.org/10.22564/rbgf.v31i1.254.

Bitencourt, J. C., Lima, J. P. R., Hansen, M. A. F., Pereira, H. G., Moreira, C. A., 2020, Aplicação de método eletromagnético terrestre de investigação rasa numa ocorrência cuprífera localizada no interior do município de Caçapava do Sul (RS). *Geociências.,* 39, 379-391, DOI: https://doi.org/10.5016/geociencias.v39i2.13158.

Blakely, R. J., 1995, Potential Theory in Gravity and Magnetic Applications. Cambridge University Press, Cambridge, 464 pp, DOI: https://doi.org/10.1017/CBO9780511549816.

Borba, A. W., Mizusaki, A. M. P., Santos, J. O. S., McNaughton, N. J., Onoe, A. T., Hartmann, L. A., 2008, U-Pb zircon and 40Ar-39Ar Kfeldspar dating of the syn-sedimentary volcanism of the Neoproterozoic Maricá Formation: constraining the age of foreland basin inception and inversion in the Camaquã Basin of southern Brazil. *Basin Research.,* 20, 359-375, DOI: https://doi.org/10.1111/j.1365-2117.2007.00349.x.

Borba, A. W., Maraschin, A. J., Mizusaki, A. M., 2007, Evolução Tectono-Estratigráfica e Paleoclimática da Formação Maricá (Escudo Sul-Rio-Grandense, Brasil): um Exercício de Geologia Histórica e Análise Integrada de uma Bacia Sedimentar Neoproterozoica. *Revista Pesquisa em Geociências.,* 34, 57-74, https://doi.org/10.22456/1807-9806.19472.

Borba, A. W., Mizusaki, A. M. P., Silva, D. R. A., Koester, E., Noronha, F. L., Casagrande, J., 2006, Provenance of the Neoproterozoic Maricá Formation (Sul-rio-grandense Shield, southern Brazil): petrographic and Sm-Nd isotopic constraints. *Gondwana Research.,* 9, 464-474, DOI: https://doi.org/10.1016/j.gr.2006.01.005.

Briggs, I.C., 1974, Machine contouring using minimum curvature. *Geophysics.,* 39, 39-48, DOI: https://doi.org/10.1190/1.1440410.

Brito Neves, B. B. and Cordani, U. G., 1991, Tectonic evolution of South America during the Late Proterozoic. *Precambrian Research.,* 53, 23-40, DOI: https://doi.org/10.1016/0301-9268(91)90004-T.

Campos, D. S., Silva, A. M., Toledo, C. L. B., de Carvalho, M. J., Rodrigues, V. G., Araujo, K., 2017, Prospectivity analysis of gold and iron oxide copper-gold-(silver) mineralizations from the Faina Greenstone Belt, Brazil, using multiple data sets. *Brazilian Journal of Geology.,* 47, 561-590, DOI: http://dx.doi.org/10.1590/2317-4889201720170012.

Carvalho, L. M. M., Pires, A. C. B., Oliveira, C. G., Moraes, R. A. V., Blum, M. L. B., 2006, Processamento e interpretação de dados magnetométricos aéreos do projeto Itabira-ferros, MG: uma ferramenta no auxílio ao mapeamento geológico-estrutural. *Revista Brasileira de Geociências.,* 36, 85-92, DOI: https://doi.org/10.25249/0375-7536.200636S17784.

Castro, L. G. and Ferreira, F. J. F., 2015, Arcabouço geofísico-estrutural da porção meridional do Cinturão Ribeira. *Brazilian Journal of Geology.,* 45, 499-516, DOI: https://doi.org/10.1590/2317-4889201520150007.

Cooper, G. R. J. and Cowan, D. R., 2006, Enhancing potential field data using filters based on the local phase. *Computers & Geosciences.,* 32, 1585–1591, DOI: https://doi.org/10.1016/j.cageo.2006.02.016.

Cordell, L. and Graunch, V. J. S., 1985, Mapping basement magnetization zones from aeromagnetic data in the San Juan Basin, New Mexico. In: Hinze, W. J., The Utility of Regional Gravity and Magnetic Anomalies Maps. Society of Exploration Geophysicists, 181–197, DOI: http://dx.doi.org/10.1190/1.0931830346.ch16.

Côrtes, A. R. P., Moreira, C. A., Paes, R. A. S., Veloso, D. I. K., 2019, Geophysical and Metalogenetic Modelling of the Copper Occurrence in Camaquã Sedimentary Basin, Brazilian Southern. *Pure and Applied Geophysics.,* 176, 4955-4968, DOI: https://doi.org/10.1007/s00024-019-02190-8.

Côrtes, A. R. P., Moreira, C. A., Veloso, D. I. K., Vieira, L. B., Bergonzoni, F. A., 2016, Geoelectrical prospecting for a copper sulfide mineralization in the Camaquã sedimentary basin, Southern Brazil. *Geofísica Internacional.,* 55, 165–174, DOI: http://revistagi.geofisica.unam.mx/index.php/RGI/article/view/1719.

Cowan, D. R. and Cowan, S., 1993, Separation Filtering Applied to Aeromagnetic Data. *Exploration Geophysics.,* 24, 429–436, DOI: https://doi.org/10.1071/eg993429.

CPRM - Brazilian Geological Survey., 2010, Projeto Aerogeofísico Escudo do Rio Grande do Sul: relatório final do levantamento e processamento dos dados magnetométricos e gamaespectrométricos. Volume I, Lasa Prospecções, Programa Geologia do Brasil, Rio de Janeiro.

CPRM - Brazilian Geological Survey., 2007, Mapa geológico do Estado do Rio Grande do Sul. Programa Geologia do Brasil, Projeto Geologia do Brasil ao Milionésimo, Porto Alegre.

CPRM – Brazilian Geological Survey., 2000, Cachoeira do Sul: folha SH.22-Y-A: estado do Rio Grande do Sul. Programa Levantamentos Geológicos Básicos do Brasil, Brasília.

CPRM - Brazilian Geological Survey., 1995, Passo do Salsinho, Folha SH.22-Y-A-I-4: Estado do Rio Grande do Sul. Programa Levantamentos Geológicos Básicos do Brasil, Projeto Mapeamento Geológico e Metalogenético, Brasília.

De Ros, L. F., Morad, S., Paim, P. S. G., 1994, The role of detrital composition and climate on the diagenetic evolution of continental molasses: evidence from the Cambro-Ordovician Guaritas Sequence, southern Brazil. *Sedimentary Geology.,* 92, 197–228, DOI: https://doi.org/10.1016/0037-0738(94)90106-6.

de Souza, J., Ferreira, F.J.F., 2015, The application of the Signum transform to the interpretation of magnetic anomalies due to prismatic bodies. In: 24th International Geophysical Conference and Exhibition, Perth, Western Australia, DOI: https://doi.org/10.1071/ASEG2015ab190.

de Souza, J., Ferreira, F.J.F., 2013, On the use of derivatives for interpreting magnetic anomalies due to dyke-like bodies II: application to synthetic and field data. In: SEG Houston Annual Meeting, DOI: https://doi.org/10.1190/segam2013-0455.1.

de Souza, J., Ferreira, F.J.F., 2012, On the use of derivatives for interpreting magnetic anomalies due to dyke-like bodies: qualitative and quantitative analysis. In: International Geophysical Conference and Oil & Gas, Istanbul, 1, 1 – 4, DOI: https://doi.org/10.1190/IST092012-001.157.

Dentith, M. and Mudge, S. T., 2014, Geophysics for the Mineral Exploration Geoscientist. Cambridge University Press, Cambridge, 454 pp, DOI: https://doi.org/10.1017/CBO9781139024358.

Evjen, H. M., 1936, The place of vertical gradient in gravitational interpretations. *Geophysics.,* 1, 127-136, DOI: http://dx.doi.org/10.1190/1.1437067.

Fairhead, J. D., Salem, A., Williams, S., Samson, E., 2008, Magnetic interpretation made easy: The tilt-depth-dip-Δ*k* method. In: SEG Technical Program Expanded Abstracts. Society of Exploration Geophysicists, 779–783, DOI: https://doi.org/10.1190/1.3063761.

Fernandes, L. A. D., Menegat, R., Costa, A. F. U., Koester, E., Porcher, C. C., Tommasi, A., Kraemer, G., Ramgrab, G. E., Camozzato, E. E., 1995, Evolução tectônica do Cinturão Dom Feliciano no Escudo Sul-Rio-Grandense: Parte II - Uma contribuição a partir das assinaturas geofísicas. *Revista Brasileira de Geociências.,* 25, 375-384, DOI: https://doi.org/ 10.25249/0375-7536.1995375384.

Ferreira, F. J. F., de Souza, J., Bongiolo, A. B. S., Castro, L. G., 2013, Enhancement of the total horizontal gradient of magnetic anomalies using tilt angle. *Geophysics.,* 78, 33–41, https://doi.org/10.1190/geo2011-0441.1.

Fontana, E., 2016, Hidrotermalismo e mineralizações das rochas vulcânicas da mina do Seival: evolução geoquímica e isotópica (δ34S, δ18O e δ13C) dos fluidos e sua correlação com outros depósitos de minérios epitermais da Bacia do Camaquã – Rio Grande do Sul – Brasil. Doctoral Thesis, University of Rio Grande do Sul (UFRGS), Porto Alegre, 201 pp.

Fragoso-Cesar, A. R. S., Fambrini, G. L., Almeida, R. P., Pelosi, A. P. M. R., Janikian, L., Riccomini, C., Nogueira, A., Saes, G., 2000, The Camaquã Extensional Basin: Neoproterozoic To Early Cambrian Sequences In Southernmost Brazil. *Revista Brasileira de Geociências.*, 30, 442-445, DOI: https://doi.org/10.25249/0375-7536.2000303442445.

Gastal, M. C., Ferreira, F. J. F., da Cunha, J.U., Esmeris, C., Koester, E., 2015, Alojamento do granito Lavras e a mineralização aurífera durante evolução de centro vulcano-plutônico pós-colisional, oeste do Escudo Sul-riograndense: dados geofísicos e estruturais. *Brazilian Journal of Geology.*, 45, 217-241, DOI: http://dx.doi.org/10.1590/23174889201500020004.

Grant, F.S. and Dodds, J., 1972, MAGMAP FFT Processing System Development Notes. Paterson Grant and Watson Limited.

Hallinan, S. E., Mantovani, M. S. M., Shukowsky, W., Braggion Jr, I., 1993, Estrutura do Escudo Sul- Brasileiro: uma revisão através de dados gravimétricos e magnetométricos. *Revista Brasileira de Geociências.,* 23, 201-214, DOI: https://doi.org/10.25249/0375-7536.1993233201214.

Hartmann, L. A., Leite, J. A. D., Silva, L. C., Remus, M. V. D., McNaughton, N. J., Groves, D. I., Fletcher, I. R., Santos, J. O. S., Vasconcellos, M. A. Z., 2000, Advances in SHRIMP geochronology and their impact on understanding the tectonic and metallogenic evolution of southern Brazil. *Australian Journal of Earth Sciences.,* 47, 829-844, DOI: https://doi.org/10.1046/j.1440-0952.2000.00815.x.

Heiskanen, W and Moritz, H., 1967, Physical Geodesy. W.H. Freeman and Campany, San Francisco and London, 302 pp.

Hinze, W., Von Frese, R., Saad, A., 2013, Gravity and Magnetic Exploration: Principles, Practices, and Applications.

Cambridge, Cambridge University Press, 525 pp. DOI: https://doi.org/10.1017/CBO9780511843129.

Isles D. J., and Rankin L. R., 2013, Geological Interpretation of Aeromagnetic Data. Collingwood, CSIRO Publishing, 365 pp. DOI: https://doi.org/10.1190/1.9781560803218.

Jacobsen, B.H., 1987, A case for upward continuation as a standard separation filter for potential-field maps. *Geophysics.,* 52, 1138–1148, DOI: https://doi.org/10.1190/1.1442378.

Janikian, L., Almeida, R. P., Fragoso-Cesar, A. R. S., Corrêa, C. R. A., Pelosi, A. P. M. R., 2005, Evolução Paleoambiental e sequências deposicionais do Grupo Bom Jardim e da Formação Acampamento Velho (Supergrupo Camaquã) na porção norte da Sub-bacia Camaquã ocidental. *Revista Brasileira de Geociências.,* 35, 245-256, DOI: https://doi.org/10.25249/0375-7536.200535224525.

Janikian, L., Almeida, R. P., Fragoso-Cesar, A. R. S., and Fambrini, G. L., 2003. Redefiniçao do Grupo Bom Jardim (Neoproterozóico III) em sua área-tipo: litoestratigrafia, paleogeografia e significado tectônico das sucessões vulcano-sedimentares do Supergrupo Camaquã, RS. *Revista Brasileira de Geociências.,* 33, 349–362.

Kane, M. F., 1962, A Comprehensive System of Terrain Using a Digital Computer. *Geophysics.,* 27, 455-462, DOI: https://doi.org/10.1190/1.1439044.

Kearey, P., Brooks, M., Hill, I., 2002, An Introduction to Geophysical Exploration (3rd ed.). , Oxford, Blackwell Science, 272 pp.

Knödel, K., Lange, G., Voigt, H. J., 2007, Environmental Geology: Handbook of Field Methods and Case Studies. Berlin, Heidelberg: Springer-Verlag Berlin Heidelberg, 1357 pp, DOI: https://doi.org/10.1007/978-3-540-74671-3.

Koppe, J. C., 1990, Metalogênese do ouro da Mina da Bossoroca, São Sepé, RS. Doctoral Thesis, Federal University of Rio Grande do Sul (UFRGS), Porto Alegre, 289 pp.

Kosaroglu, S., Buyuksarac, A., Aydemir, A., 2016, Modeling of shallow structures in the Cappadocia region using gravity and aeromagnetic anomalies. *Journal of Asian Earth Sciences.,* 124, 214-226, DOI: https://doi.org/10.1016/j.jseaes.2016.05.005.

Li, X., 2008, Magnetic reduction-to-the-pole at low latitudes: observations and considerations. *The Leading Edge.,* 27, 990–1002, DOI: http://dx.doi.org/10.1190/1.2967550.

Lowrie, W., 2007, Fundamentals of Geophysics (2nd ed.). New York, Cambridge University Press, 393 pp. DOI: https://doi.org/10.1017/CBO9780511807107.

Luiz, J. G., Costa e Silva, L. M., 1995, Geofísica de Prospecção**.** Belém, Cejup, 335 pp 1995.

Machado, N., Koppe, J. C., Hartmann, L. A., 1990, A late Proterozoic U-Pb age for the Bossoroca Belt, Rio Grande do Sul, Brazil. *Journal of South American Earth Sciences.,* 3, 87-90, DOI: https://doi.org/10.1016/0895-9811(90)90021-R.

MacLeod, I. N., Vieira, S., Chaves, A. C., 1993a, Analytic signal and reduction-to-the-pole in the interpretation of total magnetic field data at low magnetic latitudes. In: 3rd International Congress of the Brazilian Geophysical Society, DOI: https://doi.org/10.3997/2214-4609-pdb.324.830.

MacLeod, I. N., Jones, K., Dai, T. F., 1993b, 3-D Analytic Signal in the Interpretation of Total Magnetic Field Data at Low Magnetic Latitudes. *Exploration Geophysics.,* 24, 679–688, DOI: https://doi.org/10.1071/EG993679.

Matté, V., Sommer, C.A., Lima, E. F., Saldanha, D. L., Pinheiro-Sommer, J. A., Liz, J. D., 2012, Rochas dioríticas do Platô da Ramada, Rio Grande do Sul, e sua relação com o vulcanismo alcalino da Formação Acampamento Velho, Neoproterozoico do Escudo Sul-RioGrandense. *Revista Brasileira de Geociências.,* 42, 343-362, DOI: http://dx.doi.org/10.5327/Z0375-75362012000200010.

Mexias, A. S., Bongiolo, E. M., Gomes, M. E. B., Formoso, M. L L., Frantz, J. C., 2007, Alterações hidrotermais e mineralizações nas rochas da associação plutono-vulcano-sedimentar da região de Lavras do Sul-RS. In: Iannuzzi, R. and Frantz, J. C. 50 anos de Geologia: Instituto de Geociências. Contribuições, Comunicação e Identidade, Porto Alegre, p 145-159.

Miller, H.G. and Singh, V., 1994, Potential field tilt – a new concept for location of potential field sources. *Journal of Applied Geophysics.,* 32, 213–217, DOI: https://doi.org/10.1016/0926-9851(94)90022-1.

Milligan, P. R. and Gunn, P. J., 1997, Enhancement and presentation of airborne geophysical data. *AGSO Journal of Australian Geology & Geophysics.,* 17, 63-75.

Milsom, J., 2003, Field geophysics (3^{rd} ed.). Chichester, John Wiley & Sons Ltd, 249 pp

Moreira, C. A. and Ilha, L. M., 2011, Prospecção geofísica em ocorrência de cobre localizada na bacia sedimentar do Camaquã (RS). *Revista Escola de Minas.,* 64, 305–311, DOI: http://dx.doi.org/10.1590/S0370-44672011000300008.

Nabighian, M. N., 1972, The analytic signal of two-dimensional magnetic bodies with polygonal cross-section: its properties and use for automated anomaly interpretation. *Geophysics.,* 37, 507–517, DOI: https://doi.org/10.1190/1.1440276.

Nagy, D., 1966, The Gravitational Attraction of a Right Rectangular Prism. *Geophysics.,* 31, 362-371, DOI: https://doi-org.ez1.periodicos.capes.gov.br/10.1190/1.1439779.

Nogueira, F. C. C., Oliveira, M. S., Castro, D. L., 2004, Estudo Magnético e Gravimétrico do Arcabouço Estrutural da Bacia Rio do Peixe – PB. *Revista de Geologia.,* 17, 74-87.

Oliveira, S. P., Ferreira, F. J. F., de Souza, J., 2017, EdgeDetectPFI: An algorithm for automatic edge detection in potential field anomaly images–application to dike-like magnetic structures. *Computers & Geosciences.,* 103, 80–91, DOI: https://doi.org/10.1016/j.cageo.2017.02.006.

Oliveira, S. P., Ferreira, F. J. F., de Souza, J., 2015, An algorithm for automatic edge detection from magnetic anomalies. In: 14th International Congress of the Brazilian Geophysical Society.

Osinowo, O.O. and Abdulmumin, Y., 2019, Basement configuration and lineaments mapping from aeromagnetic data of Gongola arm of Upper Benue Trough, northeastern Nigeria. *Journal of African Earth Sciences.,* 160(103597), DOI: https://doi.org/10.1016/j.jafrearsci.2019.103597.

Paim, P. S. G., Chemale, F., Lopes, R. C., 2000, A Bacia do Camaquã. In: Holz, M. and De Ros, L. F., Geologia do Rio Grande do Sul. CIGO/UFRGS, Porto Alegre, p 231–274.

Pelosi, A. P. M. R. and Fragoso-Cesar, A. R. S., 2003, Proposta litoestratigráfica e considerações paleoambientais sobre o Grupo Maricá (Neoproterozoico III), Bacia do Camaquã, Rio Grande do Sul. *Revista Brasileira de Geociências.,* 33, 137-148, DOI: https://doi.org/10.25249/0375-7536.2003332137148.

Pereira, H. G., Moreira, C. A., Camarero, P. L., 2017, Correlação de dados geofísicos em pesquisa mineral de ocorrência de cobre em Caçapava do Sul (RS). *Geociências.,* 36, 717-729.

Pereira, H. G., Filho Malagutti, W., Fries, M., Moreira, C. A., 2016, Prospecção geofísica entre as ocorrências cupríferas Capão Grande e Victor Teixeira, Caçapava do Sul - RS. *Geociências.,* 35, 16-30.

Ramos, L. N. R. A., Pires, A. C. B., Labour, C., Toledo, B., 2014, Airborne gamma-ray spectrometric and magnetic signatures of Fazenda Nova region, east portion of Arenópolis magmatic arc, Goiás. *Brazilian Journal of Geophysics.,* 32, 123-140, DOI: http://dx.doi.org/10.22564/rbgf.v32i1.401.

Reeves, C., 2005, Aeromagnetic Surveys: Principles, Practice & Interpretation. Washington, Earth-Works, 155 pp.

Reid A. B., Allsop J. M., Granser H., Millett A. J., Somerton I. W., 1990, Magnetic interpretation in three dimensions using Euler deconvolution. *Geophysics.,* 55, 80-91, DOI: https://doi.org/10.1190/1.1442774.

Remus, M. V. D., Hartmann, L. A., McNaughton, N. J., Groves, D. I., Reischl, J., 2000, Distal Magmatic-Hydrothermal Origin for the Camaquã Cu (Au-Ag) and Santa Maria Pb, Zn (Cu-Ag) Deposits, Southern Brazil. *Gondwana Research.,* 3, 155–174, DOI: https://doi.org/10.1016/S1342-937X(05)70094-0.

Remus, M. V. D., Mcnaughton, N. J., Hartmann, L. A., Koppe, J. C., Fletcher, I. R., Groves, D. I., 1999, Gold in the Neoproterozoic juvenile Bossoroca Volcanic Arc of southernmost Brazil: isotopic constraints on timing and sources. *Journal of South American Earth Sciences.,* 12, 349–366, DOI: https://doi.org/10.1016/S0895-9811(99)00026-7.

Ribeiro, M., 1970, Geologia da Folha de Bom Jardim, Rio Grande do Sul, Brasil. *Bulletin of the National Department of Mineral Production (DNPM).,* 247, 1-142.

Ribeiro, M., Bocchi, P. R., Figueiredo, P. M., Tessari, R. I., 1966, Geologia da Quadrícula de Caçapava do Sul, Rio Grande do Sul, Brasil. *Bulletin of the National Department of Mineral Production (DNPM).,* 127, 1-232.

Roest, W.R., Verhoef, J., Pilkington, M., 1992, Magnetic interpretation using the 3-D analytic signal. *Geophysics.,* 57, 116–125, DOI: https://doi.org/10.1190/1.1443174.

Ronchi, L. H. and Lobato, A. O. C., 2000, Minas do Camaquã. Um estudo multidisciplinar. São Leopoldo, Unisinos, 366 pp.

Salem, A., Williams, S., Fairhead, J. D., Ravat, D., Smith, R., 2007, Tilt-depth method: A simple depth estimation method using first-order magnetic derivatives. *The Leading Edge.,* 26, 1502-1505, DOI: https://doi.org/10.1190/1.2821934.

Soliani Jr, E., 1986, Os dados geocronológicos do Escudo Sul-Rio-Grandense e suas implicações de ordem geotectônica. Doctoral Thesis, University of São Paulo (USP), São Paulo, 417 pp, DOI: https://doi.org/10.11606/T.44.1986.tde-15072015-153916.

Sommer, C. A., Lima, E. F., Pierosan, R., Machado, A., 2011, Reoignimbritos e ignimbritos de alto grau do vulcanismo Acampamento Velho, RS: origem e temperatura de formação. *Revista Brasileira de Geociências.,* 41, 420-435, DOI: https://doi.org/10.25249/0375-7536.2011413420435.

Sommer, C.A., Lima, E.F., Nardi, L.V.S., 1999, Evolução do vulcanismo alcalino na porção sul do Platô do Taquarembó, Dom Pedrito - RS. *Revista Brasileira de Geociências.,* 29, 245-254, DOI: https://doi.org/10.25249/0375-7536.199929245254.

Spector, A. and Grant, F. S., 1970, Statistical models for interpreting aeromagnetic data. *Geophysics.,* 35, 293-302, DOI: https://doi.org/10.1190/1.1440092.

Teixeira, A. L., Gaucher, C., Paim, P. S. G., Fonseca, M. M., Parente, C. V., Silva Filho, W. F., Almeida, A. R., 2004, Bacias do estágio da transição da plataforma sul-americana. In: Neto, V. M., Bartorelli, A., Carneiro, C. D. R., Brito-Neves, B. B., Geologia do Continente Sul-Americano: Evolução da Obra de Fernando Flávio Marques de Almeida. Beca, São Paulo, p. 448–487.

Telford, W., Geldart, L., Sheriff, R., 1990, Applied Geophysics (2nd ed.). Cambridge, Cambridge University Press, 770 pp. DOI: https://doi.org/10.1017/CBO9781139167932.

Thompson, D.T., 1982, EULDPH: A new technique for making computer-assisted depth estimates from magnetic data. *Geophysics.,* 47, 31–37, DOI: https://doi.org/10.1190/1.1441278.

Thurston J. B. and Smith R. S., 1997, Automatic conversion of magnetic data to depth, dip, and susceptibility contrast using SPI (TM) method. *Geophysics.,* 62, 807-813, DOI: https://doi.org/10.1190/1.1444190.

Toniolo, J. A., Gil, C. A. A., Sander, A., 2007, Metalogenia das bacias neoproterozóico-eopaleozóicas do Sul do Brasil: Bacia do Camaquã. Programa de Geologia do Brasil - Projeto Baneo, Porto Alegre.

Verduzco, B., Fairhead, C., Green, C., Mackenzie, C., 2004, New insights into magnetic derivatives for structural mapping. *The Leading Edge.,* 23, 116–119, DOI: https://doi.org/10.1190/1.1651454.

Weihermann, J. D., Ferreira, F. J. F, Oliveira, S. P., Cury, L. F., de Souza, J., 2018, Magnetic interpretation of the Paranaguá Terrane, southern Brazil by signum transform. *Journal of Applied Geophysics.,* 154, 116–127, DOI: https://doi.org/10.1016/j.jappgeo.2018.05.001.

Wijns C., Perez C., Kowalczyk P., 2005, Theta map: Edge detection in magnetic data. *Geophysics.,* 70, 39-43, DOI: https://doi.org/10.1190/1.1988184.

Original paper

MULTISOURCE DATA INTEGRATION FOR GROUNDWATER PROSPECTING IN PRECAMBRIAN SHEAR ZONES, ESPÍRITO SANTO STATE (SOUTHEASTERN BRAZIL)

Marcos Eduardo Hartwig[1*], César Augusto Moreira[2] and Marilane Gonzaga de Melo[2]

Received: April 26, 2020; accepted: November 18, 2020; published online: April 1, 2021.

RESUMEN

Las rocas metamórficas Precámbricas en la región sur del estado de Espírito Santo (sureste de Brasil) están interceptadas por zonas de cizallamiento dúctiles y quebradizas / dúctiles sobre las cuales se establecieron pueblos como Guaçuí, Marechal Floriano y Domingos Martins. En los años de 2014 a 2016, el estado de Espírito Santo enfrentó la peor sequía de los últimos 80 años. En situaciones como esa, la única fuente de agua dulce disponible es subterránea. Por lo tanto, el propósito de este estudio fue integrar datos de fuentes múltiples para la prospección y gestión de aguas subterráneas. El área de estudio comprende los sectores centrales de las zonas de cizallamiento Guaçuí y Batatal. La metodología abarca la interpretación de pares estereoscópicos para la identificación de lineamientos estructurales, prospección geofísica (resistividad eléctrica) y trabajos geológicos de campo. Los resultados se validaron tentativamente con los datos de producción de pozos de agua subterránea disponibles. Se estudiaron seis perfiles de resistividad con una longitud total de 2.400 m y se describieron 15 afloramientos. Los resultados mostraron que el marco estructural de las zonas de cizallamiento está hecho predominantemente de lineamientos de orientación NW a NNW y NE a NNE. La familia de orientación NW-NNW está relacionada con la tectónica frágil y la familia de orientación NE-NNE coincide con la trama dúctil Precámbrica de las rocas cristalinas del basamento. Un acuífero poroso superficial relacionado al regolito y a depósitos sedimentarios no consolidados recientes, con valores de resistividad < 1.372 Ohm.m y profundidades <30 m presenta un buen potencial para el almacenamiento de agua subterránea. Sin embargo, los resultados no son concluyentes sobre el significado hidrogeológico de las estructuras tectónicas para la prospección de aguas subterráneas en el área de estudio.

PALABRAS CLAVE: recursos hídricos subterráneos, tomografía eléctrica de resistividad, lineamentos estructurales, macizo rocoso fracturado, acuífero poroso.

ABSTRACT

The Precambrian metamorphic rocks in the southern region of the Espírito Santo State (southeastern Brazil) is intercepted by ductile and brittle/ductile shear zones over which towns like Guaçuí, Marechal Floriano and Domingos Martins were established. In the years of 2014 to

*Corresponding author: marilane.melo@ufes.br

[2] Departamento de Geologia Aplicada, Instituto de Geociências e Ciências Exatas, Universidade Estadual Paulista. estado de São Paulo, Brasil

1 Departamento de Geologia. Centro de Ciências Naturais e da Saúde, Universidade Federal do Espírito Santo, estado do Espirito Santo, , Brasil

2016 the Espírito Santo State faced the worst drought in the past 80 years. In situations like that, the only source of fresh water available is underground. Therefore, the purpose of this study was to integrate multisource data for groundwater prospecting and management. The study area comprises the central sectors of the Guaçuí and Batatal shear zones. Methodology involved the interpretation of stereo-pairs for the identification of lineaments, electrical resistivity surveys and geological fieldwork. The results were tentatively validated with available groundwater well production data. Six resistivity profiles with a total length of 2,400 m were surveyed and 15 outcrops were described across these structures. Results have shown that the structural framework of the shear zones is predominantly made of NW to NNW and NE to NNE-trending lineaments. The former is related to brittle tectonics and the latter coincides with the ductile Precambrian fabric of the crystalline basement rocks. A near-surface porous aquifer regarded to the regolith and recent unconsolidated sedimentary deposits presenting resistivity values < 1,372 Ohm.m and depths < 30 m have good potential for groundwater storage. However, results are not conclusive about the hydrogeological significance of tectonic structures for groundwater prospection in the study area.

KEY WORDS: groundwater resources, electrical resistivity tomography, structural lineaments, fractured rock mass, porous aquifer.

INTRODUCTION

In rural and urban areas three sources of fresh water resources for human consumption may be available: (a) rivers and water reservoirs; (b) porous aquifers (i.e. soil and sedimentary units); and (c) fractured rock aquifers (Freeze and Cherry, 1979; ANA, 2005). In regions where basement rocks outcrop, groundwater accumulates in opened planar structural features (i.e. joints, faults, foliation, veins, etc.), which serve as a complex conduit-barrier system.

Fractured rock aquifers are controlled by fracture properties such as aperture, spacing (or fracture density), orientation, infillings (e.g. sand, clay, cemented, etc.), roughness (particularly for fractures with small apertures), connectivity, state of stress and nature of host rocks (Costa, 2008; Fernandes, 2008; Singhal and Gupta, 2010; Bense *et al.*, 2013). Fracture network facilitates chemical weathering and dissolution of host rock increasing hydraulic conductivity and groundwater storage (Hiscock, 2005; Brassington 2007).

Unlike fractured aquifers, the literature about the hydrogeological characteristics of rock aquifers related to Precambrian shear zones in Brazil is deficient (Neves and Morales, 2006). Shear zones are tabular regions of concentrated deformation across which adjacent undeformed rock units are offset (Alsop and Holdsworth, 2004). They are linear to curvilinear structures whose length is much greater than width. They are recognized at all scales and can be classified into brittle, ductile and brittle-ductile. Brittle shear zones are characterized by an array of parallel to subparallel fractures and veins, formed under fracturing, brecciation and cataclastic processes in the upper Earth's crust (< 10 km). Ductile shear zones are characterized by the presence of mylonitic rocks, where crystal-plastic deformation processes take place. Typically, such processes occur in the middle to lower Earth's crust. Brittle-ductile shear zones comprise features from both endmembers (Hobbs *et al.*, 1976).

Metamorphic rocks exposed in the southern region of the state of Espírito Santo (Brazil) are cut by the Guaçuí and Batatal NE-trending shear zones (Figure 1). These outstanding structures are tens of kilometers long and can be easily traced from remote sensing and aerogeophysical data (Silva, 2010). From 2014 to 2016 the Espírito Santo state faced the worst drought in the last 80 years according to government agencies, which resulted in water supply problems and economic losses. Some important locations lay over these features, such as the Guaçuí, Marechal Floriano and the tourist town of Domingos Martins. Population of the three towns combined reach 81,000 inhabitants and land has been extensively used for cattle raising and coffee and eucalyptus plantations (https://cidades.ibge.gov.br/).

In this sense, the aim of this paper is to investigate the hydrogeological significance of these shear zones for groundwater prospecting and management. The use of remote sensing data for the analysis of landforms associated to subsurface geophysical surveys can elucidate the hydrogeological complexity of fractured aquifer system in regions where basement rocks outcrop (Fernandes, 2008; Singhal and Gupta, 2010). Besides, it can assist the conservation of areas of aquifer recharge and the identification of groundwater reservoirs (Dottridgea & Jaber, 1999; Rubin and Hubbard, 2005; Yabel *et al.*, 2015; Salles *et al.*, 2018; Sandoval & Tibujan Jr., 2019). In view of this, we integrate geophysical, remote sensing and geological and structural data.

STUDY AREA

REGIONAL GEOLOGY AND TECTONICS

The Araçuaí orogen, located in southeastern Brazil, and its African counterpart, the West Congo belt, constitute an orogenic system that developed during the Brasiliano-Pan-African orogeny between the margins of the São Francisco and Congo cratons (Alkmim *et al.*, 2006). The Araçuaí-West Congo orogen (A-WC orogen) was formed during the amalgamation of Western Gondwana in Late Neoproterozoic time and split into two parts by the opening of the South Atlantic Ocean in the Cretaceous. The Araçuaí orogen comprises rift-related to distal passive margin sequences, ophiolitic remnants of the precursor Macaúbas basin, Rio Doce magmatic arc-related rocks and pre-collisional to post-collisional intrusions - G1 to G5 Supersuits (Pedrosa-Soares *et al.*, 2011). Paleoproteroic to Archean basement rocks include high-grade metamorphic rocks included in the Caparaó, Juiz de Fora, Ipanema, Guanhães and Serra do Valentim complexes. These represent reworked rocks related to the São Francisco Craton (Vieira *et al.* 2015; Alkmim *et al.* 2006).

The Guaçuí and Batatal NE-trending shear zones are one of the most strikingly geological features encountered in the southern region of the Espírito Santo State and can be easily traced from satellite images and aerogeophysical data for tens to hundreds of kilometers (Figure 1). These geological structures were formed in the final tectonic stages of the A-WC orogen (Pedrosa-Soares *et al.*, 2001; Alkmim *et al.* 2006).

The Guaçuí and Batatal shear zones cross paragneisses belonging to the Paraíba do Sul Complex and pre to late-tectonic granitoids (Vieira, 1997). The Guaçuí Shear Zone (GSZ) is 350 km long and 5 km wide on average and is comprised of mylonites (outer margins) and ultramylonites (core region), showing subvertical mylonitic foliation. The GSZ is a right-lateral ductile shear zone developed under high-grade metamorphism (Cunninghan *et al.*, 1998; Horn, 2007). The Batatal Shear Zone (BSZ) is 70 km long and comprise mylonitic foliation, being interrupted to the south by the post-collisional Iconha pluton (Féboli, 1993; Silva, 2010). According to Silva (2010), the BSZ is a brittle-ductile shear zone originated under low to medium-grade metamorphism.

After a long period of tectonic stability, the Araçuaí-West Congo orogenic belt was broke apart due to the opening of the Atlantic Ocean in the Cretaceous. This tectonic event was responsible for the intrusion of mafic magmatism, uplift of the Serra do Mar mountain range (to the south), reactivation of inherited geological structures and the development of marginal sedimentary basins, such as the Espírito Santo and Campos basins (Almeida, 1976). The Meso-Cenozoic brittle tectonics in the Brazilian southeastern margin was investigated by many authors (Riccomini, 1995, Ferrari, 2001, Zalán & Oliveira, 2005, Silva & Melo, 2011). In the Espírito Santo State, Ribeiro (2010) and Hartwig and Bozzi (2019) recognized three brittle deformation phases responsible for landform development and deformation of the semi-consolidated sediments of the Barreiras Formation (Miocene). Calegari *et al.*, (2016) recognized a NW-trending Lineament in the Espírito Santo southeastern margin, named as the Alegre Fracture Zone, originated in the Cambrian Period and reactivated in the Cenozoic Era. Lourenço *et al.* (2016) obtained similar results for the Piúma lineament, a 70 km long and N50W-trending brittle shear zone. Maizatto *et al.* (2009) apud Chemale Jr & Hadler (2005) based on apatite fission tracks analysis, recognized an important tectonic event during 80-60 Ma in the south-central Espírito Santo State, which caused a regional uplift that reached up to 3,000 m.

Few stress data are available for the southern Brazil (Lima *et al.*, 1997). According to the authors, measurements obtained from breakout for 145 wells in the Campos, Santos and Espírito Santo offshore basins are too scattered to define a regional SH_{max} orientation.

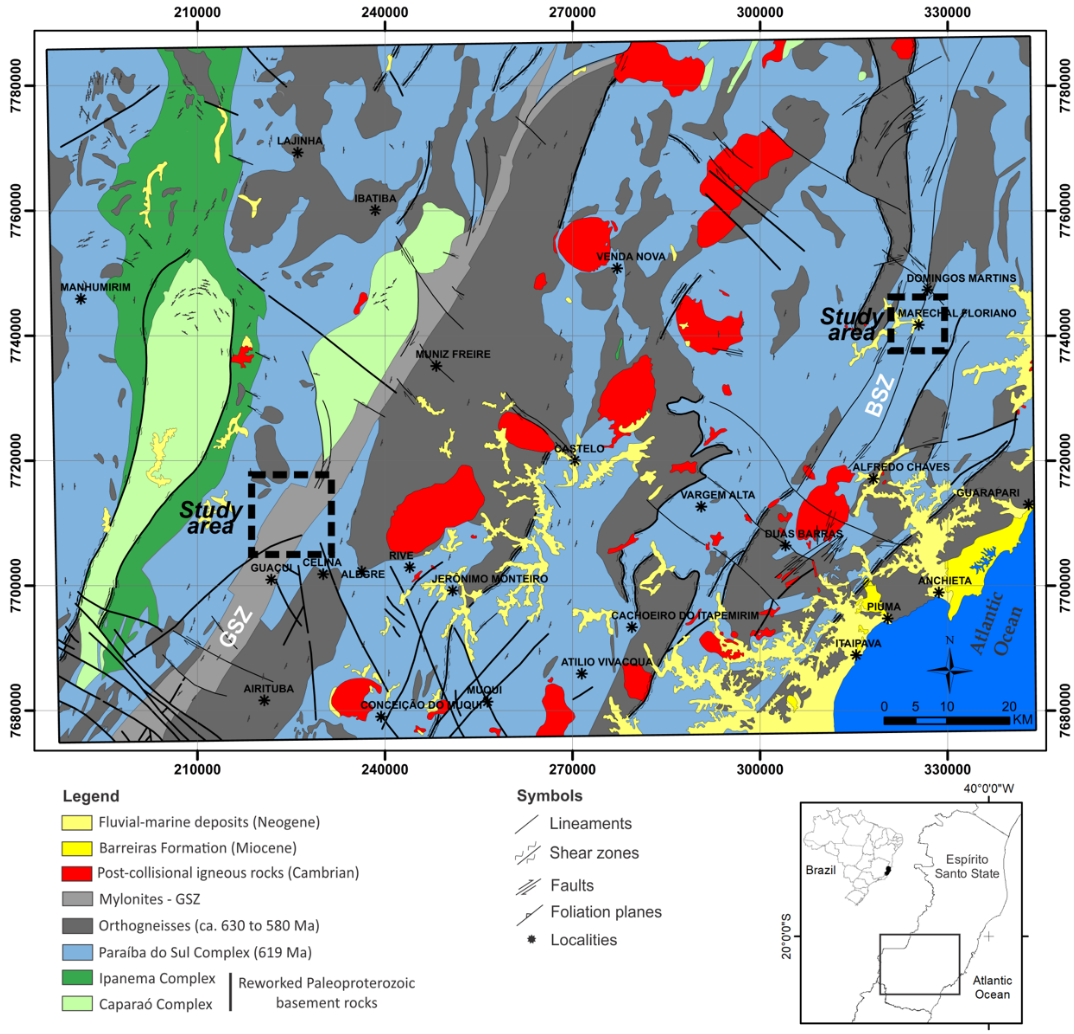

Figure 1. Regional geology of the study area based on Vieira (1997).

SOILS AND LANDFORMS

Landforms in the study area are included in the Mantiqueira Northern Plateau geomorphological unit (Gatto *et al.* 1983). They are structurally controlled by NE to NNE-trending lineaments inherited from basement rocks as well as NW-trending lineaments. Hilly landforms with rounded summits and gentle to steep slopes predominate. Landscape is marked by a regional plateau around 700 m.a.s.l amid which rocky domes emerge, reaching elevations up to 1,700 m.a.s.l. These are usually associated to post-collisional igneous rocks.

Alluvium deposits are associate to the drainage system. They are made of a mixture of gravel, sand and clay (Vieira, 1997). Soil profile can reach tens of meters in regions where elevations are moderate to gentle and gneissic rocks occur. Soil is described as red and yellow latosols, podzols and cambisols (Panoso *et al.* 1978). Colluvium soils and talus are observed close to rock domes, which are very common in landscape.

CLIMATE AND SURFACE HYDROLOGY

According to Köppen climate classification, Guaçuí town has an Aw (tropical savanna) climate type and Domingos Martins town has a Cfa (humid subtropical) climate type (https://pt.climate-data.org/). Guaçuí and Domingos Martins towns have average annual temperature around 21 degrees Celsius and average precipitation around 1,200 mm/year, with rainfalls occurring preferentially between October and March. The driest month occur in June and the rainiest month occur in December.

Drainage network is structurally controlled (Vieira, 1997). Itabapoana and Jucu rivers are the regional base level in the Guaçuí and Domingos Martins areas, respectively. Domingos Martins municipality has currently two small hydroelectric power stations in operation (< 30 MW) in the Jucu river and Guaçuí municipality has one (55 MW) in the Itabapoana river (www.annel.gov.br). River levels oscillate few meters along the year as a function of rainfall and seasons.

MATERIALS AND METHODS

The methodology of this work involved the integration of remote sensing, structural and electrical resistivity data (Madrucci *et al.*, 2005; Fernandes, 2008; Francese *et al.* 2009). Cartographic data were georreferenced in ArcGIS 10.4 (ESRI, 2015) using the horizontal Datum WGS-84 and the UTM map projection (Zone 24S). All data surveyed in this work was overlapped and integrated in the ArcGIS software.

The first step consisted in the interpretation of aerial photographs of the extinct Brazilian Coffee Institute – IBC (scale 1:30,000) freely available for the state of the Espírito Santo at the GEOBASES portal (https://geobases.es.gov.br/imagens-es-ibc-gerca-1970). The ST4 WILD Heerbruggg stereoscope was used for photogeological analysis. 11 stereo-pairs were studied and integrated for the GSZ and 5 stereo-pairs were used for the BSZ. Photogeological interpretation followed the procedures described in Soares and Fiori (1976) and Arcanjo (2011). The focus of the photogeological analysis was the identification of lineaments, which represent favorable features for groundwater storage. The term lineament used in this work followed the definition presented by O'Leary *et al.*, (1976). Aerial photos were georeferenced based on the Divino de São Lourenço and Domingos Martins topographic maps – scale 1:50,000 (IBGE, 1977 and 1978) and satellite images from GoogleEarth.

Fieldwork included the description and classification of lithologies (Fettes & Desmons, 2014) and description and collection of structural data (McClay, 1991). Structural data orientation was interpreted based on Schmidt-Lambert stereograms (Hobbs *et al.* 1976). For the study of the GSZ, eight outcrops distributed in 16 km were described along the roads ES-185 and ES-387, between the district of Celina and the small town of Ibitirama (Figure 1). For the study of the BSZ, 7 outcrops distributed in 9.7 km were described along the road BR-262.

The electrical resistivity method has been largely used for the survey of groundwater in fractured aquifers (Gallas, 2003; Braga, 2016; Singh *et al.* 2019; Briški *et al.* 2020). Usually, fractures represent permeable zones filled with water and/or soil/chemically weathered rock. Thus, they tend to present lower values of resistivity in comparison with adjacent intact rock mass. The electrical resistivity prospecting consisted in the use of the DC Resistivity method through the electrical resistivity tomography technique in a Schlumberger electrode array, distributed along six profiles with 10 meters of electrode spacing. Six resistivity profiles with a total length of 2,480 m were surveyed. A total of 385 measurements were determined for the profiles 380 m long and 527 measurements for only one profile 580 m long. The maximum investigation depth reached up to 130 m. Geophysical survey lines were preferentially setted up in the outer margins and inner portions of the GSZ and BSZ. They are oriented parallel and perpendicular to these structures.

The geophysical equipment used was the Terrameter LS resistivity meter, manufactured by ABEM Instrument (Sweden), which consists of a single automated signal transmission and reception module, with 250 W of power, 1 μV resolution and maximum electric current of 2.5 A (ABEM 2012).

Data acquired in the field were processed in the RES2DINV computational program (Geotomo, 2003). The results comprise resistivity profiles of distance versus depth presented in logarithmic scale in which values are interpolated and displayed in intervals of colors. This program automatically determines a two-dimensional subsurface model, from resistivity or chargeability data obtained in electrical profiling tests (Griffiths & Barker 1993).

The 2D model used in the program divides the pseudo-section into rectangular blocks, which will represent the pseudo-section by adjusting the field measurements. This optimization aims to reduce the difference between the apparent resistivity values calculated and measured in the field by adjusting the resistivity of the block model. The difference between the values is expressed by the root mean squared error (RMS) and its product is represented as inversion models (Loke & Barker 1996).

In order to validate the results, an attempt was made by comparing geoelectric profiles with groundwater well production data freely available in the CPRM-SIAGAS portal at http://siagasweb.cprm.gov.br/layout/visualizar_mapa.php.

RESULTS

PHOTOGEOLOGICAL ANALYSIS OF AERIAL STEREO-PAIRS

Structural lineaments interpreted from aerial stereo-pairs for the GSZ are displayed in Figure 2. 1,148 lineaments were interpreted and are distributed in 120 km^2. Lengths varied from 52 m to 3,866 m; average value equals to 386 m. NW and NE-trending lineaments predominate, respectively. NE-trending lineaments are concentrated in the eastern and southern portions of the study area (Figure 2), which coincides with the main trace of the GSZ. The NW portion of Figure 2 shows a distinct structural pattern in terms of orientation and lineament density (aerial photos ES-23 - 4505 and ES-23 - 4506).

Structural lineaments interpreted from aerial stereo-pairs for the BSZ are displayed in Figure 3. 490 lineaments were interpreted and are distributed in 78 km^2. Lengths varied from 79 to 4,155 m;average value equals to 418 m. NW-trending lineaments predominate but are scattered between N295 to N335. Structural domains are not evident.

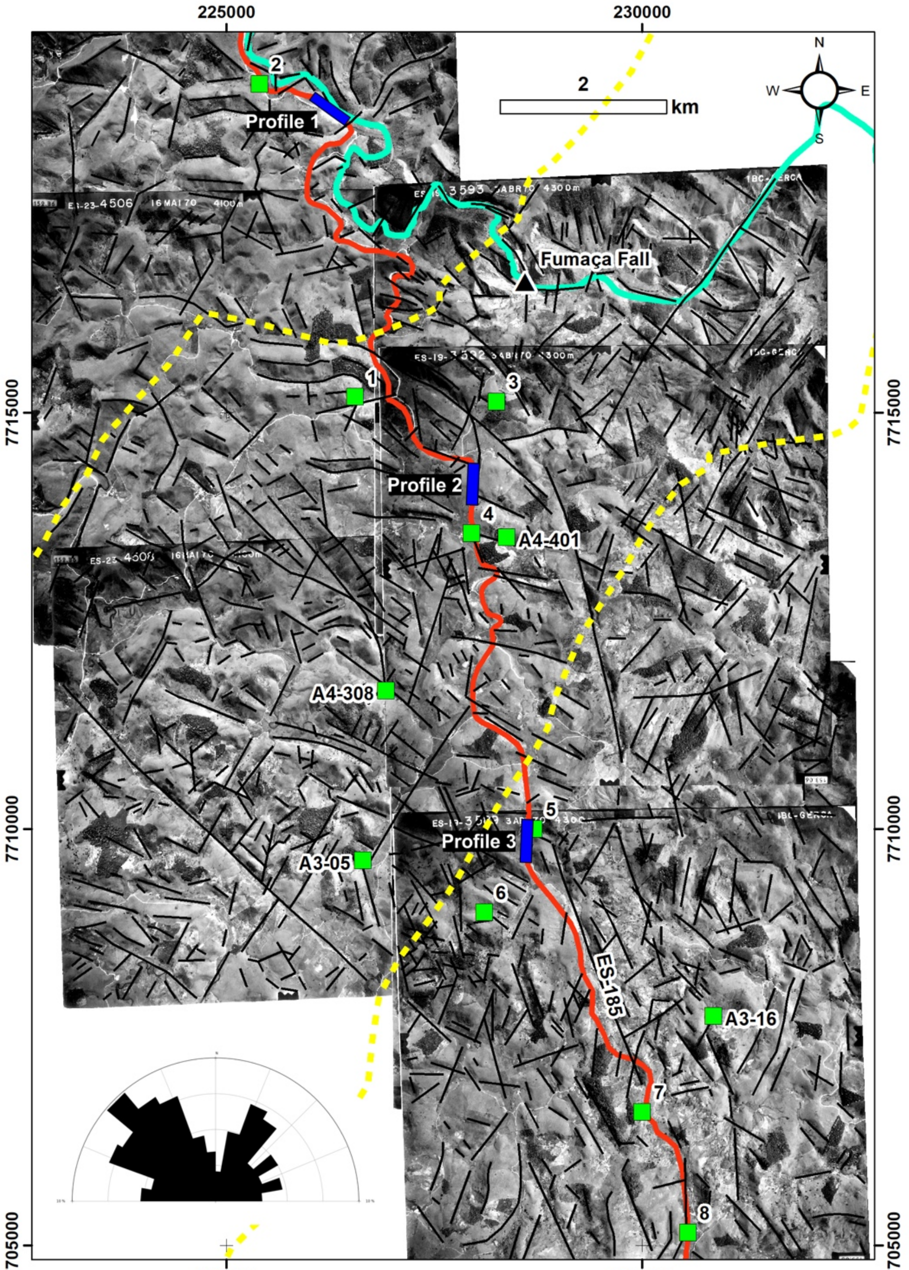

Figure 2. Structural map interpreted from aerial stereo-pairs for the BSZ with indication of the studied outcrops (labeled green boxes) and resistivity profiles (labeled blue rectangles). In the lower left corner, rose diagram display lineament orientations. Red line – roads and yellow dashed line – GSZ (after Horn, 2007).

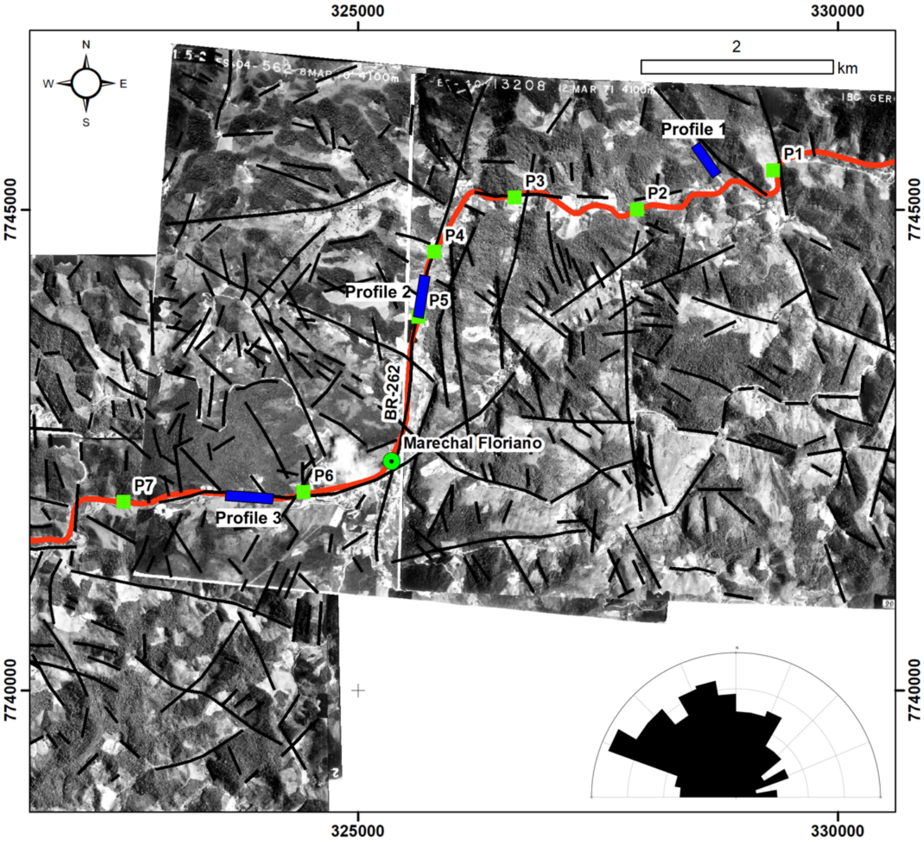

Figure 3. Structural map interpreted from aerial stereo-pairs for the BSZ with indication of the studied outcrops (labeled green boxes) and resistivity profiles (labeled blue rectangles). In the lower right corner, rose diagram display lineament orientations. Red line – road BR-262. According to Féboli (1993), the BSZ follow the Batatal river and passes through P4 and P5 rock outcrops.

FIELD GEOLOGICAL AND STRUCTURAL DATA

Fieldwork reveled three main lithotypes for the Guaçuí Shear Zone. In outcrop 8 occurs metagranites and in outcrops 1, 2 and 7, orthogneisses (Figure 2). In all the other outcrops are exposed mylonitic rocks (3, 4, 5, 6, A03-05, A03-16, A04-308 and A04-401). Besides, in one outcrop very close to Point 4 (UTM 24S 227154E/7713215S) a stromatic metatexite was also described. It shows a subvertical and penetrative foliation oriented parallel to the GSZ. Metagranites are coarse-grained and leucocratic rocks with weak foliation defined by mm-sized biotite crystals. Orthogneisses are course to fine-grained rocks and show remarkable cm-sized gneissic banding. Deformed mafic enclaves, few decimeters in size, and sparingly migmatized zones are also observed. Mylonitic rocks show typical cm to mm-sized mylonitic banding and numerous dextral kinematic indicators.

Figure 4 depicts stereograms of the planes of foliation along the cross-section studied. The results indicate that predominates strikes ranging from NNW to NNE and moderate to steep dip angles (45 - 64°) dipping predominantly to the east. Field observations across the GSZ revealed slightly fractured rock masses.

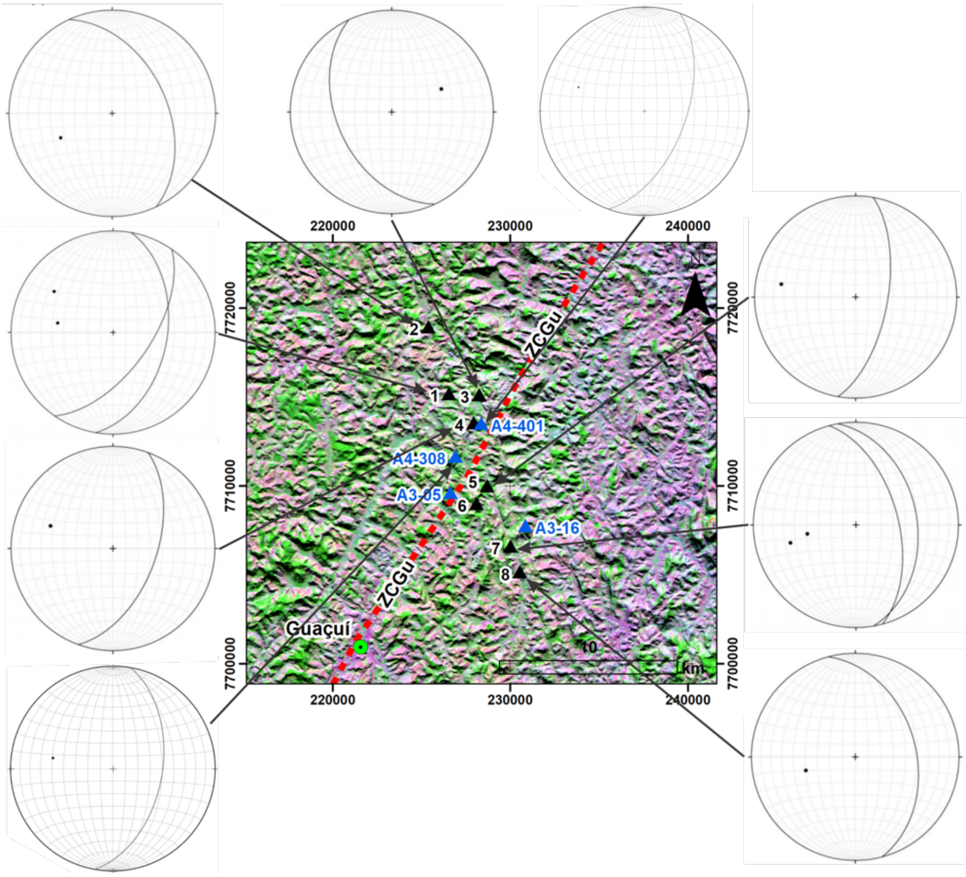

Figure 4. Stereographic projection of the planes of foliation across GSZ. Schmidt-Lambert net, lower hemisphere (equal area). Black triangles studied outcrops (this study) and blue triangles (Hartwig & Melo, 2019). Background image: Landsat-5 5R4G3B colored composition.

The transect course across the BSZ revealed coarse-grained garnet biotite gneiss, garnet metagranodiorite to metatonalite and calcisilicatic rocks. Gneissic banding is made of alternating and parallel mafic and felsic banding. Banding thickness ranges from 0.1 to 3.0 cm in hand specimens. Mafic bands are essentially made of biotite and garnet crystals and felsic bands are made of quartz, K-feldspar and plagioclase grains. A fine-grained banded calcisilicatic rock was identified in outcrop 3. Deformed mafic enclaves and sinistral kinematic indicators were observed in outcrop 6. A course-grained sillimanite-garnet gneiss was described in outcrop 7. Garnet metagranodiorites to metatonalites were recognized in outcrops 1, 2 and 5 and show a metamorphic foliation characterized by undulose films of biotite flakes (< 1 mm in diameter on average).

Figure 5 depicts stereograms of foliation along the cross-section studied. NE to NNE-trending foliation with dip angles ranging from 10 to 88° predominates. In outcrops 1, 2 and 3, a NW-trending foliation is observed with dip angles ranging from 20 to 60°. Outcrops described across the BSZ revealed slightly fractured rock masses.

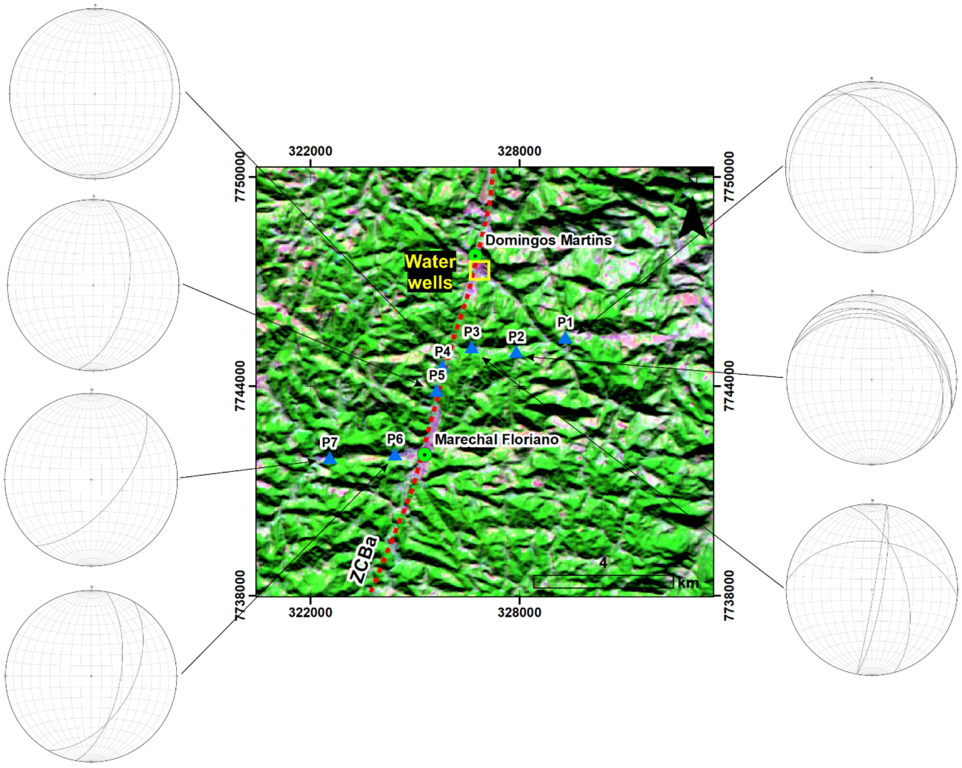

Figure 5. Stereographic projection of the planes of foliation across BSZ. Schmidt-Lambert net, lower hemisphere (equal area). Blue triangles, studied outcrops. Small yellow rectangle indicates the area where groundwater wells are distributed. Background image: Landsat-5 5R4G3B colored composition.

ELECTRICAL RESISTIVITY TOMOGRAPHY

Geophysical investigation depths ranged from 80 to 130 m for the Guaçuí Shear Zone (Figure 6). Resistivity profiles 1 and 3 are located in the west and east outer margins of the GSZ and resistivity Profile 2 is located within it (Figure 2). Resistivity profiles allow interpreting two geoelectrical layers. A superficial one regarded as soil/recent sedimentary deposits (containing groundwater or not) and a competent, unfractured and fresh rock mass (sound rock).

Resistivity profiles 1 and 2 show increasing values of electrical resistivity with depth ranging from approximately 117 to 16,070 Ohm.m. Resistivity profiles 1 and 2 show a saturated and discontinuous horizontal aquifer between elevations 710 and 660 m.a.s.l, exhibiting very low electrical resistivity values (< 117 Ohm.m). Resistivity Profile 3 shows a horizontal layer of very high electrical resistivity values (> 16,070 Ohm.m) between elevations 675 and 645 m.a.s.l, surrounded by moderate values of resistivity (~ 1,372 Ohm.m). The distribution pattern of the electrical resistivity isovalues under this layer may indicate the presence of a subhorizontal fracture. Lineaments interpreted from stereo-pairs are not evident in the resistivity sections of Figure 6 as disturbances in the distribution and magnitude of resistivity values are not discernable.

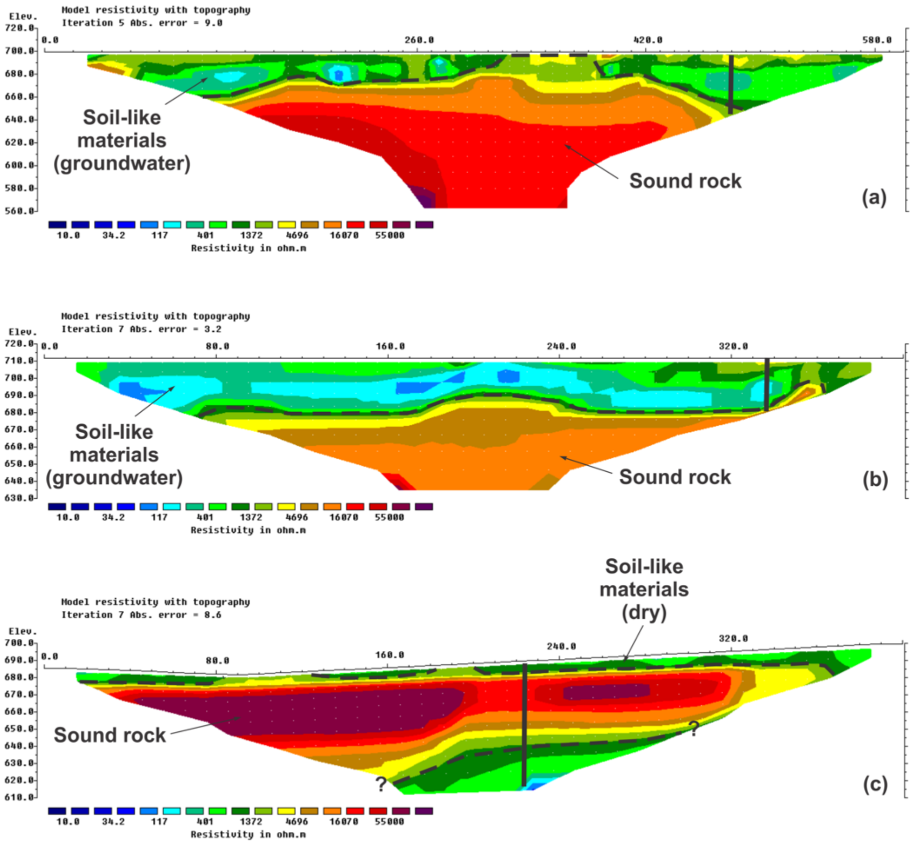

Figure 6. 2D eletrical resistivity imaging pseudosections for the GSZ in Ohm.m: (a) Resistivity Profile 1; (b) Resistivity Profile 2; and (c) Resistivity Profile 3. Dashed lines refer to geological contacts and fractures interpreted directly from resistivity sections, while continuous lines refer to lineaments based on the interpretation of stereo-pairs.

Geophysical investigation depths for the Batatal Shear Zone ranged from 75 to 85 m (Figure 7). Resistivity profiles are oriented parallel and perpendicularly to the main structural trends. Resistivity profiles 1 and 3 are located in the east and west outer margins of the BSZ while resistivity Profile 2 is within it (Figure 3). Resistivity Profile 1 shows in general average values of electrical resistivity (~ 1,372 Ohm.m) that indicate highly weathered rock masses (saprolite). Between electrodes located from 160 to 210 m, a huge elliptical spot of very high electrical resistivity is observed (55,000 Ohm.m) from elevations 515 to 485 m.a.s.l. Very high values of electrical resistivity indicate sound rock. Resistivity Profile 1 also indicates an irregular shaped layer (probably dry soil) dipping gently to the left.

Resistivity Profile 2 shows two regions of low values of electrical resistivity that indicate saturated soil/recent sedimentary deposits, separated by a central portion of high electrical resistivity values (> 4,696 Ohm.m). The vertical lineament interpreted from the stereo-pairs in the central portion of the section does not produce significant changes in the distribution pattern of resistivity isovalues.

Resistivity Profile 3 shows a superficial horizon of saprolite (1,372 Ohm.m) underlaid by sound rock (4,696 Ohm.m). Two spots of very high electrical resistivity values are observed (> 16,070 Ohm.m) between electrodes located at 180-210 m and 300-370 m. The central portion of resistivity Profile 3 also exhibits a distribution pattern of electrical resistivity values that suggests the presence of subvertical geological structures.

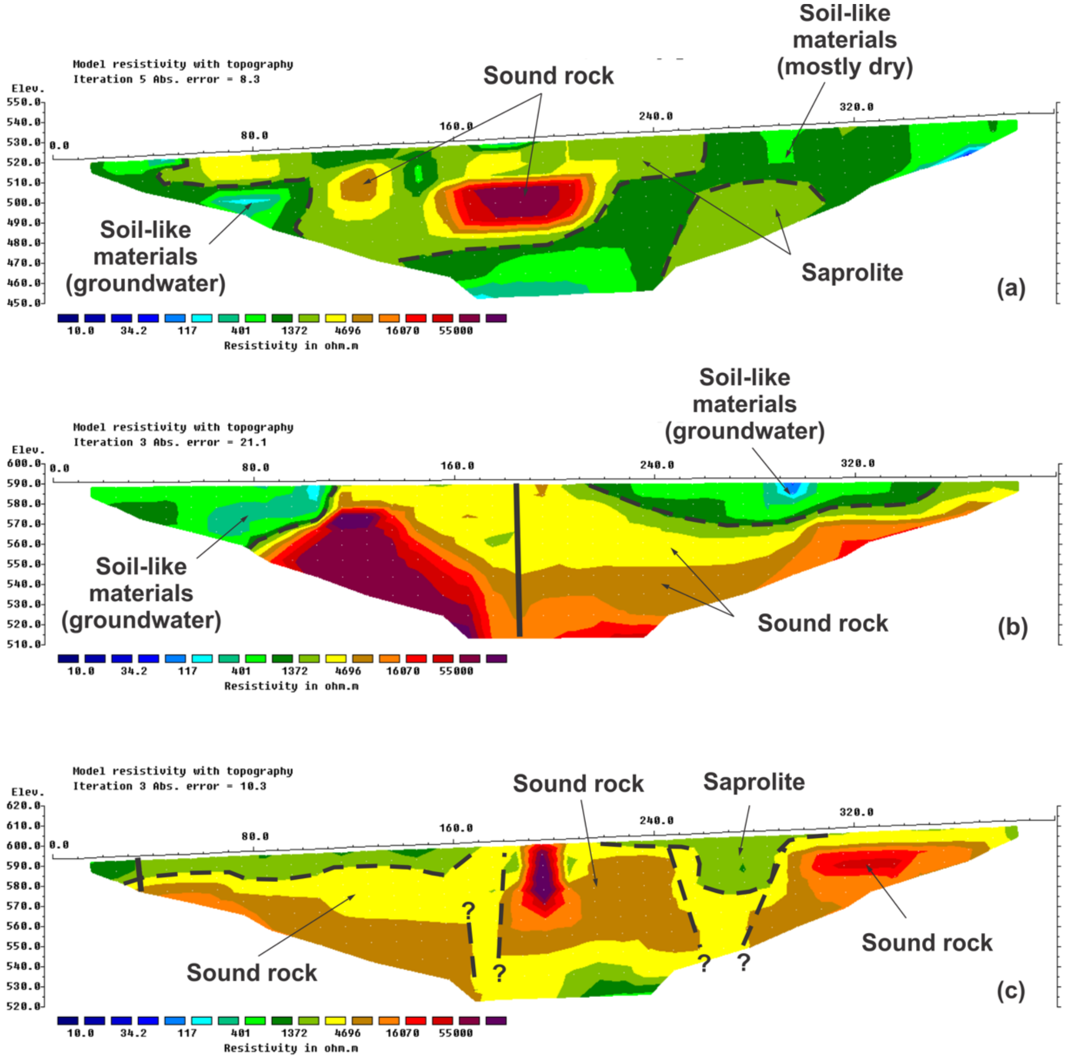

Figure 7. 2D eletrical resistivity imaging pseudosections for the BSZ in Ohm.m: (a) Resistivity Profile 1; (b) Resistivity Profile 2; and (c) Resistivity Profile 3. Dashed lines refer to geological contacts and fractures interpreted directly from resistivity sections, while continuous lines refer to lineaments based on the interpretation of stereo-pairs.

DISCUSSIONS

The geological interpretation of remote sensed data revealed that NW and NE-trending lineaments are the most important structures. NE-trending lineaments coincides with the orientation of ductile structures of the Precambrian crystalline basement rocks. NW-trending structures are associated to the opening and evolution of the South Atlantic Ocean (Calegrari *et al*., 2016; Lourenço *et al*., 2016). Hartwig and Bozzi (2019) recognized more than one hundred NW and NE-trending fractures in the semi-consolidate Miocene sediments of the Barreiras Formation in the southern margin of the Espírito Santo State showing that both sets were reactivated in recent times. For BSZ, the lineaments orientations are more scattered in comparison with the GSZ (Figures 2 and 3). Remote sensed data have also shown that the GSZ (9.5 lineaments/km^2) is more structured than the BSZ, (6.3 lineaments/km^2). Moreover, the GSZ is more strongly controlled by NE-trending lineaments.

Geological and structural field data revealed poorly fractured rock masses. Some fractures identified in the field are related to rock blasting and does not have hydrogeological significance. Foliations are predominantly oriented from NNW to NE for both shear zones. The GSZ shows a penetrative milonitic foliation while for the BSZ rocks show a weak metamorphic foliation with significant variations in dip angles.

Geophysical surveys clearly revealed a superficial porous aquifer in both shear zones, which is associated to low values of resistivity. Although the GSZ present numerous geological lineaments when viewed from stereo-pairs, resistivity sections have not confirmed their subsurface expression. One possible explanation for that may be due to their limited lengths. The low values of resistivity that appear bellow elevation 640 m.a.s.l. in Figure 6c seems to be related to exfoliation joints. These are widely regarded as forming in response to removal of overburden, associated to landform evolution (Hartwig, 2006; Hobbs *et al.* 1976, Bahat *et al.* 1999).

Abrupt changes in the orientation of the resistivity isolines indicate a fractured rock mass for the BSZ (Figure 7c). However, these structures seem to be related to sealed (closed) fractures as high resistivity values (> 4,696 Ohm.m) predominate elsewhere. Telford *et al.* (1990) present examples of electrical resistivity values for common rocks and minerals. Considering geological fieldwork data, it is possible to interpret that the distribution and magnitude patterns of resistivity values observed in Figure 7c may be related to faciological differences in crystalline basement rocks.

According to Costa (2008) and Fernandes (2008) not only the degree of fracturing, but also the principal horizontal stress orientation control groundwater storage and flow in fractured aquifers. Ribeiro (2010) studied the brittle tectonics of the Barreiras Formation in the southern margin of the Espírito Santo state and recognized NW-oriented sinistral strike-slip faults. According to the author, they were originated by extensional stress-oriented NE-SW, associated to a Quaternary E-W-trending dextral strike-slip tectonic regime. Therefore, if this state of stress was still active, groundwater would be more likely retained in NW-trending lineaments.

Groundwater production data from tube wells is available only for the BSZ (Table 1). Ten groundwater wells are distributed in Domingos Martins urban area (Figure 5). Well production data is available for only five of them. Flow rates for these water wells ranged from 0.4 to 19.8 m^3/h. It is worth mentioning that all groundwater wells lay over a long NW-trending lineament (Figure 5). However, information regarding the geology crossed by these wells and filter positions was not provided.

Figure 8 summarizes rock mass conceptual models for groundwater prospection for both the GSZ and the BSZ. A potential superficial porous aquifer is regarded to unconsolidated sedimentary deposits and/or soil cover (regolith). This are concentrated in the first 30 meters below surface and is well developed in the GSZ (Figures 6a,b). Although it is easily exploited for human consumption, it is also very vulnerable to pollution, especially from wastewater (Bertossi *et al.* 2013). Poorly fractured rock masses are associated to the GSZ and fractured rock masses were recognized for the BSZ (Figure 7c). Nevertheless, discontinuities seem to be sealed (closed) as high resistivity values (> 4,696 Ohm.m) predominate elsewhere.

Table 1. Well production data for the BSZ. Source: CPRM-SIAGAS.

Well codes	Locality	E (m)	N (m)	Flow rate (m^3/h)
3100016741	Campinho- Domingo Martins	326,741.2	7,747,191.8	19.8
3100016744	Campinho-Domingos Martins	326,971.61	7,747,347.9	0.4
3100016745	Campinho-Domingos Martins	326,970.99	7,747,409.45	6
3100016746	Campinho- Domingos Martins	327,03028	7,747,287.05	2.8
3100016747	Campinho-Domingos Martins	327,001.87	7,747,225.2	3

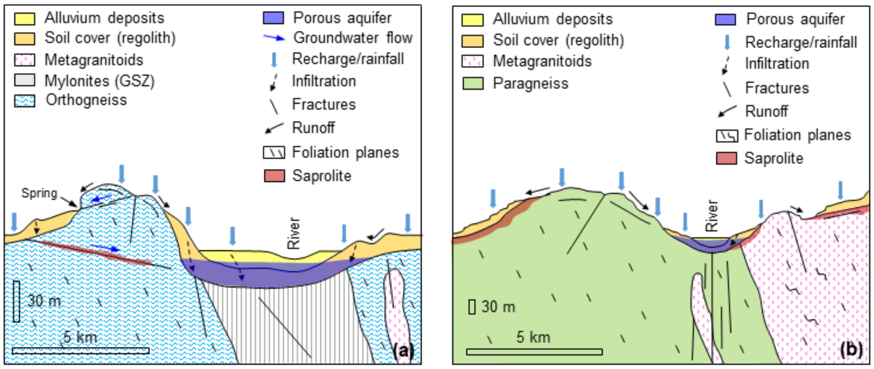

Figure 8. Rock mass conceptual model for groundwater prospection for the GSZ (a) and the BSZ (b).

CONCLUSIONS

The aim of this paper was to investigate the hydrogeological significance for groundwater prospecting of two Precambrian NE-trending shear zones, located in the southern region of the Espírito Santo State (Southeastern Brazil).

Based on the results, a porous near-surface aquifer has good potential for groundwater storage, especially in the GSZ. The GSZ and the BSZ are intercepted by numerous lineaments preferentially oriented to NE-NNE and NW-NNW. The former is associated to ductile Precambrian tectonics (Araçuaí-West Congo Orogen) while the latter to Meso-Cenozoic brittle tectonics. However, integrated data is not conclusive about the hydrogeological significance of brittle and ductile discontinuities for groundwater prospection. The resistivity profiles and available water well data did not confirm the occurrence of groundwater associated with them, which may be due to the amount of surveyed data, state of stress, etc. Authors recommend more investigations in the north and south sectors of the GSZ and the BSZ in order to better understand the hydrogeological significance of these geological features.

REFERENCES:

ABEM, 2012, Terrameter LS - Instruction Manual. ABEM Instrument AB: Sundbyberg, 1-122.

Almeida F.F.M.de., 1976, The System of Continental Rifts bordering the Santos Basin, Brazil. *An. Acad. Bras. Ciênc.*, 48, 15-26.

ANA – Agência Nacional das Águas. Disponibilidade e demandas de recursos hídricos no Brasil. Available on: < http://arquivos.ana.gov.br/planejamento/planos/pnrh/VF%20DisponibilidadeDemanda.pdf> Access on: November 10, 2019.

Alkmim F.F., Marshak S., Pedrosa-Soares A.C., Peres G.G., Cruz S.C.P., Whittington A., 2006, Kinematic evolution of the Araçuaí-West Congo Orogen in Brazil and Africa: nutcracker tectonics during the Neoproterozoic assembly of Gondwana. *Precambrian Research*, 149, 43-64.

Arcanjo J. B. A., 2011, Fotogeologia: conceitos, métodos e aplicações. CPRM/SGB, Salvador. Brasil, 144.

Alsop G.I., Holdsworth R.E., 2004, Shear zones — an introduction and overview. Geological Society, London, Special Publications, 224, 1-9. https://doi.org/10.1144/GSL.SP.2004.224.01.01.

Bahat D., Grossenbacher K., Karasaki K., 1999, Mechanism of exfoliation joint formation in granitic rocks, Yosemite National Park. *Journal of Structural Geology*, 21, 85-96.

Bense, V.F., Gleeson T., Loveless S.E., Bour, O., Scibek, J., 2013, Fault zone hydrogeology. *Earth-Science Reviews*. v. 127. p. 171-192.

Bertossi, A. P. A., Cecílio, R.A., Neves, M.A., Garcia, G,O. 2013. Qualidade da água em microbacias hidrográficas com diferentes coberturas do solo no sul do Espírito Santo. *Rev. Árvore*, v. 37, n. 1, p. 107-117.

https://doi.org/10.1590/S0100-67622013000100012.

Braga, C.O. Geofísica Aplicada: Métodos Geoelétricos em Hidrogeologia. São Paulo: Editora Oficina de Textos. 2016, 159.

Brassington R., 2007, Field Hydrogeology. Chichester, Jonh Wiley & Sons, 312.

Briški M., Stroj A., Kosović I., Borović S., Characterization of aquifers in metamorphic rocks by combined use of electrical resistivity tomography and monitoring of spring hydrodynamics. *Geosciences*, 10, 137, 2-18. doi:10.3390/geosciences10040137.

Calegari S.S., Neves M.A., Guadagnin F., França G.S., Vincentelli M.G.C., 2016, The Alegre Lineament and its role over the tectonic evolution of the Campos Basin and adjacent continental margin, southeastern Brazil. *Journal of South American Earth Sciences*, 69, 226-242.

Costa W.D., 2008, Hidrogeologia dos meios fraturados. In: Feitosa, A.C., Filho, J.M., Feitosa, E.C., Demetrio, J.G.A. *Hidrogeologia: conceitos e aplicações*. 3ª Ed. Rio de Janeiro: CPRM/LABHID, 121-151.

Cunningham, D.; Alkmim, F.F.; Marsakh, S., 1998, A structural transect across the coastal mobile belt in the Brazilian Highlands (latitude 20°S): the roots of a Precambrian transpressional orogen. *Precambrian Research*, 92, 251-275.

Dottridgea J., JABER N.A., 1999, Groundwater resources and quality in northeastern Jordan: safe yield and sustainability. *Applied Geography*, 19, 4, 313-323. https://doi.org/10.1016/S0143-6228(99)00012-0.

Gatto L.C.S.; Ramos V.L.S.; Nunes B.T.A.; MamedE L.; Góes M.H.B.; Mauro C.A.; Alvarenga S. M.; Franco E. M. S.; Quirico A. F.; Neves L. B. Geomorfologia. In: Projeto RADAMBRASIL, Folhas SF.23/24 Rio de Janeiro/Vitória; geologia, geomorfologia, pedologia, vegetação e uso potencial da terra, Rio de Janeiro, IBGE. 1983, 305-384.

ESRI 2015. ArcGIS Desktop: Release 10.4. Redlands, CA: Environmental Systems 498 Research Institute.

Fernandes A.J., 2008, Aquíferos fraturados: uma revisão dos condicionantes geológicos e dos métodos de investigação. *Revista do Instituto Geológico*, 29, 1/2, 49-72.

Féboli W.L. (Org.)., 1993, Programa de Levantamentos Geológicos Básicos do Brasil. Texto Explicativo e Carta Geológica – escala 1:100.000, Folha Domingos Martins-ES – SF.24-V-A-III. DNPM/CPRM., 179.

Ferrari A.L., 2001, Evolução tectônica do Gráben da Guanabara. PhD thesis. Universidade de São Paulo. São Paulo, 412.

Fettes D., Desmons J., 2014, Rochas metamórficas: classificação e glossário. Tradução de: Neto, J.M.R. São Paulo: Oficina de Textos, 313.

Francese R., Mazzarini F., Bistacchi A., Morelli G., Pasquarè G., Praticelli N., Robain H., Wardell N., Zaja A., 2099, A structural and geophysical approach to the study of fractured aquifers in the Scansano-Magliano in Toscana Ridge, southern Tuscany, Italy. *Hydrogeology Journal*, 17, 1233-1246.

Freeze R.A., Cherry J.A., 1979, Groundwater. New Jersey, U.S.A: Prentice-Hall, 604.

Gallas J.D.F., 2003, Prospecção de água subterrânea em aquíferos cristalinos com o emprego de métodos indiretos. *Revista do Instituto Geológico*, 24, 1/2, 43–51.

GEOTOMO SOFTWARE, 2003, RES2DINV (v.3.54) for 98/ME/2000/NT/XP. Geoelectrical Imaging 2D and 3D.

Griffiths D.H., Barker, R.D., 1993, Two-dimensional resistivity imaging and modelling in areas of complex geology. *Journal of Applied Geophysics*, 29, 211-226. https://doi.org/10.1016/0926-9851(93)90005-J.

Hartwig M.E., Bozzi A.H.R., 2019, Análise neotectônica da Formação Barreiras na porção sudeste do estado do Espírito Santo. In: XVII Simpósio Nacional de Estudos Tectônicos. *Anais*… Bento Gonçalves, Brasil, SBG, 26, 29, 148.

Hartwig M. E., Melo M. G., 2019, Sobre o Lineamento Guaçuí em seu segmento central: aspectos metamórficos e microestruturais. In: XVII Simpósio Nacional de Estudos Tectônicos. *Anais*… Bento Gonçalves, Brasil, SBG, 26, 29, 15.

Hartwig M.E., 2006, Tectônica rúptil mesozoica-cenozoica na região da Serra dos Órgãos, RJ. Master thesis. Universidade de São Paulo, São Paulo, 117.

Hiscock K.M., 2005, Hydrogeology: principles and practice. Oxford, Blackwell Publishing, 405.

Hobbs B.E., Means W.D., Williams P.F., 1976, An outline of structural geology. Wiley, New York, 571

Horn A.H, 2007, Programa Geologia do Brasil. Levantamentos Geológicos Básicos. Geologia da Folha Espera Feliz. Follha SF.24-V-A-IV. Escala 1:100.000. Brasília: CPRM., Brasil.

Instituto Brasileiro de Geografia e Estatística – IBGE, 1977, Folha Topográfica Divino de São Lourenço - Folha SF-24-V-A-IV-2. Escala 1:50.000, Brasil.

Instituto Brasileiro de Geografia e Estatística – IBGE, 1978. Folha Topográfica Domingos Martins - Folha SF-24-V-A-III-4. Escala 1:50.000., Brasil.

Lima C., Nascimento E., Assumpção, M., 1997, Stress orientations in Brazilian sedimentary basins from breakout analysis: implications for force models in the South American plate. *Geophys. J. Int*, 130, 112-124.

Loke M.H., Barker R.D, 1996, Rapid least-squares inversion of apparent resistivity pseudosections by a quasi-Newton method. *Geophysical Prospecting*, 44, 131-152. doi: 10.1111/j.1365-2478.1996.tb00142.x

Lourenço F.S., Alkmim F.F., Araújo M.N.C., Romeiro M.A.T., Matos G.C., Crósta, A.P, 2016, The Piúma Lineament, southern Espírito Santo: structural expression and tectonic significance. *Brazilian Journal of Geology*, 46, 4, 531-546.

Madrucci V., Taioli F., Araújo C.C.D., 2005, Análise integrada de dados de sensoriamento remoto, geologia e geofísica no estudo de aqüífero fraturado, Lindóia-SP. *Revista Brasileira de Geofísica*, 23, 4, 437–451.

Maizatto J.R., Lana C.C., Ribeiro A.W.S., Ferreira E.P, 2008, Evidências de terras altas no Campaniano da bacia do Espírito Santo. *Boletim Geociências Petrobrás*, 17, 1, 31-43.

Mcclay K. R., 1991, The mapping of geological structures. Chichester: Wiley, 161.

Medeiros Júnior, E. B. 2016. Evolução petrogenética de terrenos granulíticos nos estados de Minas Gerais e Espírito Santo. Tese de Doutorado, Escola de Minas, Universidade Federal de Ouro Preto, Ouro Preto.

Neves M. A., Morales, N, 2006, Well productivity-controlling factors in crystalline terrains of Southeastern Brazil. *Hydrogeology Journal*, 15, 471-482.

O'leary D. W., Friedman J. D., Pohn, H. A, 1976, Lineament, linear, lineation: some proposed new standards for old terms. *Geological Society American Bulletin*, 87, 1463 – 1469.

Panoso L.A., Gomes L.A., Pires Filho A.M., Bonelli S, 1978, Levantamento de reconhecimento de solos do Estado do Espírito Santo. Rio de Janeiro: EMBRAPA-SNLCS., 461 (Boletim Técnico Nº 45)

Pedrosa-Soares A.C., De Campos C.P., Noce C., Silva L.C., Novo T., Roncato J., Medeiros S., Castañeda C., Queiroga G., Dantas E., Dussin I., Alkmim F, 2011, Late Neoproterozoic–Cambrian granitic magmatism in the

Araçuaí orogen (Brazil), the Eastern Brazilian Pegmatite Province and related mineral resources. Geological Society of London, Special Publication., 350, 25–51.

Pedrosa-Soares A.C., Noce C.M., Wiedemann C., Pinto C.P, 2001, The Araçuaí-West Congo Orogen in Brazil: an overview of a confined orogen formed during Gondwanaland assembly. *Precambrian Research.* 110, 307–323.

Ribeiro C. S, 2010, Influência da tectônica pós-deposicional na distribuição da Formação Barreiras entre o rio Paraíba do Sul (RJ) e o rio Doce (ES). Master thesis. Universidade Federal do Rio de Janeiro – UFRJ, 165.

Riccomini C, 2005, Padrão de fraturamento do maciço alcalino de Cananéia, estado de São Paulo: relações com a tectônica mesozóico-cenozóica do sudeste do Brasil. Revista Brasileira de Geociências. 1995, 25, 2, 79-84.

Rubin Y.; Hubbard S.S. Hydrogeophysics. Dordrecht, Springer, 527.

Salles L.A., Lima J.E.F.W, Roig H.L., Malaquias, V, 2018, Environmental factors and groundwater behavior in an agricultural experimental basin of the Brazilian central plateau. *Applied Geography*, 94, 272-281. doi: 10.1016/j.apgeog.2018.02.007

Sandoval J.A., Tiburan JR. C.L, 2019, Identification of potential artificial groundwater recharge sites in Mount Makiling Forest Reserve, Philippines using GIS and Analytical Hierarchy Process. *Applied Geography*, 105, 73-85. doi: 10.1016/j.apgeog.2019.01.010.

Silva C. M. T., 2010, O sistema transcorrente da porção sudeste do orógeno Araçuaí e norte da faixa Ribeira: geometria e significado tectônico. Ph.D Thesis. Universidade Federal de Ouro Preto, 221.

Silva T. P. de, Mello C.L, 2010, Reativações neotectônicas na zona de cisalhamento do Rio Paraíba do Sul (Sudeste do Brasil). *Revista do Instituto de Geociências*, São Paulo, 11, 1, 95-111.

Singh, K.K.K., Bharti, A.K., Pal, S.K. et al, 2019, Delineation of fracture zone for groundwater using combined inversion technique. *Environ Earth Sci,* 78, 110. https://doi.org/10.1007/s12665-019-8072-z

Singhal B.B.S., Gupta R.P, 1976, Applied hydrogeology of fractured rocks. 2nd ed. New York: Springer. 2010, 408.

Soares P. C.; Fiori A. P. Lógica e Sistemática na Análise e Interpretação de Fotografias Aéreas em Geologia. Notícia Geomorfológica, Campinas. 16, 32, 71-104.

Telford, W.M., Geldart, L.P., Sheriff, R.E. 1990. Applied Geophysics. 2ed. Cambridge: University Press. 770p.

Vieira V.S., Silva M.A. Da, Correa T.R., Lopes N.H.B, 2015, Geologia e Recursos Minerais do Estado do Estado do Espírito Santo. In: Programa Geologia do Brasil. Mapas Geológicos Estaduais, escala 1:400.000. Companhia de Pesquisa de Recursos Minerais (CPRM), Serviço Geológico do Brasil, Belo Horizonte. Brasil.

Vieira, V.S. (Org.), 1997, Programa de Levantamentos Geológicos Básicos do Brasil. Folha Cachoeiro do Itapemirim – SF.24-V-A. Estados do Espírito Santo, Minas Gerais e Rio de Janeiro, escala 1:250.000. Brasília, MME/SMM/CPRM., 99.

Yabel A., Fabro R., Guadalupe J., Ávila P., Alberich M.V.E., Sansores S.A.C. & Camargo-Valero M.A., 2015, Spatial distribution of nitrate health risk associated with groundwater use as drinking water in Merida, Mexico. *Applied Geography*, 65, 49-57. doi: 10.1016/j.apgeog.2015.10.004.

Zálan P. V., Oliveira J. A. B. de, 2005, Origem e evolução estrutural do Sistema de Riftes Cenozóicos do Sudeste do Brasil. *Boletim de Geociências da Petrobrás.* 13, 2, 269-300.

Original paper

THREE-DIMENSIONAL SHEAR-WAVE QUALITY FACTOR, QS(F), MODEL FOR SOUTH-CENTRAL GULF OF CALIFORNIA, MEXICO OBTAINED FROM INVERSION OF BROADBAND DATA

Sanjay Kumar[1]*, Anand Joshi[1], Raul R. Castro[2], Shri K. Singh[3], Sandeep Singh[1]

Received: May 8, 2020; accepted: December 2, 2020; published online: April 1, 2021.

RESUMEN

Se aplicó un esquema de inversión iterativo, inicialmente desarrollado por Hashida y Shimazaki (1984) y posteriormente modificado por Joshi *et al.*, (2010), para estimar el factor de calidad de onda corta tridimensional, *Qs (f)*, del centro-sur del Golfo de California, México. Es un área de 230 x 288 km que se divide en 108 bloques rectangulares de diferentes *Qs (f)*. Se utilizó 25 terremotos bien ubicados registrados en tres estaciones de banda ancha de la red regional RESBAN operada por CICESE (Centro de Investigación Científica y de Educación Superior de Ensenada, Baja California) y tres Sismógrafos de Fondo Oceánico (OBS, por sus siglas en inglés) de un conjunto del Experimento del Fondo Oceánico del Mar de Cortés (SCOOBA, por sus siglas en inglés). Este conjunto de datos permitió obtener estimaciones de *Qs (f)* de diferentes bloques, utilizando el algoritmo de inversión modificado. El *Qs (f)* se obtuvo a varias frecuencias en el rango de 0,16 ~ 8,0 Hz. Se encontró que la estructura *Qs* estimada se correlaciona con los modelos geológicos y tectónicos de la región propuestos en estudios previos. Se obtuvo una relación regional dependiente de la frecuencia que utiliza todos los valores de 1944 del factor de calidad de la onda de corte a 18 frecuencias diferentes en todos los bloques y se puede aproximar mediante una función de la forma $Qs\ (f) = 20\ f^{1.2}$. Esta relación es típica en una región tectónicamente activa con alta atenuación de onda *S* y es similar a las relaciones de atenuación reportadas por otros autores para la región del Valle Imperial, California.

PALABRAS CLAVE: *Qs*, atenuación, Golfo de California, Mexico, inversión de onda corta.

ABSTRACT

We apply an iterative inversion scheme, initially developed by Hashida and Shimazaki (1984) and later modified by Joshi *et al.,* (2010), to estimate three - dimensional shear - wave quality factor, $Q_s(f)$, of south-central Gulf of California, Mexico. An area of 230 km x 288 km in this region is divided into 108 rectangular blocks of different $Q_s(f)$. We use 25 well-located earthquakes recorded at three broadband stations of the regional network RESBAN operated by CICESE (*Centro de Investigación Científica y de Educación Superior de Ensenada, Baja California*) and three Ocean

---

*Corresponding author: sanjay.geokuk@gmail.com; anandfes@iitr.ac.in

[1] Department of Earth Sciences, Indian Institute of Technology Roorkee, Roorkee, Uttarakhand, India.

[2] Centro de Investigación Científica y de Educación Superior de Ensenada (CICESE), División Ciencias de la Tierra, Departamento de Sismología, Ensenada, Baja California, México.

[3] Instituto de Geofísica, UNAM, Ciudad Universitaria, México City, México.

Bottom Seismographs (OBS) of the Sea of Cortez Ocean Bottom Array (SCOOBA) experiment. This dataset permits us to obtain $Q_s(f)$ estimates of different blocks using the modified inversion algorithm. $Q_s(f)$ is obtained at various frequencies in 0.16 ~8.0 Hz range. We found that the estimated Q_s structure correlates with geological and tectonic models of the region proposed in previous studies. A regional frequency-dependent relation using all 1944 values of shear-wave quality factor is obtained at 18 different frequencies in all blocks can be approximated by a function of the form $Q_s(f) = 20 f^{1.2}$. This relation is typical in a tectonically active region with high *S*-wave attenuation and is similar to attenuation relations reported by other authors for the Imperial Valley, California region.

KEY WORDS: *Qs*, Attenuation, Gulf of California, Mexico, Shear-wave inversion.

INTRODUCTION

The Gulf of California (GoC) is obliquely rifted that connects the East Pacific rise spreading ridge in the south with the San Andreas Fault in California. The trans-tension between the North American and Pacific plates resulted in the generation of the large earthquakes in the GoC along with the transform faults and the spreading ridges (Castro *et al.,* 2011b; Castro *et al.,* 2017b). The earthquakes in this region follow a fairly linear trend along the southeastward direction from southern California to the southern end of the Gulf of California, Mexico. The transform faults are associated with right lateral strike slip faulting while normal faulting is observed near the spreading centres. The northern GoC comprises the complex transform fault geometry and is the major reason for large (Ms > 6) earthquakes in this region (Goff *et al.*, 1987, Castro *et al.,* 2017b). The observed mechanism of faulting in this region is oblique -normal faulting in nature (Persaud *et al.*, 2003, *Castro et al.,* 2017b). On the other hand, the southern GoC comprise the ridge transform fault system along with the hot zones under the weak crust is the dominant mode of rupturing to generate large (Mw: 7.0 (January 7, 1901)) earthquakes (Pacheco and Sykes, 1992). These factors along with the oblique plate motion also resulted in the rapid rupturing of southern region (Umhoefer 2012).

Seismic waves generated from an earthquake experienced the attenuation of wave amplitude at distant locations from the source. The attenuation rate of seismic wave amplitude is very sensitive to the presence of fluids in the rocks, temperature conditions, the composition of rocks and other factors, while propagating through the earth interior. Local geology or the site condition at a location also plays a key role during an earthquake by amplifying or attenuating the seismic waves at different sites. The seismic attenuation is described in terms of inverse of a dimensionless parameter known as the Quality factor (Knopoff 1964). In 1984, Hasida and Shimazaki introduced a technique to estimate the 3D *Q*-structure using the intensity data for Tohoku region, Japan. Later Satake and Hasida (1989) and Nakamura and Uetake (2002) has used this method to distinguish and understand the behaviour of low and high attenuation regions for north Island, New Zealand and Pacific sea plate, Japan. Besana *et al.*, (1997) has studied the regional effects of subsurface structures like arcs, slabs and continental material using the 3D *Q*-structure for Philippine region. Later, Nakamura and Uetake (2002) and Joshi *et al.,* (2010) has modified the technique and use the acceleration data to obtain the attenuation structure for Tohoku, Japan and Uttarakhand, India regions. Attenuation studies around the world based on Q^{-1} values have been used to characterize the tectonic regions e.g. stable, volcanic, and seismically active (Joshi *et al.,* 2010; Castro *et al.,* 2008; Kumar *et al.,* 2015). The less attenuating media in a region is characterized by the high *Q* value and the vice versa.

Various attempts have been made to understand the attenuation behaviour of seismic waves in GoC and the surrounding region. For the southern region, Ortega and González (2007) has followed the general least square regression of strong motion data to determine the S or Lg wave attenuation for the

La Paz–Los Cabo region, Baja California, Mexico. The obtained results were further validated, using the coda normalization method and reported a lower attenuation for the La Paz–Los Cabo inland region. Later, Ortega and Quintanar (2011) used the offshore earthquake data and compared the propagation characteristics of S waves reported by Ortega and González (2007) with the P wave propagation characteristics following the same method. Vidales-Basurto *et al.,* (2014) has conducted the attenuation study in the south central GoC region to understand the tectonic structure of gulf region. The results obtained based on the different source receiver distance depicts the higher body wave attenuation along the oceanic spreading centres. Also, high attenuation is observed towards the southern gulf region compared to the central gulf region. Later, Rodríguez- Lozoya *et al.,* (2017) estimated the coda attenuation for central gulf region and observed a similar higher attenuation for the southern sub region. Also, Castro *et al.,* (2017b) determined the body wave attenuation and source functions for the gulf region using the foreshocks, aftershocks and the main shock (Mw= 6.6) of event occurred on October 19, 2013, along the Farallon fault region. For central gulf region, Quintanar *et al.,* (2019) have analysed the foreshocks, main shock (Mw=6.6) and aftershocks of January 4, 2006 San Pedro Martir earthquakes. They obtained the source parameters, fault geometry and fault slip distribution for the earthquake and later used them to study the attenuation behaviour of gulf region. More, recently Castro *et al.,* (2019) studied the one-dimensional variability of Q_s in the southern region of GoC at selected frequencies. They reported an increase of Q_s with increase of frequency but small variation of Q_s has been observed with depth (5-40 km) at individual frequencies.

The present article uses the approach given by Joshi *et al.,* (2010) to obtain three- dimensional attenuation structure in a broad frequency range. We use data from 25 earthquakes recorded both onshore and offshore by Ocean Bottom Seismographs (OBS) deployed in the study area of south-central Gulf of California (GoC) region. This tectonically complex region comprises a system of short spreading centres and transform faults and is considered as a high seismicity zone (Sumy *et al.,* 2013). The attenuation structure must have a strong correlation with the tectonic environment and the seismic wave velocity (Lizarralde *et al.,* 2007; Luccio *et al.,* 2014) and for this reason, is important to evaluate the attenuation characteristics of GoC.

TECTONIC STRUCTURE OF STUDY AREA

The Gulf of California (GoC) is relatively young, oblique rift system that formed with the cessation of the Farallon plate subduction under the North American plate about 12 million year ago (Lonsdale, 1989). The evolution of the GoC extensional province occurred in two stages; stage-I: extension and separation of the continents that resulting in the formation of marine basins; stage-II: is being continued till today is the expansion of seafloor and structure of transform faults (Stocks and Hodges 1989; Bennett *et al.*, 2007; Vidales-Basurto *et al.*, 2014). The GoC is comprised a group of stepping faults, seafloor spreading, ridges and the right lateral strike-slip transform faults which collectively form a continental rift system. Consequently, it facilitates the Pacific Plate to move apart from the North American plate. However, an anomalous left lateral strike slip faulting has been observed for September 1, 2007 main shock (Mw= 6.1) and its subsequent aftershocks activities in the southern gulf region (Ortega & Quintanar, 2010). The unusual characteristics of main shock and the high rate of aftershock (more than 800 during a period from September to December 2007) activities for a transform fault is believed to be a combination of narrow bathymetry, growing seafloor and stress interaction along the continental oceanic transition (COT) boundary. The major tectonic faults and the corresponding oceanic basins in GoC is shown in Fig 1. The crust underneath the ocean basins in GoC differs in terms of thickness, rifting style, sea floor spreading, and magmatism.

The south central GoC has a distinct rifting style compare to the surrounding region. Lizarralde *et al.*, (2007) has observed that evolution of rifting in this region is primarily controlled by the magmatic depletion of mantle. The anomalous Guaymas basin in the central region is considered as magmatic since the beginning of breakup (~ 6 m.a.) and possess the largest new igneous crust spread over ~280 km. The intrusive magmatism in the overlain sediments has resulted in the formation of sills over a large distance from the spreading centre (Aragón-Arreola *et al.*, 2005). On the other hand, the Farallon and Pescadero segment in the south of Guyamas basin have narrow ocean basins with nascent or no sea floor spreading (Lizarralde *et al.*, 2007).

DATA USED

The highly active south-central GoC was monitored by regional seismic network of NARS- Baja (Network of Autonomously Recording Seismographs) and the Broadband Network (RESBAN) operated by the CICESE (Avila-Barrientos and Castro, 2016). The present study also used some of the events recorded offshore by eight Ocean bottom Seismographs (OBS's) deployed under the Sea of Cortez Ocean Bottom Array (SCOOBA) experiment in the Guaymas and Alarcon basins (Sumy *et al.,* 2013). This offshore network was operative only from October 2005 to October 2006. For the present study, 25 earthquakes recorded on both onshore and offshore stations deployed in the GoC were used. The offshore OBS's are equipped with four components (two horizontal, one vertical and one pressure component) to record the ground motion at the recording rate of 32.25 samples/s (Sumy *et al.,* 2013). The onshore broadband system, operated by CICESE, is equipped with three-component sensors, recording at 20 samples/s (Castro *et al.,* 2017b, 2018). The recording stations and the epicentral location of the earthquakes used in this study are shown in Fig. 1. The calculated hypocentral parameters of the selected earthquakes and the stations used are listed in Table 1.

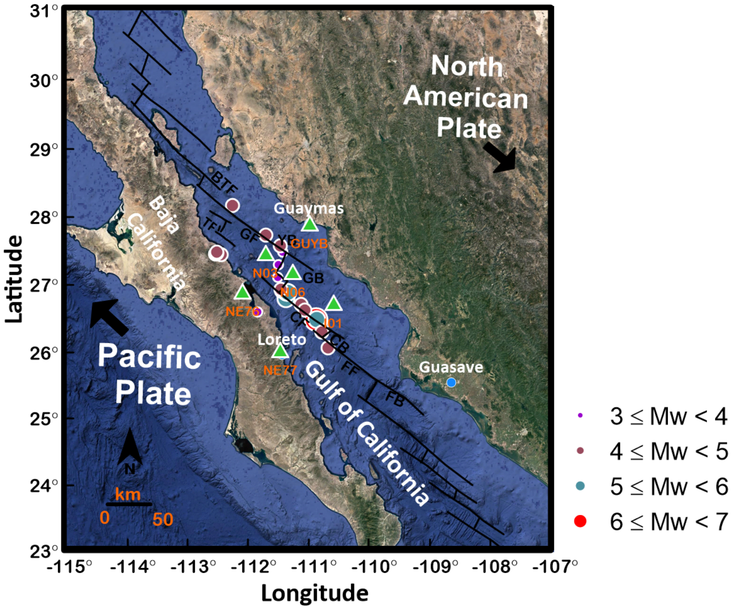

Figure 1. Map showing the location of recording stations (green triangles) and epicentres (circles) of the earthquakes selected. The purple, brown, sea green and the red circle are different magnitude bins and has been scaled as per the magnitude of earthquakes. The location of faults is taken from Aragon-Arreola *et al.,* (2005) and Dorsey *et al.,* (2013). DB= Delfin Basin, BTF= Canal de Ballenas Transform Fault, YB= Yaqui Basin, GF= Guaymas fault, GB= Guaymas Basin, CF= Carmen Fault, CB= Carmen Basin, FF= Farallon Fault, FB= Farallon basin, TF= *Tortuga Fault*. The black arrows represent the plate motion.

Fourier amplitude spectra of S-wave windows from 98 records have been used as an input in the inversion. The spectral input files consist of 18 discrete values of S-wave spectral amplitudes that range from 0.16 Hz to 7.94 Hz. Fig. 2 shows a sample of the amplitude spectra of a few stations along with the epicentral distance (ED). The earthquakes selected were relocated by Castro *et al.*, (2011) using records from the regional stations of the NARS-Baja (Trampert *et al.,* 2013) and RESBAN (Castro *et al.,* 2018b) arrays. Some of the events were located by Sumy *et al.*, (2013) using OBS's. Fig. 3 represents the magnitude hypocentral distance plot for selected events. The records were corrected for instrument response and they were baseline corrected. The S-wave windows length used to calculate the fourier amplitudes amplitudes varies between 2 s for local hypecentral distance to 75 s for regional distance. The time window starts a few seconds before the first *S*-wave arrival and ends before the surface waves arrive. The spectral records were smoothed choosing 20 equidistant frequencies, between 0.16 and 7.94 Hz, on a logarithmic scale and averaging the amplitudes using a variable frequency band of ± 25% over the central frequencies chosen (Castro *et al.,* 2017a).

The site response functions determined by Vidales-Basurto *et al.,* (2014) and Avila-Barrientos and Castro (2016) for both the NARS-Baja and the RESBAN broadband stations were used to correct the spectral amplitudes for site effects.

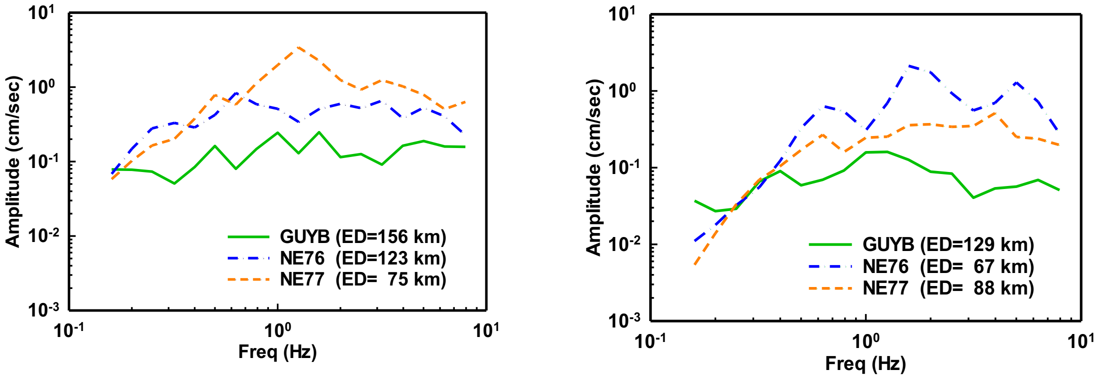

(a)

(b)

Figure 2. Amplitude spectra of S-phase recorded at stations GUYB, NE76 and NE77 from the following earthquakes: (a) 12/03/2003 (M_w=6.3) (b) 30/07/2006 (M_w=5.9)

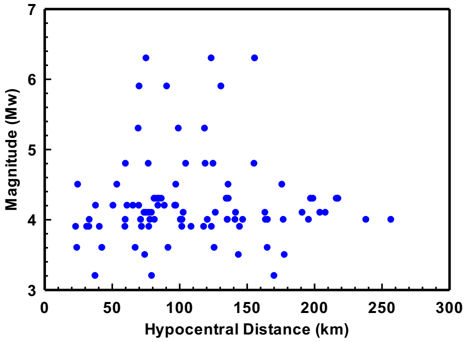

Figure 3. Spatial distribution of magnitude versus hypocentral distance of analyzed earthquakes. The selected earthquakes have Mw ranging from 3.2 to 6.3 with hypocentral distance from 20 km to 260 km.

A rectangular block of dimension 230 km to 288 km was selected on the basis of coverage area of seismic network and availability of events within it. This block is divided into six sub-blocks with individual sub-block having a rectangular area 38 km x 48 km. These blocks are further extended by three blocks of thickness upto a depth of 12 km; thereby dividing entire area into individual three dimensional blocks of size 38 km x 48 km x 4 km. The location of the rectangular block is shown in Fig. 4 along with the structural features of the study region. Inset zoom in the Fig. 4 represents the straight-line ray path projection in sub blocks between the events and the recording stations. The spectral amplitudes shown in Fig. 2 are from earthquake located between the first and third row of considered rectangular block.

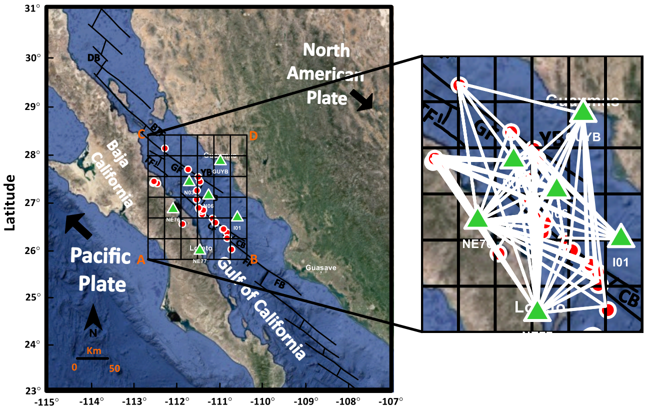

Figure 4. Map with location of the study area and the rectangular grid (ABCD) of the volume sampled, along with the tectonic features in the rectangular grid (ABCD). Red circles with white boundary indicate the epicentres of selected earthquakes. Inset zoom shows the projection of ray paths between the selected events and the recording stations in the studied area.

Table 1. Parameters of earthquake used in the present work.

S. No.	Year	Month	Day	Hour	Minute	Second	Latitude°	Longitude°	Depth (km)	Magnitude (Mw)	Recording Stations
1	2002	12	6	6	24	12.256	26.3152	-110.7364	8.6	4.0	GUYB, NE76, NE77
2	2002	12	7	1	33	45.285	26.0794	-110.633	9.8	4.1	GUYB, NE76, NE77
3	2002	12	8	17	45	17.391	26.3141	-110.7159	16.2	3.5	GUYB, NE76, NE77
4	2003	1	19	16	46	30.147	26.9204	-111.3973	2.0	4.0	GUYB, NE76, NE77
5	2003	3	12	23	41	30.561	26.4994	-110.8355	2.0	6.3	GUYB, NE76, NE77
6	2003	3	13	4	23	7.463	26.4337	-110.7387	8.3	4.0	GUYB, NE76, NE77
7	2003	3	13	14	38	20.61	26.6403	-111.0145	15.6	4.1	GUYB, NE76, NE77
8	2003	3	22	17	55	41.519	26.5048	-110.8193	5.3	4.8	GUYB, NE76, NE77
9	2004	2	18	19	30	39.033	26.6345	-111.0169	7.2	3.9	NE76, NE77
10	2004	8	7	10	41	24.442	26.6103	-111.7947	6.2	3.2	GUYB, NE76, NE77
11	2006	4	20	3	40	41.28	28.194	-112.21	3.0	4.0	GUYB, I01, N03, NE76, NE77
12	2006	4	23	7	50	40.05	27.498	-111.38	4.0	3.6	GUYB, I01, N03, N06, NE76, NE77
13	2006	5	11	5	58	18.04	27.311	-111.45	1.0	3.9	I01, N03, N06, NE76, NE77
14	2006	5	28	14	0	56.78	26.948	-111.41	12.0	4.8	GUYB, NE76, NE77
15	2006	5	28	14	18	2.23	26.904	-111.3	4.0	5.3	GUYB, NE76, NE77
16	2006	6	11	4	11	36.33	26.726	-111.08	5.0	4.2	I01, N03, N06, NE77
17	2006	6	16	8	46	44.74	27.595	-111.42	2.0	4.5	I01, N03, N06, NE76, NE77
18	2006	7	30	1	20	56.96	26.809	-111.326	19.4	5.9	GUYB, NE76, NE77
19	2006	8	7	2	50	53.05	27.503	-112.47	6.0	4.3	I01, N03, N06, NE76, NE77
20	2006	8	8	4	29	32.29	27.472	-112.49	5.0	4.3	I01, N03, N06, NE76, NE77
21	2006	8	8	21	36	35.8	27.461	-112.39	10.0	4.1	I01, N03, N06, NE76, NE77
22	2006	8	9	23	32	19.38	27.485	-112.47	5.0	4.3	I01, N03, N06, NE76, NE77
23	2006	8	11	17	55	11.5	26.881	-111.34	5.0	4.2	I01, N03, N06, NE76, NE77
24	2006	9	12	18	56	28.36	27.753	-111.66	2.0	4.0	I01, N03, N06, NE76, NE77
25	2006	9	25	13	4	5.65	27.122	-111.46	5.0	3.9	I01, N03, N06, NE76, NE77

METHODOLOGY

The inversion procedure used is based on the method proposed by Aki and Lee (1976). A cartesian co-ordinate system has been used to represent the distribution of the shear wave attenuation coefficient of the study region. The region was divided into 108 rectangular blocks with each block having a different $Q_s(f)$ value. The corners of these rectangular blocks on the surface of the Earth are assumed as the observation points. For an earth model having several blocks with different shear wave attenuation coefficient values, $Q_s(f)$ for a given frequency f, the spectral acceleration A(f) can be given by the following relation (Hashida and Shimazaki 1984):

$$\mathrm{A(f) = S(f).G.g_a.\exp} \sum_r (\mathrm{C_{pqr}.T_{ijr}}) \ldots\ldots\ldots\ldots\ldots (1)$$

$$\mathrm{G} = \frac{1}{\mathrm{R}}$$

$$\mathrm{C_{pqr}} = -\pi \mathrm{f}/\mathrm{Q}_{pqr}(\mathrm{f})$$

Where S(f) denotes the source acceleration at frequency f, G represents the geometrical spreading function and R the hypocentral distance, g_a is site amplification term and $\mathrm{T_{ijr}}$ represents the travel time of the ray in rth block having attenuation coefficient $\mathrm{C_{pqr}}$. The parameter $\mathrm{Q_r(f)}$ represents the frequency dependent quality factor in the rth rectangular block. The subscript i, j represents the ith station and the jth event, respectively. To solve equation (1), an initial three dimensional $\mathrm{Q_{pqr,o}(f)}$ model of earth is assumed. The subscripts p, q is used to define the blocks along the two-horizontal directions of the rectangular area as shown in Fig. 5. The subscript r identifies the rectangular blocks in the downward direction. The initial input model is based on the velocity and *Qs* models (Rebollar *et al.,* 2001 and Paulseen and de Vos (2017)) available for the studied region. The initial guess of source strength $S^{cal}(\mathrm{f})$ for inversion has been calculated using initially assumed *Q* model and recorded spectral acceleration in the following relation:

$$\mathrm{S_{ij}^{cal}(f)} = \frac{\mathrm{A}_{pq}^{inter}(\mathrm{f})}{G.g_a.\exp \sum_r (C_{pqr,o}.T_{ijr})} \ldots\ldots\ldots\ldots\ldots\ldots\ldots\ldots\ldots\ldots\ldots\ldots (2)$$

Where $\mathrm{S_{ij}^{cal}(f)}$ defines the calculated source strength at frequency f, $\mathrm{A_{pq}^{\mathit{inter}}(f)}$ is spectral acceleration obtained after interpolation at each observation points at frequency f and $\mathrm{C_{pqr,o}}$ is initially assumed attenuation in rth block. This value of spectral acceleration is calculated from the earthquake records. Because it is nearly impossible to have a network in which the observation points are placed at each corner of the grid at equal spacing, we are required to calculate contours of spectral acceleration in the considered rectangular area. The amplitude spectrum of S-phase of a particular earthquake, recorded at different station is used to prepare the spectral acceleration contours at frequency, f, using kriging interpolation. The spectral acceleration $\mathrm{A}_{pq}^{inter}(\mathrm{f})$ values obtained at different observation points from the contours has been used in the equation (2) to obtain the initial source strength $\mathrm{S_{ij}^{cal}(f)}$ at frequency f. In the present study the input data used for inversion has been corrected for site effects, therefore the site amplification factor g_a is fixed to one. The average value of source strength $\mathrm{S_{ij}^{cal}(f)}$ calculated at different frequencies is further used to calculate the spectral acceleration $\mathrm{A_{ij}^{cal}(f)}$ using equation (1).

If the observed spectral acceleration at any point is defined as $\mathrm{A_{ij}^{obs}(f)}$, then the relation between

$A_{ij}^{obs}(f)$, the actual attenuation coefficient C_{pqr} and source strength $S_o(f)$ can be calculated using same equation (1). By dividing observed $A_{ij}^{obs}(f)$ and calculated $A_{ij}^{cal}(f)$ spectral acceleration, following equation is obtained:

$$A_{ij}^{obs}(f)/A_{ij}^{cal}(f) = (S_o(f)/S^{cal}(f)).\exp \sum_r (C_{pqr,o} - C_{pqr}).T_{ijr}) \text{ …………….. } (3)$$

Natural logarithms on both the sides of above equation gives the following equation:

$$\ln (A_{ij}^{obs}(f)/A_{ij}^{cal}(f)) = \ln ((S_o(f)/S^{cal}(f))) + \sum_r (\delta C_{pqr}).T_{ijr}) + e \text{ ……….. } (4)$$

Where $\delta C_{pqr} = C_{pqr,o} - C_{pqr}$

$$\mathrm{Res}_{ij}(f) = \ln (A_{ij}^{obs}(f)/A_{ij}^{cal}(f))$$

“$\mathrm{Res}_{ij}(f)$" represents the residual acceleration and is used as a known variable for the inversion process. The term e stands for error in calculation.

The parameters δC_{pqr} and T_{ijr} on the right-hand side of equation (4) can be calculated from the initial velocity model using ray theory. For a particular earthquake, the total number of equations corresponds to the number of observation points. In equation (4), $A_{ij}^{obs}(f)$ and $A_{ij}^{cal}(f)$ represents the observed and calculated spectral acceleration, and $S_o(f)$ and $S^{cal}(f)$ are observed and calculated source strength, respectively. Equation (4) is inverted to get C_{pqr} in each block and the ratio of observed and calculated source strength. In the inversion scheme, we incorporate a new iteration by substituting the value of source strength obtained from the first inversion.

The process of obtaining spectral acceleration at each point in the grid is obtained directly from an inbuilt subroutine that calculates contour values at different positions using the spectral data of S phase from each record analysed. Fourier amplitude spectra of 98 records has been used to obtain 18 three dimensional structures in the discrete frequency range from 0.16 Hz to 7.94 Hz.

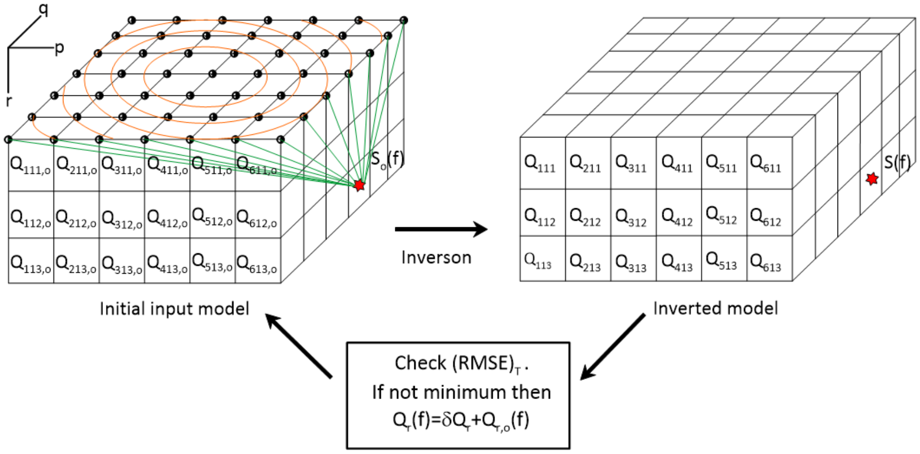

Figure 5. Schematic representation of inversion of initial $Q_{pqr,o}$ model used to obtain the final Q_{pqr} model for different rectangular blocks. The orange circles represent the spectral acceleration contours at frequency f and is used to obtain the calculated spectral acceleration $A_{ij}^{cal}(f)$. Red star and half black circles symbolize the theoretical position of earthquake and the observation points, respectively. Green lines depict the theoretical straight line ray path from source to the observation points through the different Q_{pqr} model blocks in time T_{ij}^{pqr}.

TESTS FOR INPUT PARAMETER

The results of the inversion depend on the quality of input data (e.g. Joshi 2007). In the present work, the input data consists of the initial velocity model, the initial shear wave attenuation model, hypocenters distances and distribution of the selected events and the S- wave window chosen to calculate the spectral acceleration values. To test the sensitivity of these parameters, various input parameter tests were performed, like the effect of the velocity model and the resolution of the final attenuation model on the input parameters.

Bakus and Gilbert (1968) have used the resolution matrix to check the suitability of model matrix, which can be defined for the damped least-square inversion using the following relation:

$$\mathrm{R} = (\mathrm{G}^{\mathrm{T}}\mathrm{G} + \lambda \mathrm{I})^{-1}\mathrm{G}^{\mathrm{T}}\mathrm{G} \;\ldots\ldots\ldots\ldots\ldots\ldots\ldots\ldots\ldots.. \quad (5)$$

Where R represents the resolution matrix and when R equals to the unit matrix, the obtained solution is unique. As the resolution matrix deviates from the unit matrix, the resolution becomes poorer. Several attempts had been made to check the resolution matrix for simple cases, and the obtained results are close to identity matrix for damped least-square inversion method. This simple case is also used for testing the reliability of the developed algorithm for inversion. For the actual case of acceleration data, the final model is selected based on the minimization of root mean square errors (RMSE). The $RMSE_A$ between the observed and calculated spectral acceleration at a particular frequency is given by the following equation:

$$\mathrm{RMSE_A} = [\tfrac{1}{\mathrm{N}}\textstyle\sum_{\mathrm{i=1}}^{\mathrm{N}}(\,\mathrm{A_i^{obs}} - \mathrm{A_i^{cal}})^2]^{1/2} \;\ldots\ldots\ldots\ldots\ldots\ldots\ldots \quad (6)$$

Where $\mathrm{A_i^{cal}}$ and $\mathrm{A_i^{obs}}$ denote the calculated and the observed spectral acceleration values at N number of observation points. The RMSE between the observed and calculated data and model matrix can also be computed using the equation (6). A reliable solution is obtained when all the errors are minimized simultaneously. The final model is selected based on the minimization of the following equation:

$$(\mathrm{RMSE})_{\mathrm{T}} = (\mathrm{Nor(RMSE)_{dat}} + \mathrm{Nor(RMSE)_{mod}} + \mathrm{Nor(RMSE)_A})/3 \;\ldots\ldots\ldots\ldots\ldots \quad (7)$$

Where $\mathrm{Nor(RMSE)_{dat}}$ and $\mathrm{Nor(RMSE)_{mod}}$ represents the normalized RMSE due to data and model matrix. However, it is hard to minimize $\mathrm{(RMSE)_{dat}}$, $\mathrm{(RMSE)_A}$ and $\mathrm{(RMSE)_{mod}}$ simultaneously for the same iteration, that is $\mathrm{(RMSE)_T}$ always differs from the ideal value equal of one. Moreover, the choice of the initial model and the number of input events also plays a vital role to obtain the final solution.

TEST FOR VELOCITY MODEL

Results of inversion depend upon the appropriate velocity models used for the parameterization of earth's structure as the properties mainly change with depth due to compaction, sedimentation and thermal changes. A numerical experiment was performed to check the distribution of shear wave velocity (*Vs*) model and quality factor (*Qs*) value for one layer, two layers and three layers model. The initial velocity model with different *Qs* values is shown in Table 2. The input models are based on the velocity and *Qs* models used by Rebollar *et al.,* (2001) and Paulseen and de Vos (2017) for the Gulf and Baja California region. The final model selection is based on the minimization of $\mathrm{(RMSE)_T}$. In the present work, error reduces from 252 x 10^{-4} to 134 x 10^{-4} when model changes from homogeneous to three layer model. Table 3 shows error estimates for homogeneous and layered earth models. Fig. 6 shows the dependency of the final attenuation structure on the initial velocity model and their corresponding error estimates. The three models predict a local high *Qs* zone but is located more accurately for two and the three-layer models. The 3-layer model provides more details of the *Qs* structure and fits the data better.

Table 2. Initial homogeneous layer, two layer and three layer earth models.

	Three layer model		Two layer model		One layer model	
Depth (km)	Velocity (km/s)	Qs	Velocity (km/s)	Qs	Velocity (km/s)	Qs
0-4	2.83	40	2.83	20	3.27	50
4-8	3.18	50	3.49	65	3.27	50
8-12	3.80	90	3.49	65	3.27	50

Table 3. Estimate of $(RMSE)_T$ and its iteration for homogeneous layer, two layer and three layer earth model.

Initial earth model	Minimum $(RMSE)_T$ (10^{-4})	Number of iterations corresponding to final model
Homogeneous layer	252	2
Two layer	179	3
Three layer	134	3

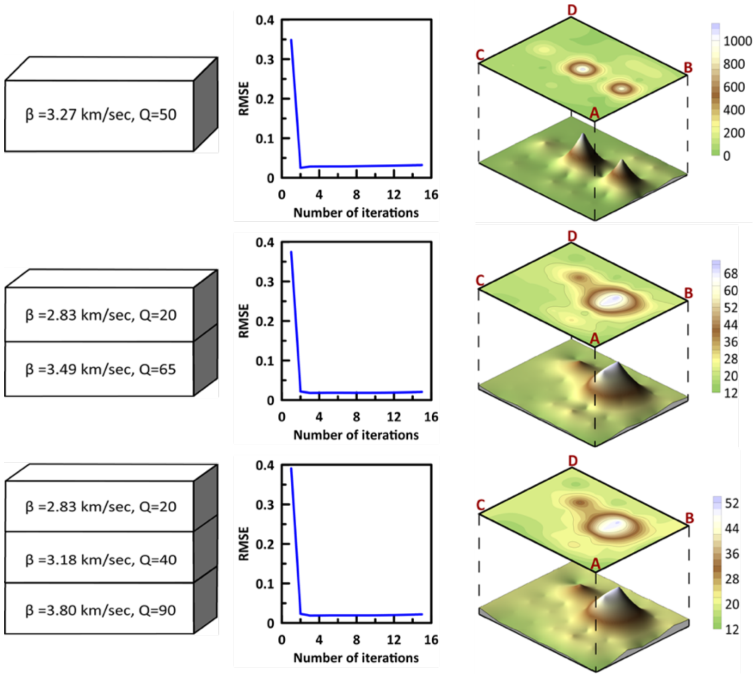

(a) (b) (c)

Figure. 6. Dependency of final attenuation structure on the initial velocity models with different Q values. (a) represents the initial layer model, (b) the error corresponding to input layer model and (c) the surface layer (0-4 km) attenuation structure contours along with the 3D projection of contour values at 1 Hz frequency.

TEST FOR INPUT DATASETS

In this experiment, the behaviour of the number of input earthquake data on final attenuation structure has been studied by removing some input earthquakes sequentially. The final attenuation model obtained using the data set of ten, fifteen and twenty-five earthquakes are shown in Fig. 7. This figure shows horizontal projections of the *Q* estimates obtained at different depths (0-4 km, 4-8 km and 8-12 km). Since the three data sets used for this test sample different crustal volumes, the resulting *Q* contours are significantly different. It is clear that the greater the number of sources used the better is the fit and the convergence. Table 4 shows error estimate and the number of iterations corresponding to the final solution for ten, fifteen and twenty-five earthquakes data sets, respectively. It is observed from the inversion that the $(\mathrm{RMSE})_T$ decreases with increase in input earthquake data and attenuation structure become much visible compared to that obtained using fewer earthquakes.

Table 4: Estimate of $(\mathrm{RMSE})_T$ and its iteration with the number of input earthquake data.

Input number of earthquakes	$(\mathrm{RMSE})_T$ (10^{-6})	Number of iterations
10	442	9
15	560	3
25	348	3

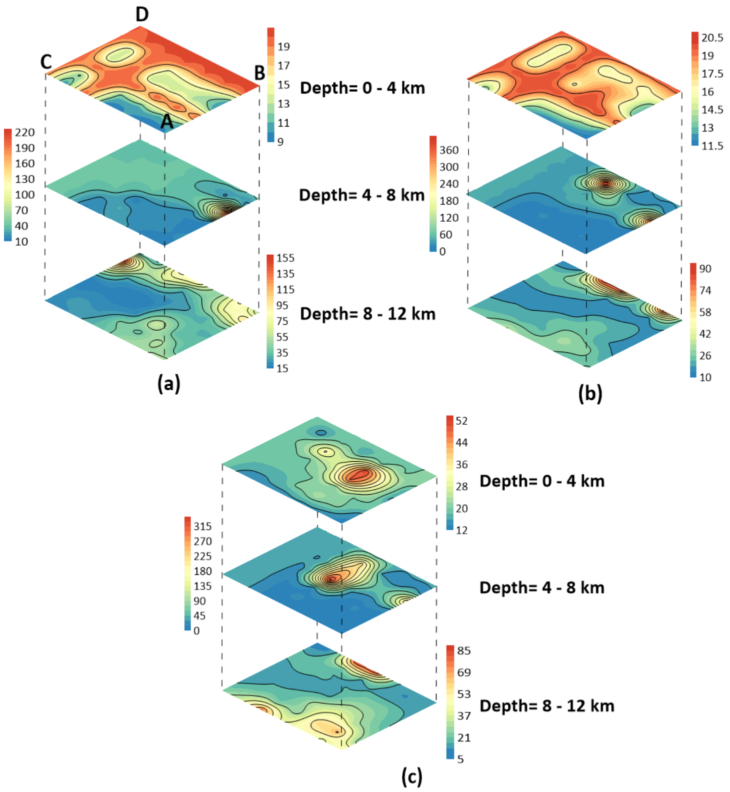

Figure 7. Dependency of the final attenuation model on the number of input earthquake data. Final models obtained for input data set of (a) Ten (b) Fifteen and (c) Twenty-Five earthquakes.

RESULTS AND DISCUSSION

The geologically young and tectonically complex region of the GoC provides an opportunity to understand the attenuation characteristics of the crust in this region. We have determined a three-dimensional (3-D) attenuation structures for the south - central GoC region. The area of interest has been divided into the 108, 3-D rectangular blocks of dimensions 38 km x 48 km x 4 km. The selection of dimensions of the rectangular blocks is based on the location of recording stations and earthquake epicentres. All stations and hypocenters of earthquakes lie within these rectangular blocks.

In the present article, the three - dimensional attenuation structure has been determined from a total of 1944 estimates of the shear- wave quality factor at 18 discrete frequencies. The resolution matrix of the inversion has significant importance in understanding how much information has been recovered in individual blocks. Fig. 8 is a 2-D view of the resolution matrix for the individual blocks. Blocks with resolution value > 0.7 have been considered as well resolved, and it has been observed that almost all the blocks in the region sampled are in general well resolved. Fig. 9 displays the source-station ray paths and illustrates the coverage of the volume sampled, which is good at depths above 10 km.

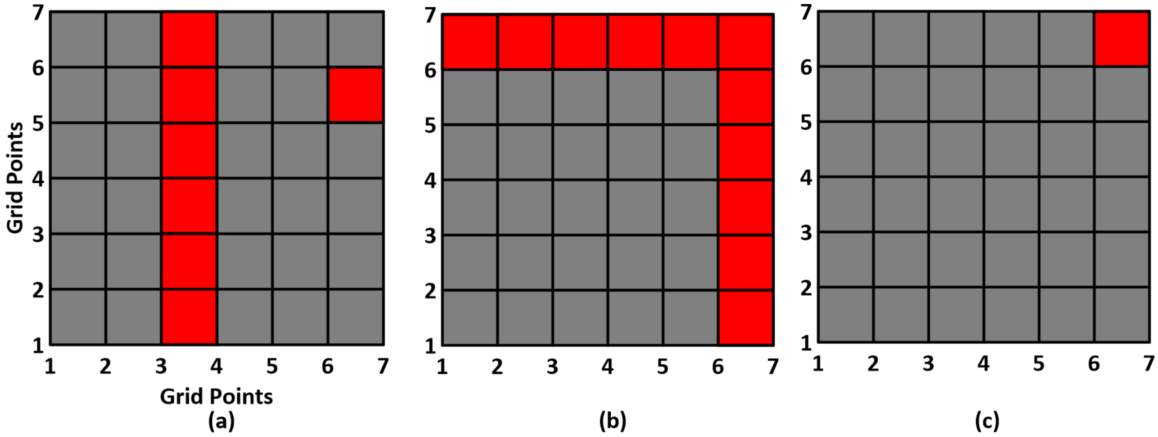

Figure 8. Block diagram representing the resolution matrix values obtained in individual blocks from the inversion at (a) 0 – 4 km depth, (b) 4 – 8 km depth and (c) 8 -12 km depth, respectively. Grey color blocks are well resolved (resolution value > 0.7) while the red blocks are poorly resolved (resolution value < 0.7).

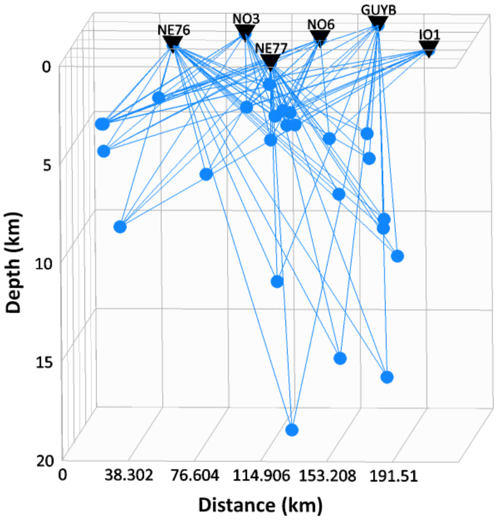

Figure 10. Ray-path diagram illustrating the coverage of different blocks between the events and their respective recording stations. The events are represented by the blue dots and the station shown by the inverted black triangles.

The inversion algorithm gives three-dimensional attenuation structure at 18 different frequencies at which spectral input data has been used. The three-dimensional attenuation structure at 0.5 Hz, 1.0 Hz and 2.0 Hz, respectively, are shown in Fig. 10, 11 and 12. The blocks with low-resolution values have been covered with white blocks.

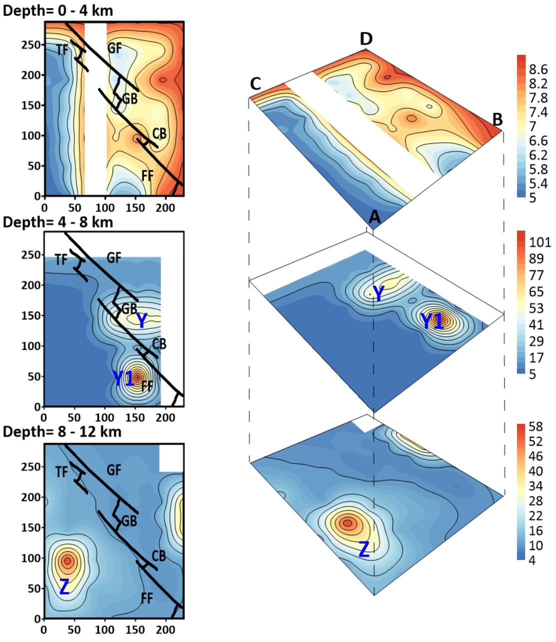

(a) (b)

Figure 10. Quality factor contours obtained from the inversion at 0.5 Hz frequency for (i) 0-4 km (ii) 4-8 km (iii) 8-12 km depths. The solid line in (a) represents the tectonic features present in the study region. Labels Y, Y1 and Z represent the high *Q* patches observed at various depths. Blocks of lower resolution are covered by the white rectangular blocks.

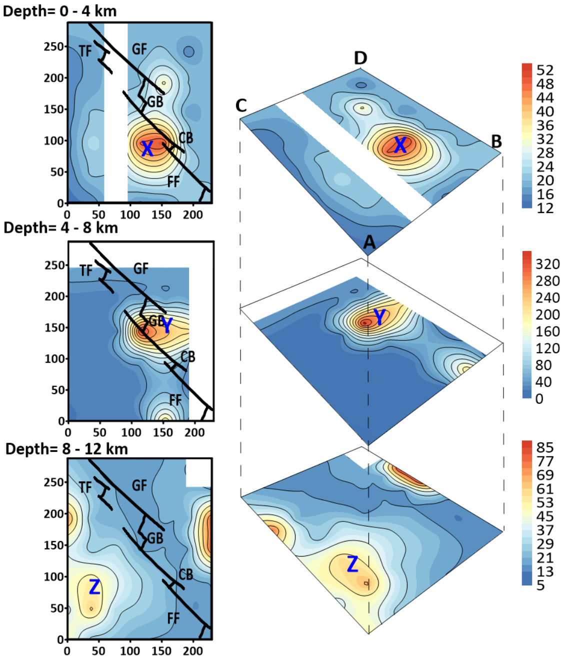

(a) (b)

Figure 11. Quality factor contours as in Fig. 9 but at 1.0 Hz for (i) 0-4 km (ii) 4-8 km (iii) 8-12 km depths. The solid black line in Fig. (a) represents the tectonic features present in the study region. Labels X, Y and Z points out high *Q* patches observed at various depths. Blocks of lower resolution are covered by the white rectangular blocks.

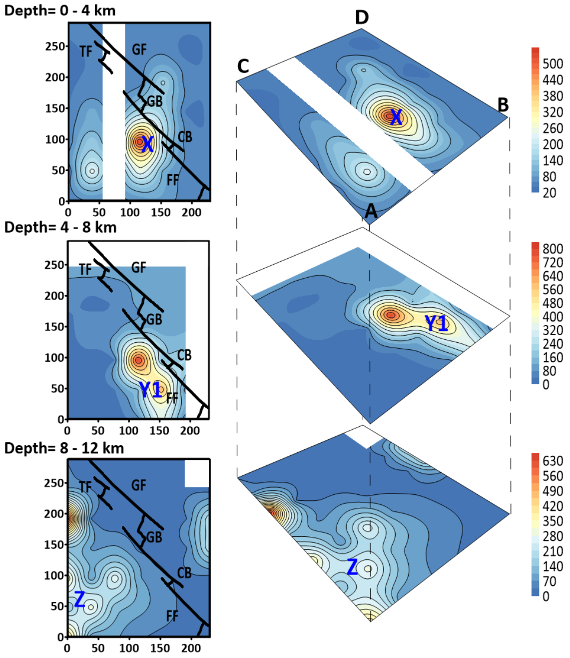

(a) (b)

Figure 12. Quality factor contours at 2.0 Hz for (i) 0-4 km (ii) 4-8 km (iii) 8-12 km depths. The solid line in (a) represents the tectonic features present in the study region. Labels X, Y1 and Z points out the high Q patches observed in the studied region at various depths. Blocks of lower resolution are covered by the white rectangular blocks.

The attenuation contours obtained from the inversion are useful for identifying the different patches of low and high Q values at different depth layers. The results obtained shows low Q values along the gulf region, particularly at shallow depths. The attenuation structure obtained is correlated with the crustal velocity structure determined by Lizarralde *et al.,* (2007) and Teske *et al.,* (2014). Fig. 13 summarizes the crustal structure of the Guaymas basin, located in the centre of the studied region of the gulf.

For the surface layer (0-4 km), the low Q values contrast with one major patch (zone X in figures 11 and 12) of high Q value in the south-east zone of the region. The crustal structure obtained by Aragón-Arreola *et al.,* (2005), Lizarralde *et al.,* (2007) indicates that the south-central region of GoC, is masked by a thick layer of sill intruding the sediments deposited on the igneous layer. Thus, resulting in the low Q value and high attenuation in the surface layer. But the thickness of this sediment layer decrease from ~ 3 km in the Guyamas basin to the ~1.5 km in the Carmen basin. Thus, the presence of the igneous layer (Teske *et al.,* (2014)) in the surface layer results in the increase of Q (zone X) in the south-east of the studied region, as shown in Figs. 11-12 at 1.0 Hz and 2.0 Hz. This feature does not show at the lower frequency (0.5 Hz) probably due to the small dimension of the high Q patch.

In the middle layer (4-8 km depth), two major patches (zones Y and Y1) of high Q value can be observed close to the ridge- transform system. First, the high Q patch Y at 0.5 and 1.0 Hz along the Guyamas basin increases with frequency from 53 at 0.5 Hz to 320 and 800 at 1.0 and 2.0 Hz, respectively. The subsurface representation of Guaymas basin shown in Fig. 13 suggest the presence of high heat flow due to intruded sills located along the western side of the spreading ridge. Thus, the cooler southwestern side has a higher Q value compared to the hotter northeastern side of the Guaymas Basin. The other high Q patch Y1 located along the Farallon Transform fault in a zone of high seismicity, where the rocks must be cool and rigid.

In the bottom Layer (8-12 km depth), a high Q value patch (Z) is observed along with the older and cooler continental crust. The obtained Q values in the depth range show a decreasing trend of *Q* towards the spreading ridges. This 8-12 km depth zone probably has a high flow of magma from the mantle near the ridge, as shown in Fig. 13, resulting in an increase of thermal flow in the bottom layer. Thus, low *Q* values and high *S*-wave attenuation takes place along the ridge transform fault system.

The obtained attenuation contours correlate with the crustal model proposed by Lizarralde *et al.,* (2007) and Teske *et al.,* (2014) and support the high attenuation of seismic energy observed along the gulf region. Also, the decrease in seismic velocity and high heat flow beneath the thin crust correlates with the high attenuation observed along the young plate boundary (Persaud *et al.,* 2014; Teske *et al.,* 2014; Vidales-Basurto *et al.,* 2014; Lizarralde *et al.,* 2007; Hasegawa 1985). These results also indicate that the seismic attenuation is decreasing towards the continental crust.

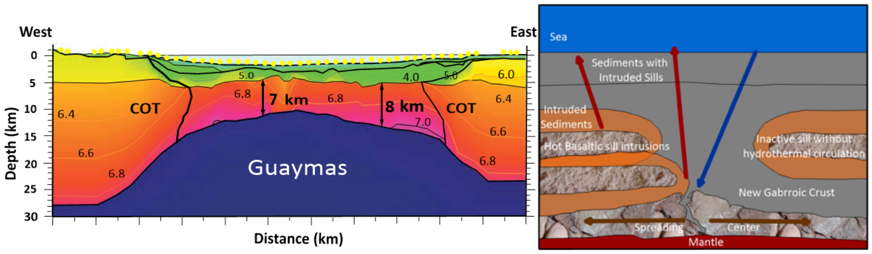

(a) (b)

Figure 13. (a) Seismic velocity and crustal model for Guaymas extensional basin region of GoC, Mexico (modified after Lizarralde *et al.,* 2007). (b) schematic diagram of subsurface basement, sills, sediments and arrow represent the liquid flow direction (modified after Teske *et al.,* 2014).

BOOTSTRAP TEST

In order to inspect the stability of inverted *Q* structures, the bootstrap resampling scheme has been adopted. For the same, the initial population of 25 earthquakes has been divided into two subsets, with each subset having randomly selected 17 earthquakes. The inversion results for 1.0 Hz frequency are shown in Fig 14.

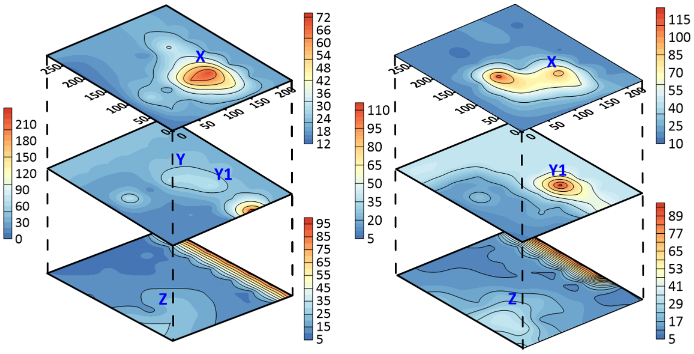

(a) (b)

Figure 14. Bootstrap test results for two different subsets of initial population of earthquakes for depths (i) 0-4 km (ii) 4-8 km and (iii) 8 -12 km at 1 Hz frequency. The alphabets X, Y, Y1 and Z represents the identified low attenuation zones in different depth layers.

The comparison of bootstrap test results with Figs. 10-12, clearly reveal that for different subset of initial population of earthquakes, we are capable of detecting the same attenuation features on different depth layers. Thus, the resulted *Q* structure in this study is stable and consistent for different subset of original dataset. However, decreasing the number of earthquakes in bootstrap test has lowered the resolution of individual rectangular blocks, so few major differences in the attenuation structure has been observed in the bootstrap results.

A regional *Q*-frequency relation for this region has been prepared by using all 1944 estimates of shear wave quality factor at 18 different frequencies. Fig. 15 and 16 show the *Q*-frequency relation obtained using average values of Q_s resulting from the inversion for each frequency. The best least square fit gives the relation $Q_s(f)= 20f^{1.2}$ for this region. Fig. 15 shows data used for obtaining this relationship. It has been observed that seismic *Q* strongly depends on the frequency *f* in the view of relation $Q = Q_0 f^n$ and increases with increase of frequency (Aki, 1980a). But this increase is not so widespread at low frequencies in comparison to high frequencies as we move from surface to depth (Kumar *et al.,* 2015). Therefore, a relatively large error has been measured at high frequencies as shown in Fig. 15. Despite the large variation in Q_s values at high frequencies, the resulted Q_s values are providing the significant information for south-central GoC region.

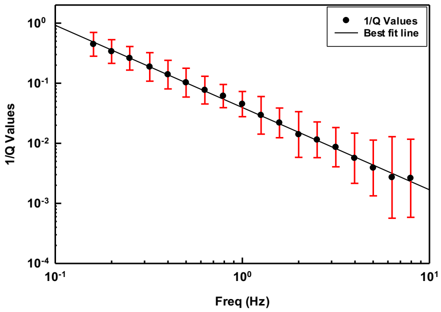

Figure 15. Frequency - dependent shear wave quality factor *1/Qs(f)* relationship obtained from 1944 values of shear wave quality factor at different frequencies.

The Q_0-f^n relation can be used to distinguish different regions into seismically active and stable areas. The parameters Q_0 and *n* represent heterogeneities and levels of tectonic activity, respectively (Kumar *et al.,* 2015). Low values of $Q_0 < 200$ indicate tectonically and seismically active regions, high values of $Q_0 > 600$ signify seismically stable regions, and intermediate values are expected in moderately active regions (Kumar *et al.,* 2005). A correlation between the degree of frequency dependence and the level of tectonic activity in the area of measurement have been made by several researchers for a number of tectonic regions (e.g., Aki, 1980a; & Van Eck, 1988). They ascertained higher *n* values for tectonically active regions as compared to that of tectonically stable regions (Sharma *et al.,* 2015). The obtained low $Q_0 =20$ and high exponent $n=1.2$ of this relation indicate that the studied region is highly active with high attenuation. The resulted high value of n=1.2 is an artifact and can be considered as ~1.0. Similar, higher values of exponent *n*, has also observed for various highly active regions of world (Gupta *et al.,* 1988, Akinci *et al.,* 1994 & Vidales-Basurto *et al.,* 2014).

We compare in Fig. 16, obtained relation with regional relationships obtained by previous studies in the GoC region using different techniques. It is seen that Q_0-f^n relation obtained with the estimates of *Q* from the inversion matches with other relations obtained for this region within the variability of the estimates shown in Fig. 15. The higher values of *Q* reported by Vidales-Basurto *et al.,* (2014) are due to differences in the crustal volume sampled. Most of the paths sampled by them are outside the ridge zone and some includes the continental region. The estimates of Castro *et al.,* (2008) correspond to the Mexican Basin and Range Provence, inside the continent. The estimates of *Q* from the Imperial

Valley (Singh *et al., 1982)* are very similar to our estimates in south-central Gulf of California. These two regions have some geologic features in common, like the presence of sediments and high heat flow and explain the low values of *Q* obtained.

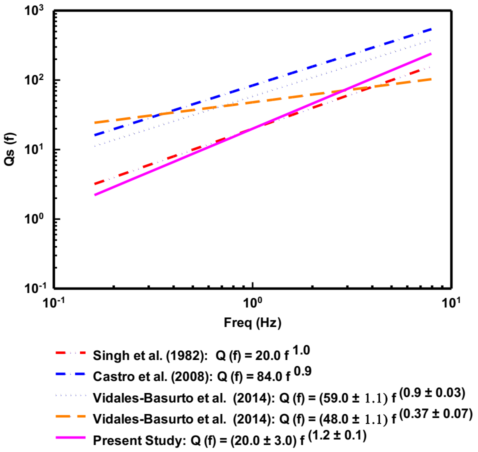

Figure 16. Comparison of obtained Q_0-f^n relation with other existing relations for the south-central GoC region.

CONCLUSIONS

A frequency-dependent three-dimensional shear wave attenuation structure for the south-central Gulf of California, Mexico has been obtained using 98 records from 25 earthquakes recorded at six different stations. A total of shear wave attenuation structures at 18 frequencies has been obtained in this work that permitted us to identify zones of high and low attenuation that correlate well with geological and tectonic models of the region. The iterative inversion scheme used in this work gives results consistent with crustal models proposed by Lizarralde *et al.,* (2007) and Teske *et al.,* (2014) for the Gulf of California region. The average shear wave quality factor obtained from the different 108 blocks at different frequencies from inversion has been further used to develop the regional frequency dependent shear wave quality factor of form $Qs\ (f) = 20\ f^{1.2}$. The developed relationship has been compared with that available for this region. The comparison establishes the reliability of obtained shear wave quality factors in different blocks.

ACKNOWLEDGEMENTS: Authors sincerely thank the Indian Institute of Technology, Roorkee, Roorkee, Uttarakhand, India and Centro de Investigación Científica y de Educación Superior de Ensenada (CICESE), Baja California, Mexico for supporting the study presented in this article. We acknowledge Dr. Claudia Vidales-Basurto and Dr. Lenin Avila-Barrientos, who provided the site response functions used. We thank Antonio Mendoza and Arturo Pérez-Vertti for facilitating data from the RESBAN array. The work presented in this paper is the outcome of the DST project grant no. DST/INT/MEXICO/P-03/2016; CONACYT-DST 266078 and CONACYT CB2017-2018-A1-S-37179. We would also like to thanks Dr. Roberto Ortega, CICESE, Mexico for his efforts and expertise for reviewing the manuscript, to improve the quality of article.

REFERENCES:

Aki, K. & Lee, W.H.K. (1976). Determination of the three- dimensional velocity anomalies under a seismic array using first p arrival time from local earthquakes. 1. A homogeneous initial model. *Journal of Geophysical Research, 81,* 4381-4399.

Aki, K., & Chouet, B. (1975). Origin of coda waves: source, Attenuation and scattering effects. *Journal of Geophysical Research, 80,* 3322-3342.

Akinchi, A., Taktak, A. G., and Ergintav, S. (1994). Attenuation of coda waves in western Anatolia. *Physics of Earth and Planetary Interiors,*87, 155–165.

Aki, K, (1980a). Attenuation of shear waves in the lithosphere for frequencies from 0.05 to 25 Hz. *Physics of Earth and Planetary Interiors, 21,* 50-60.

Aragon-Arreola, M. & Morandi, M. (2005). *Structure of the rift basins in the central Gulf of California; kinematic implications for oblique rifting. Tectonophysics, 409,* 19-38.

Avila-Barrientos, L. & Castro, R.R. (2016). Site response of the broad band stations of the NARS-Baja and RESBAN arrays, located in the region of the Gulf of California, México. *Geofísica Internacional,* 55, 131-154.

Backus, G.E., & Gilbert, J.F. (1968). The resolving power of gross earth data. *Geophysical Journal International, 16*, 169-205.

Bennett, S., Oskin, M., & Iriondo, A. (2007). Transition from Proto-Gulf extension to transtension, coastal Sonora, Mexico. *Eos, Trans. American Geophysical Union, 88*, 23.

Besana, G.M., Negishi, H. & Ando, M. (1997). The three-dimensional attenuation structures beneath the Philippine archipelago based on seismic intensity data inversion. *Earth and Planetary Science Letters, 151*, (1997).

Castro, R., Condori, C., Romero, O., Jacques, C., & Suter, M. (2008). Seismic Attenuation in Northeastern Sonora, Mexico. *Bulletin of the Seismological Society of America, 98(2),* 722-732.

Castro, R.R., Pérez-Vertti, A., Mendez, I., Mendoza, A., & Inzunza, L. (2011b). Location of moderate size earthquakes recorded by the NARS-Baja array in the Gulf of California region between 2002 and 2006. *Pure & Applied Geophysics, 168,* 1279–1292.

Castro, R.R., Stock J.M., Hauksson E., and Clayton R.W. (2017a). Source functions and path effects from earthquakes in the Farallon Transform Fault region, Gulf of California, Mexico that occurred on October 2013, *Pure and Applied Geoph*ysics, 174 (6), 2239-2256.

Castro, R.R., Stock, J.M., Hauksson, E. & Clayton, R.W. (2017b). Active tectonics in the Gulf of California and seismicity (M > 3.0) for the period 2002– 2014. *Tectonophysics, 719–720,* 4–16.

Castro, R.R., Mendoza-Camberos, A. & Perez-Vertti A. (2018a). The broadband seismological network (RESBAN) of the Gulf of California, Mexico, Seismological Research Letter, 89.

Castro R.R., Mendoza-Camberos, A. & Pérez-Vertti A. (2018b). Radiated seismic energy of earthquakes in the south–central region of the Gulf of California, Mexico. *Geophysical Journal International, 214 (2),* 990-1003.

Castro, R. R., Singh, S. K., Joshi, A., and Singh, S. (2019). Shear wave attenuation study in the south region of the Gulf of California, Mexico. *Bulletin of Seismological Society of America, 109,* 600–609.

Dorsey, J.R., Umhoefer, J.P., Oskin, E.M. & Arrowsmith, R. (2013). Rupturing Continental Lithosphere in the Gulf of California & Salton Trough. *GeoPRISMS Newsletter, Issue No. 30.*

Goff, J.A., Bergman, E.A., Solomon & S.C. (1987). Earthquake source mechanism and transform fault tectonics in the Gulf of California. *Journal of Geophysical* Research, 92, 10, 485–10, 510.

Gupta, S. C., Teotia, S. S., Rai, S. S., and Gautam, N. (1998). Coda Q estimates in the Koyna region, India. *Pure and Applied Geophysics, 153,* 713–731.

Hashida, T. & Shimazaki, K. (1984). Determination of seismic attenuation structure and source strength by inversion of seismic intensity data: method and numerical experiment. *Journal of physics of Earth, 32*, 299-316.

Hasegawa, H.S. (1985). Attenuation of Lg waves in the Canadian Shield. *Bulletin of the Seismological Society of America,75,* 1569 – 1582.

Joshi, A. (2007). *Inversion of seismic intensity data for the determination of three-dimensional attenuation structures in the central gap region of Himalayas. Natural Hazards 43*, 129–146.

Joshi, A., Mohanty, M., Bansal, A.R., Dimri, V.P., & Chadha, R.K. (2010). Use of spectral acceleration data for determination of three- dimensional attenuation structure in Pithoragarh region of Kumaon Himalayas. *Journal of Seismology, 14,* 247–272.

Knopoff, L. (1964). Q. *Reviews of Geophysics, 2*, 625-660.

Kumar, N., Parvez, I.A. & Virk, H.S. (2005). Estimation of coda wave attenuation for NW Himalaya region using local earthquakes. *Physics of Earth and Planetary Interiors, 151,* 243-258.

Kumar P., Joshi A., Sandeep, Kumar A., & Chadha R.K. (2015). Detailed attenuation study of shear waves in the Kumaon Himalaya, India, using the inversion of strong-motion data. *Bulletin of the Seismological Society of America, 105(4)*, 1836–1851.

Lonsdale P., (1989). Geology and tectonic history of the Gulf of California, in Winterer, E.L., *et al.*, eds., The Eastern Pacific Ocean and Hawaii:Boulder, Colorado, *Geological Society of America, Geology of North America, v. N, p.499–521.*

Luccio F. Di, Persaud P., & Clayton R.W. (2014). Seismic structure beneath the Gulf of California: a contribution from group velocity measurements. *Geophysical Journal International, 199,* 1861–1877.

Lizarralde, D., Axen G.J., Brown H.E., Fletcher J.M., González-Fernández A., Harding A.J., Holbrook W.S., Kent G.M., Paramo P., & Sutherland F. (2007). Variation in styles of rifting in the Gulf of California. *Nature, 448,* 466 – 469.

Nakamura, R. & Uetake, T. (2002): Three-dimensional attenuation structure and site amplification inversion by using a large quantity of seismic strong motion records in Japan. *Journal of the Seismological Society of Japan, 54,* 475-488.

Ortega, R., and González, M. (2007). Seismic wave attenuation and source excitation in La Paz-Los Cabos, Baja California Sur, Mexico. *Bulletin of Seismological Society of America, 97,* 545–556.

Ortega, R., and Quintanar, L. (2010). Seismic evidence of a ridge-parallel strike-slip fault off the transform system in the Gulf of California. *Geophysical Research latter, 37,* L06301.

Ortega, R., and Quintanar, L. (2011). A comparison between P-wave and S-wave propagation characteristics in the southern part of the Gulf of California, Mexico. *Bulletin of Seismological Society of America, 101,* 1270– 1280.

Pacheco, J.F. & Sykes L.R. (1992). Seismic moment catalog of large shallow earthquakes,1900 to 1989. *Bulletin of the Seismological Society of America, 82,* 1306–1349.

Paulssen, H., & de Vos, D. (2017). Slab remnants beneath the Baja California peninsula: seismic constraints and tectonic implications. *Tectonophysics, 719–720,* 27–36.

Persuad, P., Stock J.M., Steckler, M.S., Martin-Barajas, A., Diebold, J.B., Gonzalez-Fernandez, A. & Mountain, G.S. (2003). Active deformation and shallow structure of the Wagner, Consag, and Delfin basins, northern Gulf of California, Mexico. *Journal of Geophysical Research, 42(6),* 2355.

Persaud P., Luccio, F.Di., & Clayton R.W. (2014). Rayleigh wave dispersion measurements reveal low-velocity zones beneath the new crust in the Gulf of California. *Geophysical Research Letters, 42(6),* 1766-1774.

Quintanar, L., Ortega, R., Rodríguez-Lozoya, H.E., Domínguez-Reyes, T. (2019). The 4 January 2006 (M w 6.6), San Pedro Martir Earthquake: Example of an Earthquake for Calibrating Excitation and Attenuation Studies. *Bulletin of the Seismological Society of America, 109(6),* 2399–2414.

Rebollar, C.J., Quintanar, L., Castro, R.R., Day, S.M., Madrid, J., Brune, J.N., Astiz, L. & Vernon, F. (2001). Source characteristics of a 5.5 magnitude earthquake that occurred in the transform fault system of the Delfin Basin in the Gulf of California. *Bulletin of the Seismological Society of America, 91*, 781–791.

Rodríguez-Lozoya, H.E., Domínguez R.T., Quintanar R.L., Meléndez A.A., Rodríguez-Leyva H.E., Rocha W.P. & García-Páez F. (2017). Attenuation of Coda Waves in the Central Region of the Gulf of California, México. *Geofísica Internacional 56 (2),* 137-145.

Satake, K. & Hashida, T. (1989). Three-dimensional attenuation structure beneath North Island, New Zealand. *Tectonophysics 159,* 181–194.

Sharma, B., Teotia, S.S. & Kumar, D. (2007). Attenuation of P, S, and coda waves in Koyna region, India. *Journal of Seismology, 11,* 327–334.

Singh S.K., Aspel R.J., Fried J., & Brune J.N. (1982). Spectral attenuation of SH waves along the imperial fault. *Bulletin of Seismological Society of America*, 72, 2003-2016.

Stock, J.M., & Hodges K.V. (1989). Pre-Pliocene extension around the Gulf of California and the transfer of Baja California to the Pacific plate. *Tectonics, 8*, 99–115.

Sumy, D.F., Gaherty, J.B., Kim, W.Y., Diehl, T., & Collins, J.A. (2013). The mechanism of earthquakes and faulting in the southern Gulf of California. *Bulletin of the Seismological Society of America, 103,* 487–506.

Teske, A., Callaghan A.V., & LaRowe D.E. (2014). Biosphere frontiers of subsurface life in the sedimented hydrothermal system of Guaymas Basin. *Frontiers in Microbiology* 5:362.

Trampert, J., H. Paulsen, A. Van Wettum, J. Ritsema, R. Clayton, R. Castro, C. Rebollar & A. Pérez-Vertti (2003). New array monitors seismic activity near the Gulf of California in México. *EOS, Trans. American Geophysical Union, 84,* 29-32.

Umhoefer, P.J. (2011). Why did the Southern Gulf of California rupture so rapidly? Oblique divergence across hot, weak lithosphere along a tectonically active margin. *Geological Society of America Today, 21*, 4-10.

Van Eck T. (1988). Attenuation of coda waves in the Dead Sea region. *Bulletin of the Seismological Society of America, 78,* 770–779.

Vidales-Basurto, C.A., Castro, R.R., Huerta, C.I., Sumy, D.F., Gaherty, J.B. & Collins, J.A. (2014). An attenuation study of body waves in the south–central region of the Gulf of California, Mexico. *Bulletin of the Seismological Society of America, 104,* 2027–2042.

Original paper

DETECTION OF TOTAL WATER MASS CHANGES IN THE PATAGONIAN GLACIERS AREA BY SATELLITE GRAVIMETRY

Ayelen Pereira[1*], Cecilia Cornero[1], Ana C. O. C. Matos[2], M. Cristina Pacino[1] and Denizar Blitzkow[2].

Received: August 20, 2020; accepted: January 15, 2021; published online: April 1, 2021.

RESUMEN

La gravimetría satelital es una herramienta que aún no se aplica en profundidad para estudiar áreas relativamente extensas en los Andes de Argentina y Chile, a pesar de los esfuerzos actuales para lograr una mejor comprensión de los cambios en los glaciares y sus tendencias.

En este trabajo se analizan las variaciones de masa en los Hielos Patagónicos junto con las tendencias de decrecimiento en la región. El objetivo es demostrar la capacidad de la misión satelital GRACE (*Gravity Recovery and Climate Experiment*) para detectar los cambios en el almacenamiento de agua en áreas glaciarias. Además, se monitorearon las variaciones del nivel hidrométrico en lagos patagónicos, combinando datos de altimetría satelital y mediciones *in situ* con los cambios de masa de agua observados.

Para ello, se utilizaron datos GRACE para estimar la tendencia de la gravedad; y fueron usadas soluciones "mascons" de GRACE CSR RL05 de alta resolución, para analizar los cambios en el almacenamiento de agua de los campos de hielo en la región para el período 2002-2017.

Se utilizaron estaciones virtuales de altimetría satelital, además de información de altura hidrométrica de estaciones localizadas en lagos de la Patagonia en Argentina y Chile, con el fin de comparar el TWS de GRACE con el nivel de agua. Adicionalmente, se calcularon los coeficientes de correlación en cada estación.

Los resultados manifiestan una disminución significativa del almacenamiento de agua en la zona del Campo de Hielo, y además muestran que los Hielos Patagónicos Sur tienen una tendencia de derretimiento de las masas de hielo más pronunciada que en la región del norte, de aproximadamente 6 cm/año.

PALABRAS CLAVE: GRACE, Patagonia, glaciares, TWS, nivel de agua, altimetría satelital

ABSTRACT

Despite present efforts to better understand glacier changes and their trends, the satellite gravimetry is a powerful tool still not applied in-depth to study relatively large areas in the Andes of Argentina and Chile.

* *Corresponding author: apereira@fceia.unr.edu.ar*

[1] *Área de Geodinámica y Geofísica, Facultad de Ciencia Exactas, Ingeniería y Agrimensura, Universidad Nacional de Rosario-CONICET, Argentina*

[2] *Laboratório de Topografia e Geodesia, Escola Politécnica, Universidade de São Paulo (USP) and Centro de Estudos de Geodesia (CENEGEO), São Paulo/SP, Brazil*

In this work, the Patagonian Icefield mass variations are analyzed together with the decrease trends of the ice layer in the region. The purpose of this study is to demonstrate the GRACE satellite mission (Gravity Recovery and Climate Experiment) ability to detect water storage changes over the glaciers area. Furthermore, the variations of the hydrometric level in some Patagonian lakes were monitored by combining satellite altimetry data and *in situ* measurements with the observed water mass variations.

Data retrieved from GRACE were used to estimate gravity trends; and high-resolution GRACE CSR RL05 mascon solutions were used to analyze the icefields water storage change in the region under study for the 2002-2017 period.

Virtual stations from satellite altimetry obtained from a lake database and hydrometric height data from *in situ* stations, located at Patagonian lakes in Argentina and Chile, were also used in order to compare the TWS from GRACE to the water level of the specific lakes. Additionally, correlation coefficients were determined at each station.

The results show a significant water storage decrease in the Icefield area, and they also demonstrate that the ice melt in southern Patagonia (of about 6 cm/year) tends to be more pronounced than in the northern region.

KEY WORDS: GRACE, Patagonia, glaciers, TWS, water level, satellite altimetry.

INTRODUCTION

In response to the climate change in a global context, many glaciers are losing ice volume –and the Patagonian region is not an exception– which contributes to sea-level rise (Falaschi *et al.*, 2017; Gardner *et al.*, 2013; Hock *et al.*, 2009; Jacob *et al.*, 2012).

The largest temperate ice masses acknowledged in the southern hemisphere are also undergoing this melting process (Warren & Sugden,1993). Both the Northern and Southern Patagonian Icefields (hereafter, NPI and SPI, respectively) and their outlet glaciers, have shown high thinning rates since the second half of the 20th century (Rignot *et al.*, 2003; Willis *et al.*, 2012a; Willis *et al.*, 2012b).

The evolution of satellite gravimetric missions in the last years have introduced a new concept in the gravitational field modeling, allowing to obtain accurate global models with a higher resolution of the static component and in the time-dependent gravity field. In recent years, remote sensing data (such as altimetry-based surface water levels and total water storage from space gravimetry) have proved to be very helpful for studying the water balance at sub-basin and basin scales (Bamber & Rivera, 2007; Pereira *et al.*, 2014; Xavier *et al.*, 2010).

The GRACE (Gravity Recovery and Climate Experiment) satellite gravity mission can map the mass distribution by measuring the changes in the Earth's gravity field. These changes can be related to terrestrial water storage, which includes hydrological reservoir changes, snow, ice, and glaciers, and can be expressed in terms of equivalent water height (TWS). From GRACE, it is possible to detect these mass variations to a height of about 1 centimeter for areas ranging in size on the order of 400 km (Wahr *et al.*, 2004).

There are important contributions of GRACE data in the study of ice mass losses in Greenland (Chen J. L., 2006; Jin & Zou, 2015; Su *et al.*, 2015; Svendsen *et al.*, 2013), the Patagonian region

(Barcaza *et al.*, 2017; Chen *et al.*, 2007; Ciraci *et al.*, 2015; Falaschi *et al.*, 2017; Millan *et al.*, 2019; Richter *et al.*, 2019), the glaciers of the Tian Shan mountain chain (Yi *et al.*, 2016), Alaska (Chen J. L., 2006), and Antarctica (Jin *et al.*, 2016; Lee *et al.*, 2012).

Satellite altimetry and GRACE mission have been used to monitor the components of the water balance in large river basins over time scales ranging from months to decades. Space observations allow to obtain unprecedented information in combination with terrestrial data, providing global coverage, and continuous monitoring over time. In addition, they have the potential to significantly improve the understanding of hydrological processes in large river basins and their influence on climate variability.

Satellite altimetry allows the systematic monitoring of the oceans, rivers, lakes, wetlands, and flood plains water level (Papa *et al.*, 2008). Several satellites have been launched since the '90s, like ERS-1 (1991), TOPEX/POSEIDON (1992), ERS-2 (1995), GFO (2000), Jason-1 (2001), ENVISAT (2002), and Jason-2 (2008).

In recent decades, most Patagonian glaciers have retrogressed alarmingly fast with high decrease rates (Rivera & Casassa, 2002). Several studies about mass losses in the Patagonian icefield have been developed (Abdel *et al.*, 2019), like Rignot (2003), who estimated an ice loss of 15.0 ± 0.8 km^3 per year for the period 1975- 2000 (total amount in the northern and southern region). For the period 1995- 2000, this research estimated losses of about 37.7 ± 4.0 km^3 per year, which gives an idea of the accelerated ice melting in the last years.

The Intergovernmental Panel on Climate Change showed that since 1960 the accumulated losses in the Patagonian glaciers were about 40 m of ice thickness (Lemke *et al.*, 2007).

It is difficult to obtain the estimates of the ice loss for North and South Patagonian Icefields for several reasons, but mainly due to the lack of observations with adequate spatial and temporal sampling. The relatively small size of the region, the gradient of the slopes, and the undefined boundaries of the glaciers limit the utility of remote sensing techniques, such as laser or radar altimetry and interferometric synthetic aperture radar –InSAR- (Coudrain *et al.,* 2005; Braun *et al.*, 2019; Papa *et al.*, 2008).

There are multiple impacts associated with massive losses of glaciers and permanent icefields. One of the most direct consequences is the rise of sea levels due to the incorporation of a large amount of water from the ice melting. In addition, the loss of large ice areas implicates the loss of the reflective surface of the Earth as well, which will increase the warming due to an increment of the solar radiation absorbed by the Earth's surface (Gardner *et al.*, 2013).

The objective of this work is to detect the total water storage variations (TWS) in the Patagonian Icefield from GRACE data, together with the estimation of the decreasing trend for the NPI and SPI regions corresponding to the 2002-2017 period. Moreover, the water level variations in Patagonian lakes are analyzed using a combination of GRACE and satellite altimetry data with *in situ* measurements.

STUDY AREA

The glaciers have an important role in global freshwater storage since almost 70% of the world's freshwater is stored in glacial ice (Chen *et al.*, 2007). The icefields are vast rocky areas covered by ice sheets that comprise different geographical features, such as lakes and large mountain chains. According to geological and glaciological studies, the icefields would be remnants of areas formed during the last glaciation. These icefields also represent one of the main freshwater reservoirs in the world.

The main icefields in the Patagonian region are, on one hand, the Northern Patagonian Icefield (NPI), which is an ice mass that covers an area of 4,200 km^2 (Figure 1) and is entirely located in Chile. The Arenales Hill and San Valentín Mount, both covered by glaciers, are important because of their height of 3,437 and 3,910 meters, respectively. On the other hand, the Southern Patagonian Icefield (SPI), which is a large continental ice region located on the border between Argentina and Chile and covers an area of 13,000 km^2 (Figure 1). Numerous large glaciers arise from this, like the Montt, Pío XI (the largest of South America), Grey, Upsala, Viedma, and Perito Moreno. It is estimated that the SPI consists of 48 major glaciers and more than 100 minor glaciers.

In the Patagonian Andes, a large lake system can be found. Among the largest lakes in this system, the Buenos Aires/General Carrera, St. Martín/ O'Higgins, Viedma, and Argentino can be mentioned.

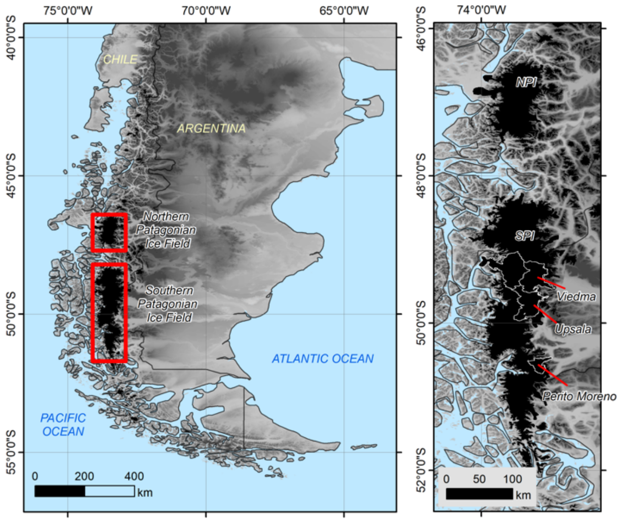

Figure. 1. Northern Patagonian Icefield (NPI) and Southern Patagonian Icefield (SPI) locations (left); and a detail of some glaciers in the region (right). The maps were generated with information from GLIMS Glacier Database (Raup *et al.*, 2007).

DATA

GRACE DATA

The observed gravity variations are caused by temporal mass changes. These mass variations can be considered as concentrated in a very thin water layer on the surface, with thickness changing in time. In fact, most of the temporal gravity variations are caused by changes in the water storage of the hydrological reservoirs, by mass movements in the oceans, atmosphere and cryosphere, and by the exchanges between them. The vertical extension of this layer of water is measured in centimeters, which is much smaller than the Earth's ratio or the horizontal variations scales - which are measured in kilometers- (Wahr *et al.*, 1998).

First, the GRACE Level-2 data corresponding to the period spanning from April 2002 to June 2017 were used for gravity trend analysis. Particularly, the solutions from CSR RL06 (Center for Space Research, University of Texas) were acquired (Bettadpur S., 2018).

Afterwards, the high-resolution GRACE CSR RL05 mascon solutions were used in this study in order to analyze the water mass variations of the Patagonian Icefields (Save *et al.,* 2016).

A *mascon* solution approach consists of a mass anomalies estimation at grid locations of certain *mas*s *con*centration. Then, these solutions provide the monthly time variations of the TWS at 1° of spatial resolution, resampled at 0.5°. Only GRACE measurements are used to derive these solutions, and they are not influenced by external geophysical models or data. In this approach, the *mascons* are related to the range-rate or the range-acceleration data by means of a spherical harmonic expansion, which is truncated at a finite order and degree (Save *et al.*, 2016).

IN SITU MEASUREMENTS

The National Hydrological Network is the largest source of hydrological information in Argentina and collects the basic data required for the design of projects and the national management of water resources. It is currently operated by several national institutions and has 369 measuring points, in many of which both hydrological and meteorological parameters are observed (SSRH, 2018).

The Basic Network of Water Information collects and processes the basic data of the quantity and quality of water resources with a significant presence in most part of the country, and provides hydrological information, which is available to the user through the development and implementation of the National System of Water Information (SNIH).

In this work, three stations with *in situ* water level measurements and daily time resolution were selected. These stations are located at the Argentino, Rico and Buenos Aires lakes (Figure 2), and their characteristics are shown in Table I.

The Buenos Aires station presented a lack of information in the period under study; however, it was still included since it was the only one located at the NPI.

SATELLITE ALTIMETRY DATA

Satellite altimetry is a technique that has great potential in hydrology, and for a lot of lakes located in areas that are difficult to access, it is the only source of information available.

The RADAR (Radio Detection and Ranging) altimeters used in satellite missions transmit a short microwave pulse in the nadir direction. The distance traveled by the electromagnetic pulse between the satellite and the Earth's surface is determined by measuring the time it takes for the pulse to be reflected back to the altimeter, assuming that the pulse propagates at the speed of light (Calmant *et al.,* 2008).

Then, the height of the reflecting surface is calculated by the difference between the satellite orbit and the altimeter range measurement. Several corrections in which time delays related to the propagation of the pulse through the atmosphere and the ionosphere are considered, as well as also corrections for solid tidal effects on the Earth, are after added.

Nowadays, there are several databases that allow obtaining the hydrometric heights in large basins of the world. The satellite water level information used in this work was obtained from DAHITI (Database for Hydrological Time Series of Inland Waters), which provides water level time series of lakes, reservoirs, rivers, and wetlands derived from multi-mission satellite altimetry for hydrological applications (Schwatke *et al.*, 2015). For the estimation of water heights, multi-mission altimeter data are used, such as Topex, Jason-1, Jason-2, Jason-3, Envisat, ERS-1, ERS-2, Cryosat-2, IceSAT, Sentinel-3A and Sentinel-3B.

In this study, two satellite altimetry virtual stations were selected from the DAHITI website, located at the Viedma and Argentino lakes (Figure 2 and Table I).

Table I. Virtual and terrestrial stations characteristics used in this study.

Lake	Latitude	Longitude	Icefield	Source
Buenos Aires	46.5388 S	71.6097 W	NPI	SNIH
Rico	50.4261 S	72.7478 W	SPI	SNIH
Argentino	50.3200 S	72.2610 W	SPI	SNIH
Argentino	50.2408 S	72.3985 W	SPI	Virtual
Viedma	49.6155 S	72.5125 W	SPI	Virtual

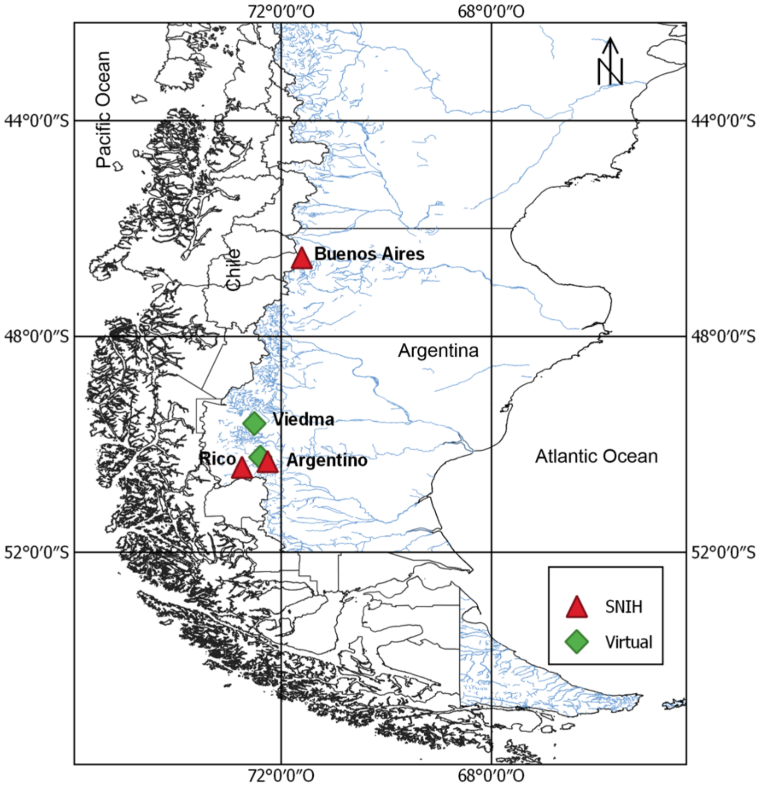

Figure 2. Virtual (green) and SNIH (red) stations at the Patagonian lakes: Buenos Aires corresponds to the NPI region; Argentino, Viedma and Rico, to the SPI.

METHODOLOGY AND RESULTS

GRAVITY TREND AND AMPLITUDE

The changes in time of the monthly gravity fields, δg, were determined by means of a 4-parameter trend analysis of the gravity disturbances. In order to do this, the trend and two yearly seasonal terms were estimated in each grid point of 0.5° x 0.5° (Sandberg Sørensen & Forsberg, 2010), where the result is the gravity trend obtained at satellite altitude (500 km):

$$\delta g(t) = a + b.t + c.\cos(2\pi t) + d.sen(2\pi t) \qquad (1)$$

First, a grid for the Patagonian Icefield region was determined, considering the area between 52º- 45° south latitude, and 75º- 71° west longitude.

To allow a fair comparison and limit the errors introduced to the high order coefficients, in all cases the data was filtered by truncating the spherical harmonic expansions (Forsberg & Reeh, 2006; Sandberg Sørensen & Forsberg, 2010). The calculations were essentially performed with the geodetic software Gravsoft (Tscherning *et al.*, 1992).

The resulting gravity trend (in µGal per year) for the area under study, based on GRACE Level-2 solutions, is shown in Figure 3.

In the Patagonian Icefield region, the gravity anomaly trend was negative for the entire area, with values ranging from -0.32 to -0.20 µGal/year. According to Figure 3, extreme values could be detected at the Southern Patagonian Icefield, in the proximity of the Viedma, Argentino and Rico lakes, delimited in Figure 2 from north to south, respectively.

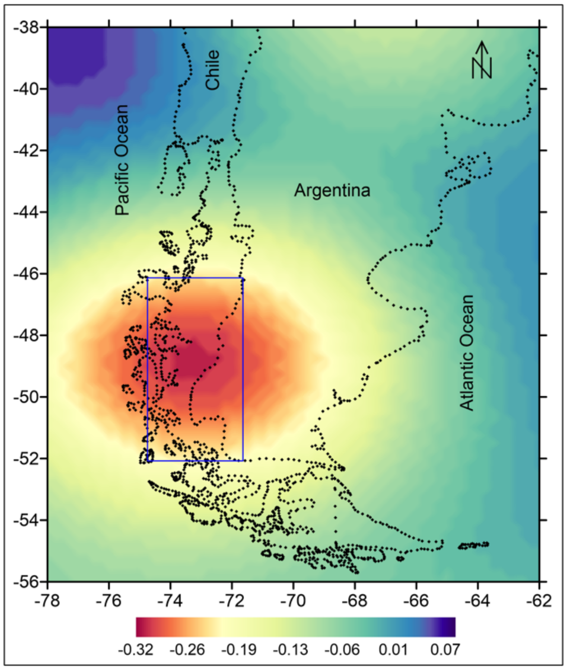

Figure 3. Gravity trend in µGal/year in the Patagonian Icefield for period 2002-2017 from GRACE Level-2 CSR RL06 data (the box corresponds approximately to the Patagonian Icefield)

PATAGONIAN ICEFIELD DECREASE TREND

In order to analyze the NPI and SPI regions, time series of TWS from CSR mascon solutions were obtained by averaging the points of the grid contained within the delimited boundary for each region.

In Figures 4 and 5, the TWS time series for the north and south regions are presented, respectively. Linear least squares trends of TWS were obtained for the north and south region, resulting trends of ~ - 61.70 ± 3.8 mm/year and ~ - 57.90 ± 3.4 mm/year, respectively.

The SPI shows a more pronounced negative trend line than the NPI region, which indicates a greater speed of level melting of ice masses towards the south (about 4 cm/year).

It should be noted that these water mass change values, interpreted as ice melting, may be influenced by other causes that contribute to the mass variation, which is also detected by GRACE, e.g. groundwater storage fluctuations in nearby areas.

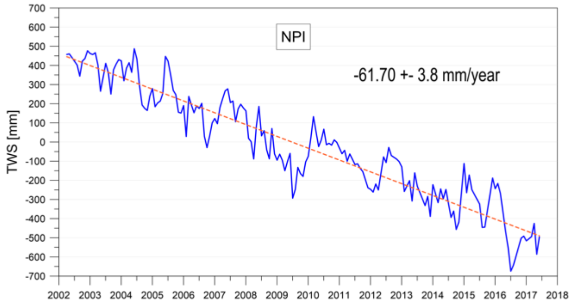

Figure 4. Total water storage (TWS) and trend line for NPI.

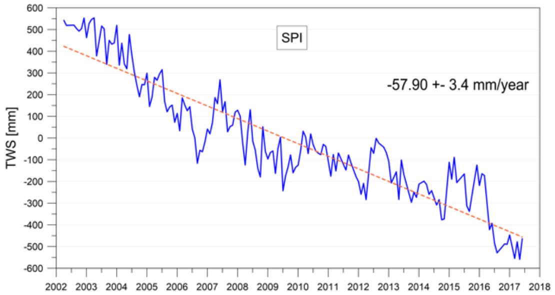

Figure 5. Total water storage (TWS) and trend line for SPI.

Chen *et al.* (2007) carried out a study on the melting rate of the ice mass for the whole region during the period 2002- 2006 and estimated a value of 27.9 ± 11 km^3/year, which is rather high considering the small extension of the Patagonian Ice region. This estimate contributes to a sea level rise of approximately 0.078 ± 0.031 mm/year. These values obtained from GRACE are comparable with other estimations of the melt rate obtained from topographic and cartographic data made by Rignot *et al.* (2003).

In this investigation, no rate estimates were made, as there are other geophysical contributions to GRACE observations that have an effect on the mass variations for this area specifically, such as the postglacial rebound of the Earth's mantle due to the change in the ice load from the last maximum glaciations up to the present day ice melting. In this sense, it is not object of the present investigation to estimate rates of decrease; the study is then limited to the analysis of the GRACE signals for each region, considering that the greater mass variation is due to the melting of glaciers, but there are other contributions to that change, as mentioned above.

Chen (2006) also estimated the slope of TWS for a point located at the Pío XI glacier - one of the largest glaciers in the southern Patagonian ice region – resulting 37.4 ± 2.1 cm/year for a 5-year period. Although the results are not similar, the TWS trend values obtained in this research are not so distinct from each other, considering that the regions are different, as well as the methodology used in each investigation.

TWS monthly maps were derived from GRACE CSR RL05 mascons for the period 2002 to 2017. The mean annual TWS was also obtained, taking into account the available GRACE months (e.g. for 2017 year, the mean was obtained up to June).

Figure 6 presents the mean annual TWS maps, where the progressive decreasing of the TWS in the NPI and SPI area from 2002 to 2017 can be observed.

COMPARISON AT PATAGONIAN LAKES

For the sake of analysis of the TWS results from GRACE in the glacier´s area, such results were compared with hydrometric heights series and satellite altimetry data of Patagonian lakes located in Argentina and Chile.

The *in situ* river gauge time series (SNIH) and the virtual stations from satellite altimetry of 30 day intervals were computed in two steps in order to make the data consistent with the TWS data derived from GRACE. First, the missing data series were completed using moving averages; and subsequently, the averages for 30 days intervals were obtained. The TWS temporal series were then interpolated to obtain the water storage at the same hydrometric station (*HH*) with bilinear interpolation using the nearest neighbor method.

In Figures 7 and 8, the series of hydrometric height (from SNIH) and the virtual station (from DAHITI) are presented respectively together with the GRACE time series. It can be observed for all the stations that the TWS signal is decreasing in the period 2002-2017, while the water level of the lakes shows a periodic behavior. Furthermore, the seasonal performance and the adjusted trend line for the TWS and the water level series are presented in Figure 7 (right), where the increasing of both variables can be perceived, starting in the summer (of southern hemisphere) to the early autumn, in correspondence with the precipitation regime of the region.

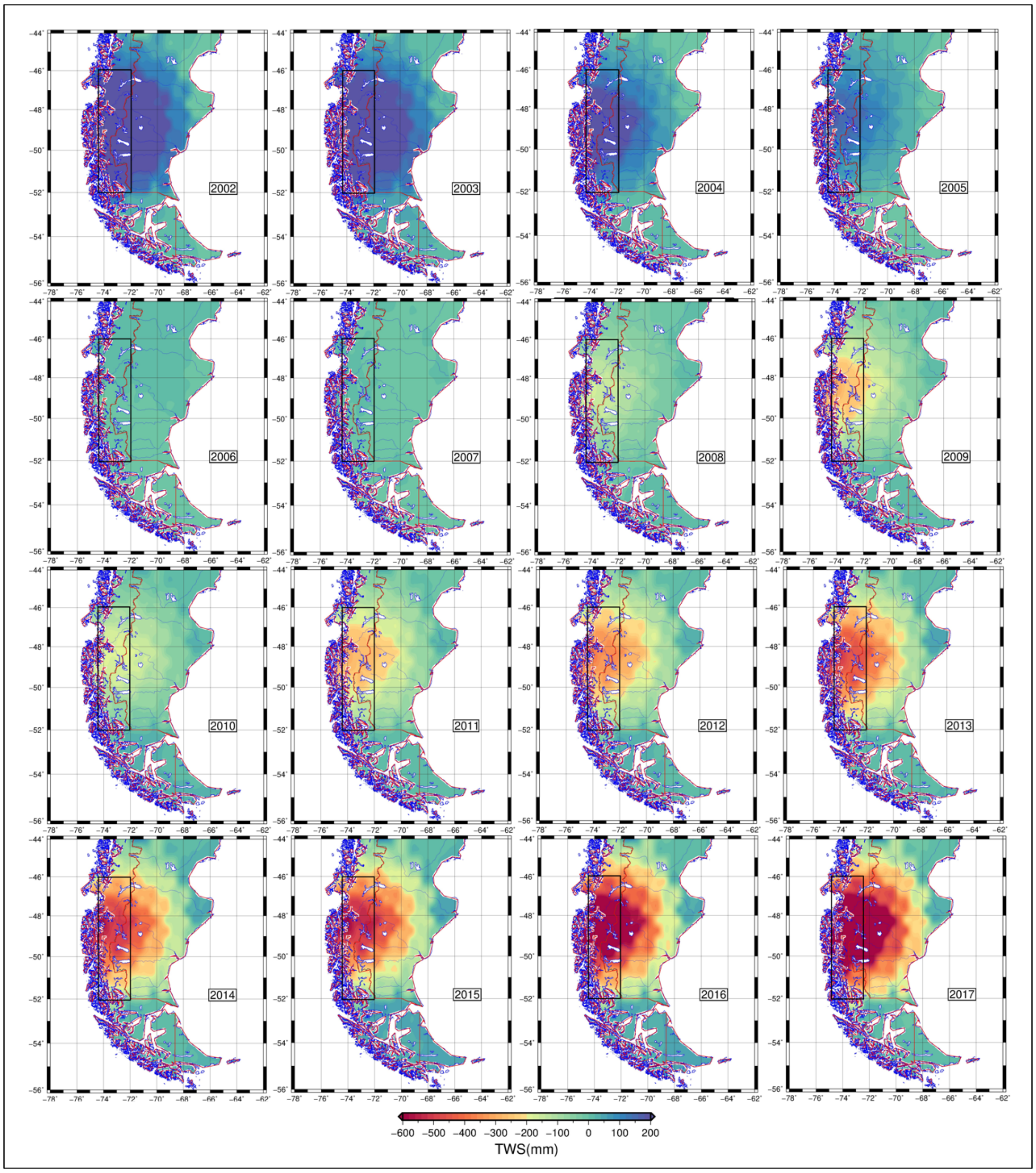

Figure. 6. Mean annual TWS maps from GRACE data showing the progressive decrease in the NPI and SPI region detected in the period 2002-2017.

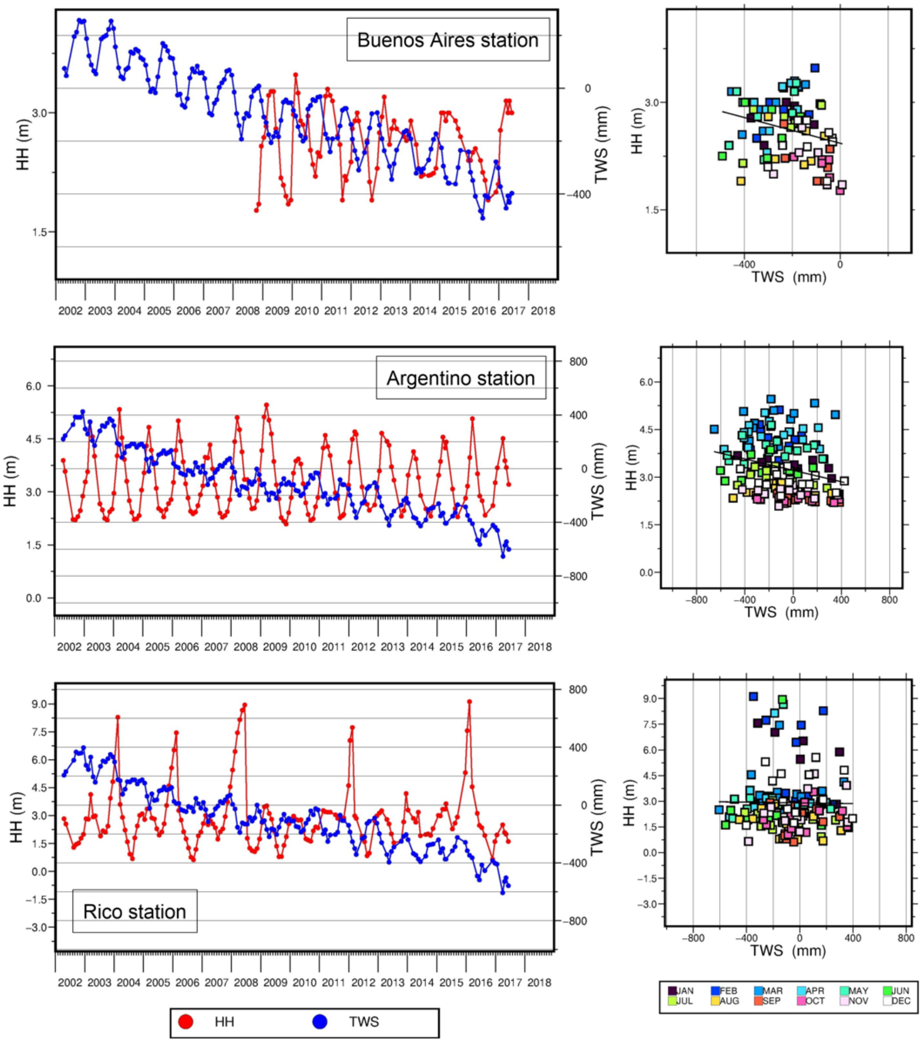

Figure7. Hydrometric height (HH) vs. TWS, trend line and seasonal behavior for both signals, for stations Buenos Aires (NPI), Argentino (SPI), and Rico (SPI).

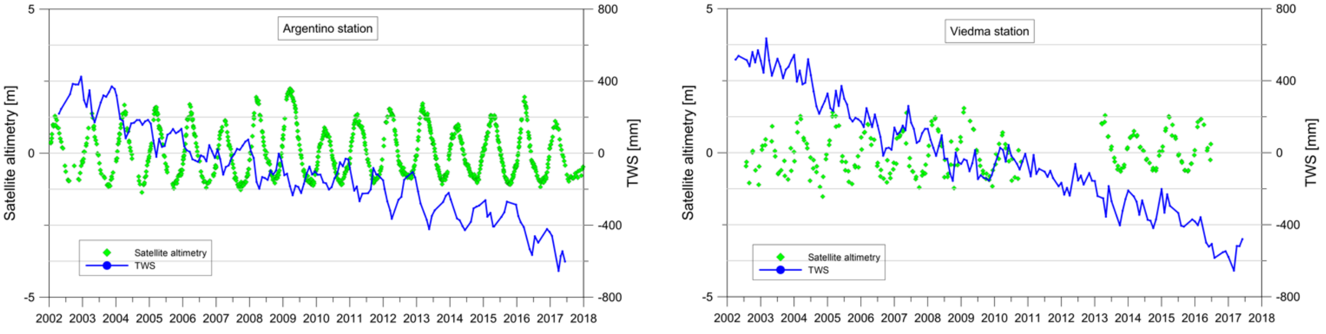

Figure 8. Water level (virtual stations from satellite altimetry) vs. TWS for Argentino and Viedma stations.

Afterwards, the Pearson coefficient *r* was obtained to evaluate the correlation between the analyzed variables.

At this point, it is important to mention that the TWS data and the hydrometric heights represent different magnitudes. While GRACE "sees" the total water storage as a vertical column composed of surface water, groundwater and soil moisture integrated over a time period (monthly), the hydrometric height represents the water level reached in a section of a lake that can be measured on a daily basis.

The resulting Pearson coefficients for the stations at the Patagonian lakes are shown in Table II. According to the results, the Argentino station (SNIH), located at SPI, presented the highest correlation value (over 50%). The remaining stations located in the south, both terrestrial and virtual, showed very low *r* coefficients; while the only one station at NPI -Buenos Aires- presented a Pearson correlation value close to 0.50.

Table 2. Pearson correlation coefficient r (dimensionless) for the Patagonian lakes.

Lake	**Source**	**Icefield**	**Pearson**
Buenos Aires	SNIH	NPI	-0.48
Rico	SNIH	SPI	-0.05
Argentino	SNIH	SPI	-0.55
Argentino	Virtual	SPI	0.17
Viedma	Virtual	SPI	0.10

DISCUSSION AND CONCLUSIONS

At the Patagonian region, the negative trend of the detected gravity anomalies could be mainly due to the redistribution of water, ice, and snow, and related to the climate change that is causing regression and loss of the ice mass in most of the Patagonian glaciers.

The analysis of the Patagonian Icefield area was performed for two sub-regions, the Northern Patagonian Icefield (NPI) and the Southern Patagonian Icefield (SPI). Then, the time series of TWS were obtained for each region by averaging the grid points within the boundaries for the NPI and SPI areas.

The results showed that the SPI region presents a more pronounced negative trend than the NPI region, which indicates a greater speed of the level melting of ice masses towards the south. Linear trends of total water storage were obtained for the north and south regions, resulting in values of -61.70 mm/year and -57.90 mm/year, respectively. Likewise, this negative trend was also demonstrated in the TWS maps, which showed the progressive total water storage decrease for the period 2002-2017.

According to the study of the Patagonian lakes, the SNIH stations Buenos Aires and Argentino presented a strong negative correlation –of about 0.5-. Meanwhile, for the rest of the stations located at the SPI (both terrestrial and virtual) very low correlation coefficients were obtained. The results for the SNIH stations indicate a negative association, which is revealed through the behavior of the different TWS (decreasing) and hydrometric height (mainly seasonal) signals.

The weak correlation obtained for some stations in the Patagonian lakes may be due to the influence of the nearby glaciers. The GRACE signal indicates a negative trend in the TWS, while the hydrometric level signal does not detect the same decrease. This indicates that GRACE measurements may be affected by the proximity of other zones with different hydrological characteristics.

It can be concluded that the use of GRACE data and satellite altimetry is feasible to detect variations of the hydrometric levels in the Patagonian lakes only in those areas where there is no influence of the environment. That is to say, if the surrounding area is homogeneous, then the changes in the regional water mass may be linked to punctual variations to make valid comparisons with local variables, as in the case of a gauge station (hydrometric heights). Otherwise, GRACE detects the lake- glacier water storage change, but it is not comparable with changes in the levels of the lake measured *in situ* or by satellite altimetry in the South Patagonian region. This means that the glacier signal derived from GRACE was stronger, masking all other signals in its neighborhood. Therefore, further investigations in this topic should be carried out.

Regarding satellite altimetry, it can be mentioned that it is useful for the comparison of GRACE results in those places where there are no *in situ* available information. In such comparisons, since no records were obtained in order to complement this analysis, the groundwater variations were not taken into account.

ACKNOWLEDGEMENTS: This work was partially supported by CONICET, PICT 2015-1180 (ANPCyT) and ING-561 (UNR).

REFERENCES:

Abdel Jaber W., Rott H., Floricioiu D., Wuite J., and Miranda N. (2019). Heterogeneous spatial and temporal pattern of surface elevation change and mass balance of the Patagonian ice fields between 2000 and 2016, *The Cryosphere*, 13, 2511–2535, https://doi.org/10.5194/tc-13-2511-2019.

Bamber J., Rivera A., (2007). A review of remote sensing methods for glacier mass balance determination. Global and Planetary Change, (59), 138-148, doi: 10.1016/j.gloplacha.2006.11.031.

Barcaza G., Nussbaumer S. U., Tapia G., Valdés J., García J. L., Videla Y., Albornoz A., Arias V., (2017). Glacier inventory and recent glacier variations in the Andes of Chile, South America. *Annals of Glaciology* 58 (75pt2), doi: 10.1017/aog.2017.28.

Bettadpur S. (2018). UTCSR Level-2 Processing Standards for Level-2 Product Release 0006 (Rev 5.0 Apr 18, 2018) GRACE 327-734, Center for Space Research, University of Texas at Austin.

Braun M.H., Malz P., Sommer C., Farías-Barahona D., Sauter T., Casassa G., Soruco A., Skvarca P., and Seehaus T.C. (2019). Constraining glacier elevation and mass changes in South America. *Nature Clim Change* 9, 130–136, https://doi.org/10.1038/s41558-018-0375-7.

Calmant S., Seyler F. and Cretaux J. F., (2008). Monitoring continental surface waters by satellite altimetry. *Surveys in Geophysics*, 29(4-5), 247-269.

Chen J. L., Tapley B. D., & Wilson C. R., (2006). Alaskan mountain glacial melting observed by satellite gravimetry. *Earth and Planetary Science Letters*, 248(1–2), 353–363.

Chen J. L. (2006). Satellite Gravity Measurements Confirm Accelerated Melting of Greenland Ice Sheet. *Science*, 313(5795), 1958–1960.

Chen J. L., Wilson C. R., Tapley B. D., Blankenship D. and Ivins E. R., (2007). Patagonia Icefield melting observed by Gravity Recovery and Climate Experiment (GRACE). *Geophysical Research Letters*, Vol. 34, L22501, doi:10.1029.

Coudrain A., Francou B., Kundzewicz Z. W., (2005). Glacier shrinkage in the Andes and consequences for water resources. *Hydrological Sciences Journal*, (50)6, 925-932, doi:10.1623/hysj.2005.50.6.925.

Ciraci E., Velicogna I., Wahr J. M. & Swenson S. C., (2015). Mass loss of glaciers and ice caps from GRACE during 2002-2015. In AGU Fall Meeting Abstracts.

Falaschi D., Bolch T., Rastner P., Lenzano M. G., Lenzano L., Lo Vecchio A., & Moragues S., (2017). Mass changes of alpine glaciers at the eastern margin of the Northern and Southern Patagonian Icefields between 2000 and 2012. *Journal of Glaciology*, 63(238), 258–272, doi: org/10.1017/jog.2016.136.

Forsberg R., Reeh N., (2006). Mass change of the Greenland ice sheet from GRACE. Proc. First meeting of the International Gravity Field Service: Gravity Field of the Earth 2006, Springer Verlag.

Gardner A. S., Moholdt G., Cogley J. G., Wouters B., Arendt A. A., Wahr J., Berthier E., Hock R., Pfeffer W. T., Kaser G., Ligtenberg S. R. M., Bolch T., Sharp M. J., Hagen J. O., Van den Broeke M. R. and Paul F., (2013). A reconciled estimate of glacier contributions to sea level rise: 2003 to 2009. *Science*, 340(6134), 852–857. http://doi.org/10.1126/science.1234532.

Hock R., De Woul M., Radic V., & Dyurgerov M., (2009). Mountain glaciers and ice caps around Antarctica make a large sea-level rise contribution. *Geophysical Research Letters*, 36(7), 1–5. http://doi.org/10.1029/2008GL037020.

Jacob T., Wahr J., Pfeffer W. T., & Swenson S., (2012). Recent contributions of glaciers and ice caps to sea level rise. *Nature*, 482(7386), 514–518. http://doi.org/10.1038/nature10847.

Jin S., & Zou F., (2015). Re-estimation of glacier mass loss in Greenland from GRACE with correction of land-ocean leakage effects. *Global and Planetary Change*, 135, 170–178.

Jin S., Abd-Elbaky M., & Feng G., (2016). Accelerated ice-sheet mass loss in Antarctica from 18-year satellite laser ranging measurements. *Annals of Geophysics*, 59(1).

Lee H., Shum C. K., Howat I. M., Monaghan A., Ahn Y., Duan J., Guo J-Y., Kuo C-Y and Wang L., (2012). Continuously accelerating ice loss over Amundsen Sea catchment, West Antarctica, revealed by integrating altimetry and GRACE data. *Earth and Planetary Science Letters*, 321–322, 74–80.

Lemke P., Ren J., Alley R. B., Allison I., Carrasco J., Flato G., Fujii Y., Kaser G., Mote P., Thomas R. H. and Zhang T., (2007). Observations: Changes in Snow, Ice and Frozen Ground. In: Climate Change 2007: The Physical Science Basis. Contribution of Working Group I to the Fourth Assessment Report of the Intergovernmental Panel on Climate Change [Solomon, S., D. Qin, M. Manning, Z. Chen, M. Marquis, K.B. Averyt, M. Tignor and H.L. Miller (eds.)]. Cambridge University Press, Cambridge, United Kingdom and New York, NY, USA.

Millan R., Rignot E., Rivera A., Martineau V., Mouginot J., Zamora R., Uribe J., Lenzano G., De Fleurian B., Li X., Gim Y., and Kirchner D., (2019). Ice thickness and bed elevation of the Northern and Southern Patagonian Icefields. Geophysical Research Letters, 46, 6626– 6635. https://doi.org/10.1029/2019GL082485.

Papa F., Güntner A., Frappart F., Prigent C., and Rossow W. B., (2008). Variations of surface water extent and water storage in large river basins: A comparison of different global data sources. *Geophys. Res. Lett.*, 35, L11401, doi:10.1029/2008GL033857.

Pereira A., Cornero C., Pacino M. C. & Oliveira, A. C., De Matos C., (2014). Using geotechnologies for mapping water storage changes in the Pampeana region from GRACE data. *Geoacta*, 39(1), 1–10.

Ramillien G., Frappart F., Cazenave A. and Güntner A., (2005). Time variations of the land water storage from an inversion of 2 years of GRACE geoids, *Earth Planet. Science Lett.*, 235, 283-301.

Raup B.H., Racoviteanu A., Khalsa S.J.S., Helm C., Armstrong R., Arnaud Y., (2007). The GLIMS Geospatial Glacier Database: a New Tool for Studying Glacier Change. *Global and Planetary Change* 56:101-110. (doi:10.1016/j.gloplacha.2006.07.018)

Richter A., Groh A., Horwath M., Ivins E., Marderwald E., Hormaechea J.L., Perdomo R., Dietrich R., (2019). The Rapid and Steady Mass Loss of the Patagonian Icefields throughout the GRACE Era: 2002–2017. *Remote Sens*. 2019, 11, 909.

Rignot E., Rivera A. & Casassa G., (2003). Contribution of the Patagonia ice fields of South America to sea level rise. *Science*, 302(5644), 434- 437, doi:10.1126/science.1087393.

Rivera A. & Casassa G., (2002). Detection of ice thickness using radio echo sounding on the Southern Patagonia Icefield. In Casassa, G. Sepulveda, F., and Sinclair, R.(eds.), The Patagonian Icefields: A Unique Natural Laboratory for Environmental and Climate Change Studies. Series of the Centro de Estudios Científicos. New York: Kluwer Academic/Plenum Publishers, 101–115.

Sandberg Sørensen L. & Forsberg R., (2010). Greenland ice sheet mass loss from GRACE monthly models. *Gravity, Geoid and Earth Observation*, (135), 527–532, doi:10.1007/978-3-642-10634-7 70.

Save H., Bettadpur S., and Tapley B. D., (2016). High resolution CSR GRACE RL05 mascons, *J. Geophys. Res. Solid Earth*, 121, 7547–7569, doi: 10.1002/2016JB013007.

Schwatke, C., Dettmering, D., Bosch, W., and Seitz, F. (2015). DAHITI - an innovative approach for estimating water level time series over inland waters using multi-mission satellite altimetry, *Hydrol. Earth Syst. Sci.*, 19, 4345-4364, doi:10.5194/hess-19-4345-2015, 2015.

SSRH Subsecretaría de Recursos Hídricos, Argentina. Información acerca del Sistema Nacional de Información Hídrica. Available at <http://www.hidricosargentina.gov.ar/InformacionHidrica.html>. Accessed in August 2018.

Su X., Shum C. K., Guo J., Duan J., Howat I., & Yi Y., (2015). High resolution Greenland ice sheet inter-annual mass variations combining GRACE gravimetry and Envisat altimetry. *Earth and Planetary Science Letters*, 422, 11–17.

Svendsen P. L., Andersen O. B., & Nielsen A. A., (2013). Acceleration of the Greenland ice sheet mass loss as observed by GRACE: Confidence and sensitivity. *Earth and Planetary Science Letters*, 364, 24–29.

Tscherning C.C., Forsberg R., & Knudsen P., (1992). The GRAVSOFT package for geoid determination. Continued Workshop on the European Geoid.

Wahr J., Molenaar M. & Bryan F., (1998). Time-variability of the Earth's gravity field: hydrological and oceanic effects and their possible detection using GRACE. *Journal of Geophysical Research*, 103, 30205-30230.

Wahr J., Swenson S., Zlotnicki V., Velicogna I., (2004). Time-variable gravity from GRACE: First results. *Geophysical Research Letters*, Jun 9, 2004, Vol. 31, Iss. 11, pp. 4.

Warren C. & Sugden D., (1993). The Patagonian Icefields: a glaciological review. *Arctic and Alpine Research*, 25(4), 316-331. doi:10.2307/1551915.

Willis M. J., Melkonian A. K., Pritchard M. E., & Ramage J. M., (2012a). Ice loss rates at the Northern Patagonian Icefield derived using a decade of satellite remote sensing. *Remote Sensing of Environment*, 117, 184–198. http://doi.org/10.1016/j.rse.2011.09.017.

Willis M. J., Melkonian A. K., Pritchard M. E., & Rivera A., (2012b). Ice loss from the Southern Patagonian Ice Field, South America, between 2000 and 2012. *Geophysical Research Letters*, 39(17), 1-6. http://doi.org/10.1029/2012GL053136.

Xavier L., Becker M., Cazenave, Longuevergne L., Llovel W. and Rotunno Filho O.C., (2010). Interannual variability in water storage over 2003–2008 in the Amazon Basin from GRACE space gravimetry, in situ river level and precipitation data. *Remote Sensing of Environment*, 114 (8), 1629-1637. doi:10.1016/j.rse.2010.02.005.

Yi S., Wang Q., Chang L., & Sun W., (2016). Changes in mountain glaciers, lake levels, and snow coverage in the Tianshan monitored by GRACE, ICESat, altimetry, and MODIS. *Remote Sensing*, 8(10), 798.

Artículo original

LA MAGNETOMETRÍA COMO ALTERNATIVA PARA IDENTIFICAR ÁREAS CON POTENCIAL ACUÍFERO. EL CASO DE LA CUENCA BAJA DEL RÍO GRIJALVA

Rubén de Jesús Escudero-Durán[1], Marco Rogelio Bustamante-Orozco[1], Edgar Ángeles-Cordero[2], Iris Neri-Flores[3] y Ojilve Ramón Medrano-Pérez[4*]

Recibido: agosto 29, 2019; aceptado: marzo 18, 2021; publicado en línea: abril 1, 2021

RESUMEN

El objetivo principal de esta investigación es identificar las áreas de unidades de rocas con potencial acuífero en las subcuencas de la porción oeste de la cuenca baja del río Grijalva, mediante la interpretación de las respuestas magnéticas obtenidas aplicando diversos algoritmos matemáticos para la detección de bordes estructurales (*i.e.*, Gradiente Horizontal, Señal Analítica y Derivada TILT) y la elaboración de modelos 3D de la zona estudiada a base de *voxels*. Para ello, se realizó el procesado de datos aeromagnéticos, con el propósito de resaltar e identificar las características geológicas sobresalientes en el área de estudio. Los resultados obtenidos permitieron identificar zonas asociadas a espesores sedimentarios que, cuando se correlacionan con los datos altimétricos, permiten inferir que la zona centro-norte alberga el área con mayor potencial acuífero en la porción oeste de la cuenca baja del río Grijalva. De esta manera, se busca contribuir al conocimiento local y propiciar la toma de decisiones en los temas geohidrológicos, ordenamiento territorial y políticas públicas relacionadas.

PALABRAS CLAVE: métodos potenciales, hidrogeofísica, potencial acuífero, gestión del agua subterránea, cuenca Grijalva.

ABSTRACT

The main objective of this research is to identify aquifer potential areas of rock units within the sub-basins of the western portion of the lower basin of the Grijalva River by interpreting the magnetic responses obtained by applying various edge detection algorithms (*i.e.*, Horizontal Gradient, Analytical Signal and TILT Derivative) and developing 3D models of the studied area based on voxels. For this, the processing of aeromagnetic data was carried out with the purpose of highlighting and identifying the outstanding geological characteristics. The results obtained allowed the identification of zones associated with sedimentary thicknesses which, when correlated with the altimetry data, allow us to infer that the north-central zone harbor the area

**Autor de correspondencia: ojilve.medrano@ccgs.mx*

[1] *División Académica de Ciencias Básicas (DACB), Universidad Juárez Autónoma de Tabasco (UJAT), Tabasco, México*

[2] *Profesor Investigador, Ingeniería Petrolera, Universidad Politécnica de Chiapas (UPChiapas), Suchiapa, Chiapas, México*

[3] *Escuela Nacional de Estudios Superiores Mérida. Tablaje Catastral N°6998, Carretera Mérida-Tetiz Km. 4.5, Municipio de Ucú, Yucatán, México, C. P. 97357*

[4] *Cátedra CONACYT−Centro del Cambio Global y la Sustentabilidad, A.C. (CCGS), Villahermosa, Tabasco, México*

with the greatest aquifer potential in the western portion of the lower basin of the Grijalva River. Thus, it seeks to contribute local knowledge and promote decision-making in geohydrological issues, territorial planning and related public policies.

KEY WORDS: potential methods, hydrogeophysics, aquifer potential, groundwater management, Grijalva basin.

INTRODUCCIÓN

Los recursos hídricos en México se caracterizan por asimetrías territoriales y temporales en la disponibilidad natural del agua, con el agravante de que la concentración espacial de la población y la economía se encuentran en las regiones con menor disponibilidad. A diferencia de las regiones norte y centro, el sureste presenta el mayor escurrimiento, dotando así a esta región de una riqueza hídrica privilegiada. Sin embargo, en contraste con el norte y centro, esta región posee menor población y una alta marginalidad (CONAGUA, 2018).

En México, de acuerdo con CONAGUA (2018) la disponibilidad natural media anual de agua, o agua renovable, al 2017 alcanza los 451,585 hm^3/año (incluye las importaciones y exportaciones con países vecinos) que, al dividirse por la población del 2017, se tiene una disponibilidad per cápita de 3,656 m^3/hab./año. Asimismo, del total de agua disponible se extraen 87.84 miles hm^3 para uso consuntivo (19.5%), donde el 61% es de fuentes superficiales y el 39% de subterráneas, y los usos agrícolas y abastecimiento público son los principales usuarios. Sin embargo, estas cifras no muestran la dependencia de agua subterránea en diversos territorios que, por sus condiciones climáticas y geomorfológicas o por las presiones demográficas y económicas, ven limitados sus recursos superficiales (Peñuela-Arévalo & Carrillo-Rivera, 2013). Así, Spring & Cohen (2012) indican que, como consecuencia de la concentración espacial del crecimiento de la población, la producción agrícola e industrial, y la distribución natural del recurso (espacial y temporal), la disponibilidad de agua per cápita es cada vez más limitada. Lo que, en efecto, se manifiesta en las distintas regiones donde estos factores convergen, principalmente, centro y norte del país.

No obstante, de ambos recursos, superficial y subterráneo, el agua subterránea es el de menor comprensión y entendimiento en el país (Hatch-Kuri, 2017; López-Morales, 2017). De hecho, Peñuela-Arévalo & Carrillo-Rivera (2013) consideran que el agua subterránea no solo es uno de los elementos que mayor impacto negativo ha sufrido desde la última mitad del siglo XIX, sino también que hasta ahora existe poco interés estatal en el estudio y análisis de su dinámica y funcionamiento. En este contexto, México enfrenta una serie de desafíos hídricos como la contaminación, el impacto del cambio climático en el ciclo hidrológico (Ojeda-Olivares *et al.*, 2019), la escasez de agua, el fortalecimiento de la gestión del agua con la participación de los usuarios, promover una buena planificación ambiental, así como impulsar la investigación y la tecnología (Cortés *et al.*, 2012). En particular, en esto último, el uso de técnicas geofísicas puede contribuir al conocimiento y comprensión de las aguas subterráneas del país (CONAGUA, 2007).

Los métodos geofísicos de exploración son esenciales para inferir y estimar la distribución de las propiedades físicas de los materiales del subsuelo. En particular, para este propósito existen los métodos gravimétricos y magnéticos, conocidos como métodos potenciales. Estos se aplican tanto en áreas urbanas como rurales (Henderson, 1992; Campos-Enríquez *et al.*, 1997; Huizar-Álvarez *et al.*, 1997; Campos-Enríquez *et al.*, 1997; Flores-Márquez *et al.*, 1998; López-Loera, 2014), o en sectores como la industria petrolera (Ndougsa-Mbarga *et al.*, 2007), la explotación de recursos minerales, la agricultura, geotermia, geología, arqueología, forense y la hidrología (Silva, 1974; Allred *et al.*, 2008; Robinson *et al.* 2008; Reynolds, 2011; Alatorre-Zamora *et al.*, 2015; Tinivella *et al.*, 2013; Binley *et al.*, 2015; Romero-Ruiz *et al.* 2018; Florsch *et al.*, 2019). De tal modo, la magnetometría es considerada un método versátil y de fácil operación que puede ser aplicado a distintos problemas de exploración del subsuelo (Ernstson, 2006). En particular, entre otras cosas, puede ayudar a determinar regiones con potencial acuífero por medio de la identificación de estructuras geológicas que podrían estar asociadas con la permeabilidad (fracturamiento), como ha sido reportado por López-Loera (2014).

La aplicación de los métodos geofísicos a la hidrología no es reciente, la hidrogeofísica, como disciplina de la geofísica para investigar procesos hidrológicos, se ha fortalecido en los últimos años debido a los avances y la disminución de costos en la tecnología e instrumentación (Hubbard & Rubin, 2005; Robinson *et al.*, 2008). En los últimos años, desde la hidrogeofísica, el uso de métodos geofísicos ha estado enfocado en investigaciones hidrogeológicas, en el conocimiento de problemas ambientales e infiltración de contaminantes en el suelo, en el mapeo de las características del subsuelo, en la variabilidad espacial y temporal de la humedad del suelo, en el funcionamiento biogeoquímico del sistema agua-suelo, en el estudio de procesos hidrológicos, y en las interacciones de las aguas subterráneas con las superficiales y costeras (Hubbard & Rubin, 2005; Vereecken *et al.*, 2006; Robinson *et al.*, 2008; Kirsch, 2009; Binley *et al.*, 2015; Brocca *et al.*, 2017; Romero-Ruiz *et al.*, 2018; Florsch *et al.*, 2019).

No obstante, si bien el uso de métodos eléctricos y electromagnéticos en la exploración del agua subterránea (*i.e.*, Belmonte-Jiménez *et al.*, 2012; Belmonte-Jiménez *et al.*, 2014) está más extendido en relación a los sísmicos, gravimétricos y magnéticos, el costo, área de estudio y la facilidad tecnológica y operativa, son factores a evaluar para la selección del método a usar (Silva, 1974; Randall-Roberts, 2000; Ernstson, 2006; López-Loera & Tristán-González, 2013; Guevara-Mansilla *et al.*, 2017).

En el caso de México, destacan los estudios para el levantamiento magnético del lago Chapala, Guadalajara (Alatorre-Zamora *et al.*, 2015); en la caracterización geoeléctrica de un sitio contaminado por hidrocarburos en Tabasco (Shevnin *et al.*, 2012); el método electromagnético para caracterizar el acuífero de la Cuenca de México (Arango-Galván *et al.*, 2016) y el acuífero del altiplano de Tula, Tamaulipas (Guevara-Mansilla *et al.*, 2017); la aplicación de métodos magnetométricos y eléctricos para la localización de agua subterránea en ambientes volcánicos áridos de San Luis Potosí (López-Loera, 2014); la potencialidad acuífera del Graben de Villa de Reyes, San Luis Potosí (López-Loera & Tristán-González, 2013); el estudio hidrogeológico de la cuenca de Villa Hidalgo, San Luis Potosí (Pérez-Corona *et al.*, 2017); y el uso de sondeos eléctricos en la identificación de pozos de infiltración para la mitigación de inundaciones en El Barreal, Chihuahua (Dena *et al.*, 2013). Asimismo, destaca el estudio de CONAGUA (2007) sobre el uso de los métodos potenciales en la prospección hidrogeológica e ingeniería de construcción de obras hidráulicas en México. De tal manera, existen distintos trabajos que han utilizado los métodos geofísicos para la exploración y entendimiento de la dinámica y funcionamiento de las aguas subterráneas y problemáticas asociadas en el país.

Desde esta perspectiva, el objetivo principal de este manuscrito es la identificación de zonas con potencial acuífero en la cuenca baja del río Grijalva mediante el análisis magnetométrico. En tal sentido, para responder a este objetivo, el presente trabajo está organizado de la siguiente manera. En primer lugar, se muestra una descripción de la zona de estudio. En segundo, se explica la metodología usada para identificar las áreas con potencial acuífero. En tercer lugar, se presentan los resultados y la discusión. Y finalmente, la conclusión. Sobre esta base se concluye que el estudio realizado puede favorecer no sólo la investigación en estos temas, sino también la reflexión y la toma de decisión de los distintos actores en torno a la protección, gestión, aprovechamiento y planificación de las aguas subterráneas en el país.

ÁREA DE ESTUDIO

El área estudiada se encuentra dentro de la Región Hidrológica Grijalva-Usumacinta Núm. 30 (RH-30), la cual se ubica en la latitud norte 18° 0.106’ y 17° 18.122’ y longitud oeste 92° 52.205’ y 93° 34.427’. El río principal es el Río Grijalva, o Mezcalapa, como es conocido en esta porción de la cuenca Grijalva (Álvarez-Soberano & Medrano-Pérez, 2020). Administrativamente, se localiza en el sector norte del estado de Chiapas cubriendo pequeñas porciones de Tabasco en su parte norte (Figura 1a). Está delimitada por las subcuencas Río Viejo Mezcalapa, Río Mezcalapa, Río Tzimbac, Río Zayula, Río Platanar, Río Paredón, Río Pichucalco (Figura 1b). Posee una superficie de 381.97 km^2, y alberga una población de 340,160 habitantes, según datos del año 2015 del Instituto Nacional de Estadística y Geografía (INEGI). Asimismo, el área de estudio cubre en su totalidad a la delimitación administrativa del acuífero Reforma, y parcialmente, a los acuíferos Samaria-Cunduacán, La Sierra, Huimanguillo, Ocozocoautla (Figura 1c).

El área de estudio se caracteriza por valores de elevación de entre 1 y 2,425 m s. n. m., aunque gran parte de la zona puede considerarse de baja elevación (Figura 1d). En cuanto la geomorfología de la zona de estudio comprende una porción de la Planicie Costera del Golfo en su parte norte, encontrado relieves suaves con lomeríos en cadena orientados preferencialmente en dirección noreste-suroeste y elevaciones que alcanzan poco más de los 300 m s. n. m. La porción sur del área de estudio se caracteriza por una serie de sierras y valles. Esta zona está constituida por las denominadas Montañas del Norte, formando una franja con orientación este-oeste y altitudes que rebasan los 1,500 m s. n. m. (DOF, 20/04/2015). Dentro de esta porción, a unos 20 km al suroeste de Pichucalco, se encuentra el volcán Chichonal y sus rocas volcánicas asociadas (Figura 1e) (Plascencia *et al.*, 2014).

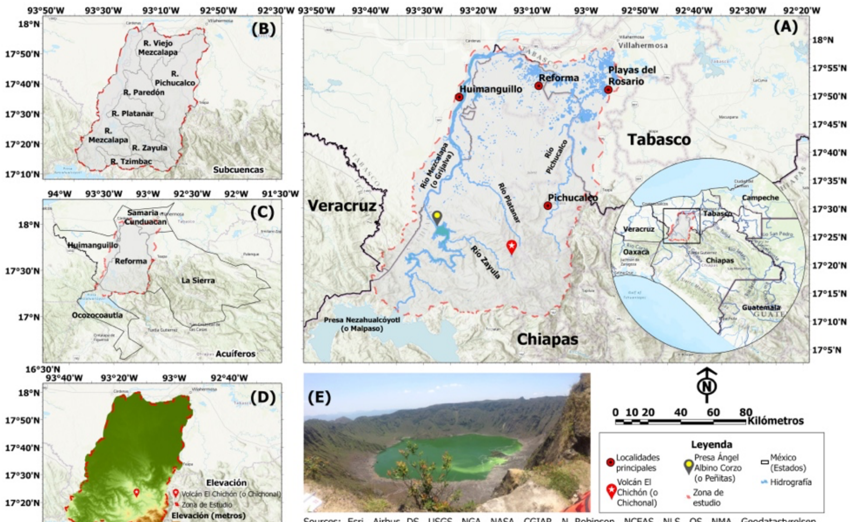

Sources: Esri, Airbus DS, USGS, NGA, NASA, CGIAR, N Robinson, NCEAS, NLS, OS, NMA, Geodatastyrelsen, Rijkswaterstaat, GSA, Geoland, FEMA, Intermap and the GIS user community, Sources: Esri, HERE, Garmin, FAO, NOAA, USGS, © OpenStreetMap contributors, and the GIS User Community, Source: Esri

Figura 1. Área de estudio: a) Ubicación; b) Subcuencas; c) Acuíferos; d) Elevación, y e) Panorámica del volcán El Chichón (o Chichonal).

En tanto que la geología de la zona, al cubrir el acuífero Reforma prácticamente la totalidad del área estudiada, las características geológicas de este acuífero pueden ser representativas para el área estudiada. En la porción sur del área, correspondiente al límite norte de la Sierra de Chiapas, se encuentran aflorando rocas del Cretácico Inferior y Superior surcadas por una serie de fallas y plegamientos, así como sedimentos Terciarios y rocas ígneas extrusivas. Tienen amplia distribución las rocas calizas y les siguen lutitas y areniscas muy intemperizadas, como consecuencia del clima cálido y las altas precipitaciones de esta zona. El resto del área corresponde a depósitos Cuaternarios y a sedimentos miocénicos. La parte principal del acuífero se localiza en la Planicie Costera constituida por depósitos granulares finos con espesores de alrededor de 30 m, cubriendo los sedimentos del Terciario (lutitas y areniscas) que constituyen la Planicie Costera del Golfo. Esta zona se encuentra configurada por una terraza aluvial del Pleistoceno, actualmente fragmentada y muy desgastada, que se eleva sólo pocos metros arriba de la llanura aluvial del Reciente (el Holoceno) e integrada por una composición de canales de ríos activos e inactivos, diques naturales y pantanos secundarios (Plascencia *et al.*, 2014; DOF, 20/04/2015). En general, se muestra la Figura 2 una caracterización geolitológica de mayor detalle sobre el área estudiada.

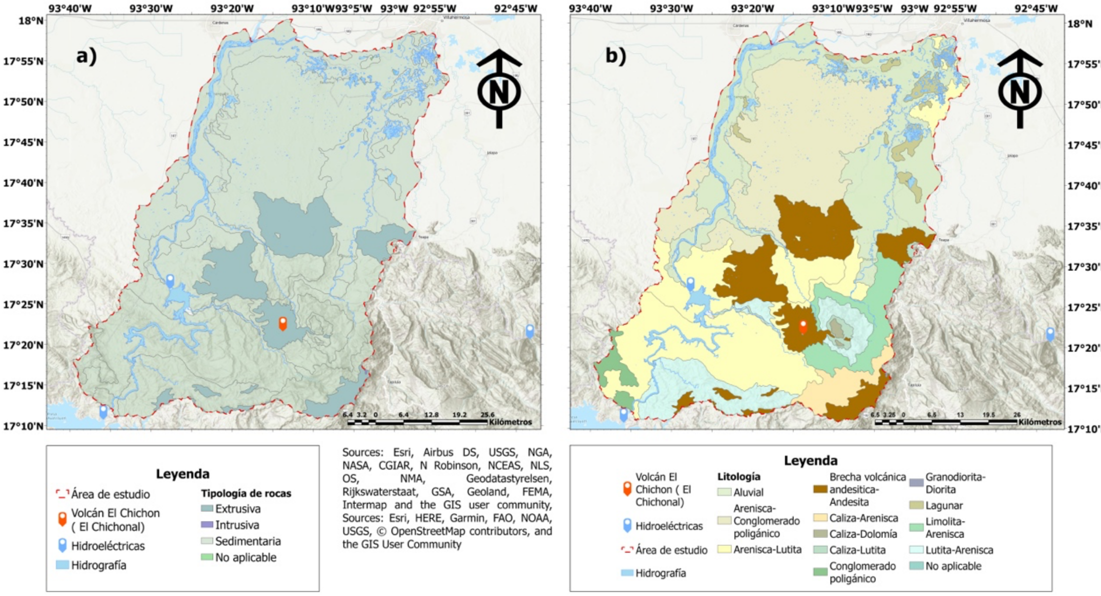

Sources: Esri, Airbus DS, USGS, NGA, NASA, CGIAR, N Robinson, NCEAS, NLS, OS, NMA, Geodatastyrelsen, Rijkswaterstaat, GSA, Geoland, FEMA, Intermap and the GIS user community, Sources: Esri, HERE, Garmin, FAO, NOAA, USGS, © OpenStreetMap contributors, and the GIS User Community

Figura 2. Características geolitológicas del área de estudio: a) tipología de rocas y b) litología.

METODOLOGÍA

Para cumplir con el objetivo propuesto para esta investigación, se llevaron a cabo varias etapas fundamentales (Figura 3). En primer lugar, se realizó una recopilación de información relacionada con la geología de la zona de estudio. Posteriormente, se obtuvo la información aeromagnética de las 9 cartas magnéticas a escala 1:50,000 en el Servicio Geológico Mexicano (SGM) en formato PDF (Pichucalco E15-C29, Reforma E15-C19, Raudales Malpaso E15-C48, Villahermosa E15-D11, Huimanguillo E15-C18, Rómulo Calzada E15-C38, Estación Chontalpa E15-C28, Ixhuatán E15-C39, Tecpatán E15-C49), a las cuales se les aplicaron tratamientos para mejorar la calidad de las imágenes para su posterior digitalización y la delimitación del área de estudio en el sistema de información geográfica *ArcMap*.

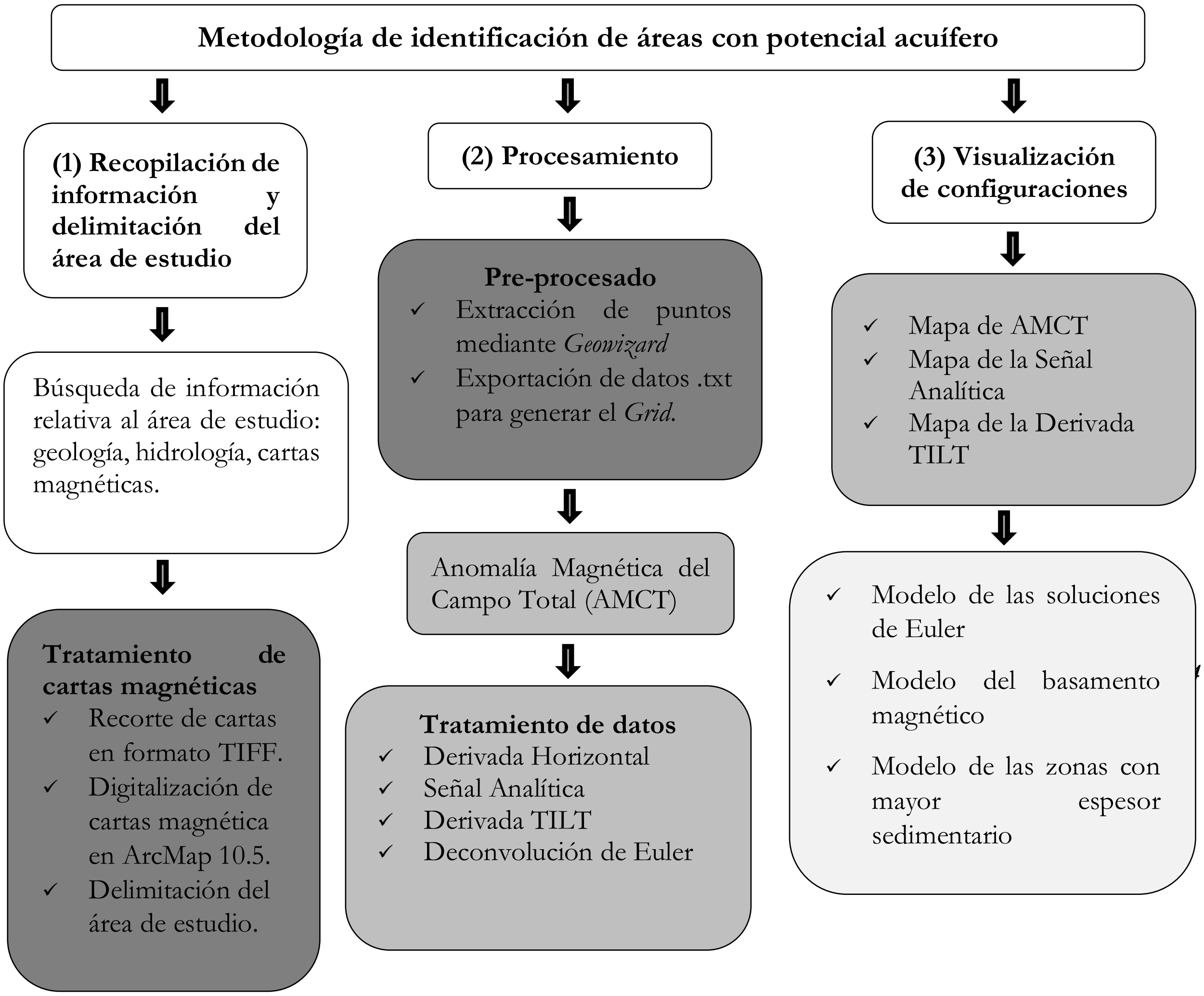

Figura 3. Metodología de identificación de áreas con potencial acuífero. Nota: Servicio Geológico Mexicano (SGM); Anomalía Magnética de Campo Total (AMCT) y TILT (Derivada TILT).

Una vez concluido el proceso de digitalización, se continuó con el preprocesado, el cual consistió en la agrupación de los datos correspondientes a las nueve cartas magnéticas. A continuación, se generó una matriz de datos inicial o *grid* (archivo GRD) que posteriormente se cargó al *software Oasis Montaj,* generando así el mapa de Anomalía Magnética de Campo Total (AMCT). Consecuentemente, se aplicaron diversos filtros o algoritmos matemáticos considerados en la metodología para el procesado de los datos, tal como se muestra en la Tabla 1. Derivado de ello, se obtuvieron los distintos mapas correspondientes a los filtros aplicados, los cuales fueron Anomalía Magnética del Campo Total (AMCT), Señal Analítica y Derivada TILT.

Tabla 1. Algoritmos matemáticos para el tratamiento de datos

Algoritmo matemático	Descripción
Gradiente Horizontal	Técnica principalmente usada para la detección y delimitación de contactos magnéticos, permitiendo aproximar localizaciones horizontales de los bordes de la fuente que produce la anomalía magnética (Roest & Pilkington, 1993; Phillips, 2000).
Señal Analítica	Técnica propuesta por Nabighian (1972) y mejorada por Roest & Pilkington (1992) que es utilizada para delinear los limites o bordes de las fuentes magnéticas, similar al gradiente horizontal, con la diferencia que la SA considera las variaciones verticales del campo magnético, de esta manera siendo útil para inferir la profundidad, localización y geometría de las fuentes.
Derivada TILT	Técnica utilizada para el reconocimiento de la localización horizontal y la extensión de las fuentes, mediante la detección de los bordes de estas. En comparación a otros algoritmos de detección de bordes, esta técnica tiene la ventaja de detectar no solo los bordes de las fuentes someras sino también los bordes de las fuentes profundas (Miller & Singh, 1994).
Deconvolución de Euler	Técnica aplicada por Thompson (1982) para obtener estimaciones de profundidad y localización de fuentes causantes de anomalías magnéticas, así como inferir las tendencias estructurales de dichas fuentes mediante la implementación de un índice estructural correspondiente a un tipo de estructura en particular.

RESULTADOS Y DISCUSIÓN

En el mapa de la anomalía magnética de campo Total (AMCT) mostrado en la Figura 4a, se observa una anomalía con comportamiento dipolar de gran longitud de onda (dimensiones mayores) que se extiende sobre el área de estudio. La parte con valores de tendencia positiva se ubica al norte, y la parte de valores negativos al sur. La dirección principal de las anomalías presentes en esta configuración es NE-SW. Según la distribución de subcuencas hidrográficas en la zona, los bajos magnéticos están enmarcados en ciertas porciones de las subcuencas R. Zayula, R. Pichucalco, R. Tzimbac y R. Platanar, al sureste de la zona de estudio. Cabe señalar que esta zona está asociada al vulcanismo reciente producido por el volcán Chichonal, por lo que las respuestas magnéticas presentes se ven fuertemente afectadas, debido a que las anomalías termales en profundidad afectan la magnetización de las rocas y, por lo tanto, a las anomalías magnéticas observadas en superficie (Carrillo-de la Cruz *et al.*, 2020).

En la zona norte, predomina una anomalía positiva de gran longitud de onda. Esta zona coincide con la porción correspondiente a la Planicie Costera del Golfo, donde encontramos los valores altimétricos más bajos. Superpuestas a estas dos anomalías mayores tenemos una serie de anomalías de dimensiones menores. En la porción central, entre los valores positivos mencionados anteriormente, tenemos una zona caracterizada por un fuerte gradiente con contrastes de valores magnéticos de menor extensión que guardan una dirección preferencial noroeste-sureste (NE-SW). Este comportamiento magnético coincide con una zona de transición entre materiales de cobertura sedimentaría y productos volcánicos. Es en esta región en donde la altimetría del relieve comienza a descender.

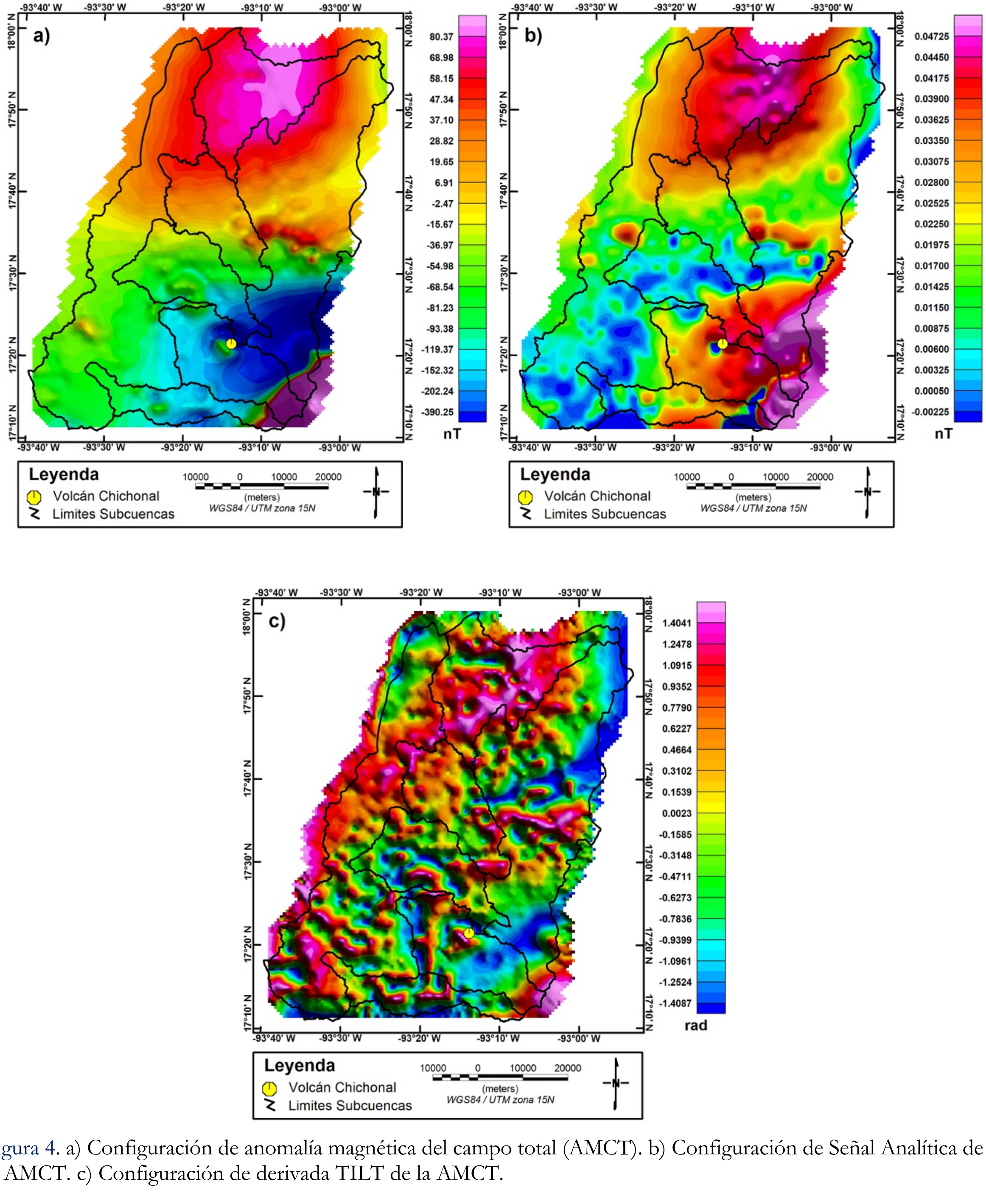

Figura 4. a) Configuración de anomalía magnética del campo total (AMCT). b) Configuración de Señal Analítica de la AMCT. c) Configuración de derivada TILT de la AMCT.

Asimismo, la configuración de la señal analítica de la AMCT (Figura 4b), al igual que la derivada TILT, es una herramienta que delimita gradientes, ayudando a establecer los límites de los cuerpos que originan las anomalías (i.e., Pérez-Corona *et al.*, 2017). De misma forma como en la

AMCT, la dirección principal de las anomalías presentes en esta configuración es NE-SW. El primer alto magnético está ubicado al norte de la zona de estudio, manteniendo el comportamiento suave como se ha mencionado anteriormente. El bajo magnético presente al sureste en la AMCT está ahora representado por valores positivos intermedios. Estas dos anomalías mayores son separadas por un *trend* de bajos magnéticos alienados con dirección suroeste-noreste (NE-SW). Respecto al bajo y alto magnético de la gran anomalía dipolar asociada al volcán Chichonal, estos se encuentran claramente definidos por la señal analítica.

La configuración de la derivada TILT de la AMCT, mostrada en la Figura 4c, indica una serie de lineamientos distribuidos en toda la zona de interés, asociados con fuentes superficiales que en un principio estaban superpuestas a las anomalías de carácter regional, por tal razón es posible observar una mayor cantidad de fuentes magnéticas de menor tamaño. Al igual que en las configuraciones anteriores, la dirección principal de las anomalías presentes en esta configuración es NE-SW. Nótese que las repuestas magnéticas muestran tendencias lineales, por lo que pueden representar características estructurales de interés hídrico (zonas de fallas y/o fracturas), puesto que se trata de un algoritmo matemático útil para la detección de contactos entre cuerpos magnéticos, debido a su naturaleza. Respecto a la zona sur, se observan una serie de altos magnéticos con dirección preferencial NE-SW distribuidos por toda la región, los cuales no presentan un interés hídrico debido a que estas respuestas coinciden con la zona con relieves más altos que corresponden a las denominadas Montañas del Norte. Estos rasgos se mantienen presentes hasta la parte central de la zona estudiada, punto a partir del cual la altimetría del relieve comienza a descender. Asimismo, se muestra un alto magnético de dimensiones considerables en la zona norte con dirección NE-SW, sobre la cual se encuentran superpuestas una serie de anomalías de dimensiones menores. Esta zona corresponde al área de mayor interés o potencial acuífero debido a que se encuentra en la porción de menores valores altimétricos, estando influenciada por los escurrimientos de agua provenientes de las partes altas en la zona estudiada. Como se observa en la Figura 4c, la derivada TILT también enfatiza los límites del alto magnético de la anomalía dipolar asociada con el volcán Chichonal.

Según Padilla y Sánchez (2007), las rocas de la zona de estudio se encuentran afectada por una serie de rasgos estructurarles (pliegues y fallas) producto de los procesos geológicos que configuraron la geología de la zona de estudio y sus alrededores. Estos rasgos estructurales distribuidos tienen una dirección preferencial NE-SW. Como ya me menciono, las anomalías presentes en las 3 configuraciones mostradas en la Figura 4 presentan principalmente direcciones NE-SW, mostrando una fuerte relación con los rasgos estructurales propuestos por Padilla y Sánchez (2007). En concreto, los valores de tendencia positiva distribuidos particularmente al norte de la zona de estudio se encuentran presentes en las tres configuraciones obtenidas (Figura 4). En este sentido, el alto magnético sobresaliente en todas las configuraciones podría estar asociado con un anticlinal.

En relación con la construcción del modelo magnético en la zona estudiada, se aplicó la Deconvolución de Euler (DE) para los índices estructurales 0.5, 1.0, 1.5, 2.0, 2.5 y 3.0 utilizado una ventana de 9x9 datos, y así obtener los rasgos de profundidad asociados a cambios en la geometría de la distribución de los materiales magnéticos que constituyen la base para la construcción del modelo magnético (Figura 5). Todas las soluciones obtenidas con la DE fueron integradas a una misma base de datos. Posteriormente se interpolaron estos valores utilizando el método de vecinos cercanos en el software *Voxler 4.1*, esto con el objetivo de integrar la respuesta de una fuente magnética equivalente asociada a la capa de roca magnética, que constituye el basamento cristalino impermeable. El uso de un solo índice estructural solo proyecta una parte de la estructura, así que al interpolar las soluciones se genera una imagen que muestra la distribución de estas fuentes magnéticas (Figura 5).

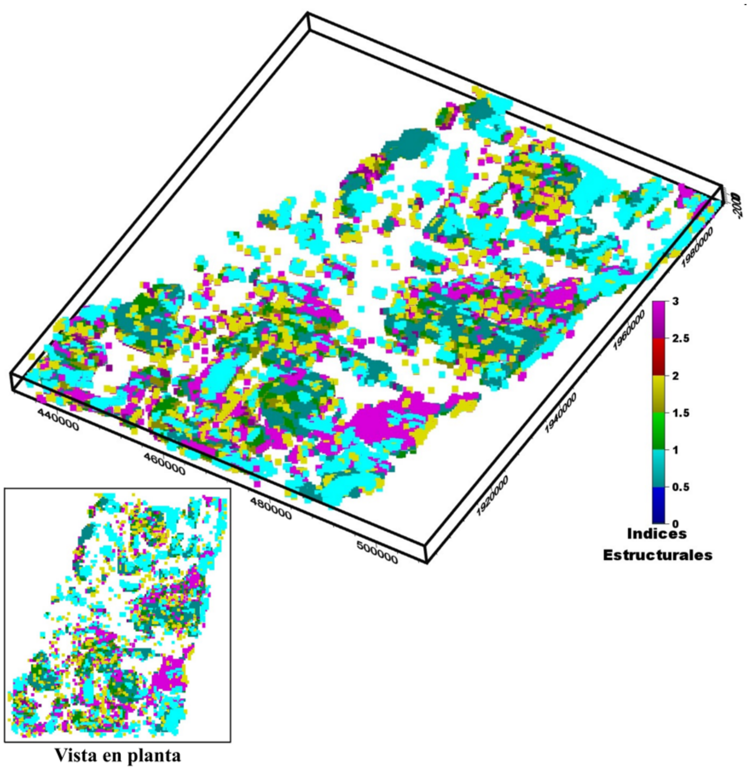

Figura 5. Visualización 3D de las soluciones de la Deconvolución de Euler para los índices estructurales. Nota: 0.5 (Azul marino), 1.0 (Azul celeste), 1.5 (Verde), 2.0 (Amarillo), 2.5 (Rojo) y 3.0 (Morado). Las zonas en blanco en el área estudiada corresponden a las porciones en donde no tienen soluciones de Euler. En la porción inferior izquierda se muestra la vista en planta de los resultados.

Una vez interpoladas las soluciones, se realizó un proceso de asociación o conexión de fuentes para ayudar visualmente a resaltar la presencia de materiales magnéticos asociados al basamento, contrayendo así un modelo tridimensional (Figura 6, 7a). En las Figuras 7b y 8a, las áreas iluminadas en color azul corresponden a zonas en donde no se encontró una fuente magnética equivalente dentro de la dispersión en la interpolación. Estas zonas son asociadas a espesores de paquetes sedimentarios presentes en la zona de estudio y representan las posibles zonas con mayor potencial para el almacenamiento de fluidos. Los colores oscuros se asocian a la delimitación de lo que suponemos es el basamento magnético. Cabe señalar que estos espesores alcanzan profundidades mayores a los 3,000 metros en esta zona. Asimismo, la Figura 8b corresponde a la superposición de las zonas constituidas por espesores sedimentarios junto con los escurrimientos de las regiones topográficamente más altas, pudiéndose apreciar una buena correlación entre estos dos. En este sentido, se puede observar cómo los escurrimientos provenientes de las partes más altas (sur de la zona estudiada) desembocan en las zonas de espesor sedimentario más profundo (centro y norte de la zona estudiada). Por tanto, se puede inferir, con fundamento en la altimetría y la magnetometría, que la parte central-norte del área estudiada alberga zonas de potencial acuífero.

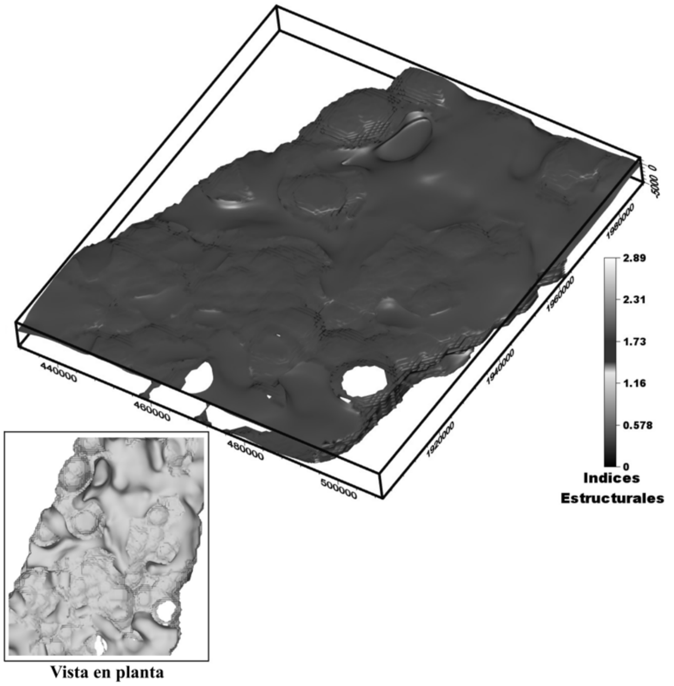

Figura 6. Visualización 3D del modelo del basamento obtenido a través de la interpolación de las soluciones de Euler. Nota: En la porción inferior izquierda se muestra la vista en planta de los resultados.

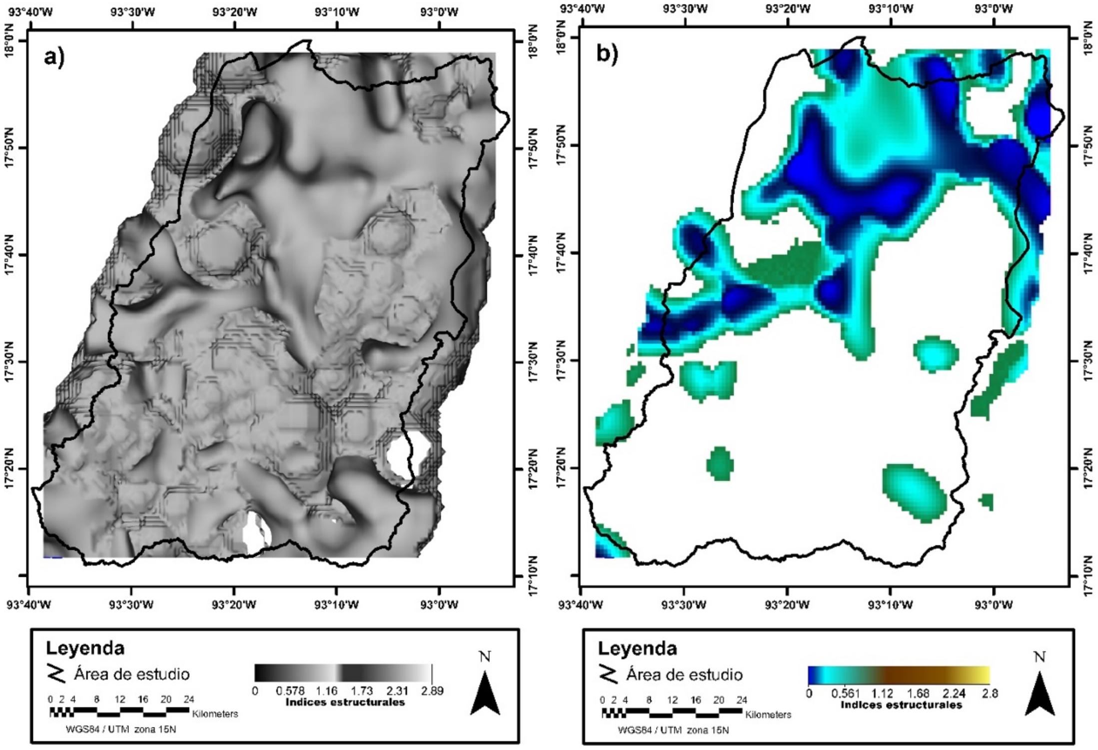

Figura 7. a) Modelo de basamento correspondiente a la zona de estudio (obtenido al interpolar los índices estructurales); b) Zonas de mayor espesor sedimentario (obtenido al interpolar los índices estructurales). Nota: Las barras de colores para a) y b) representan los valores de los índices estructurales interpolados.

Esta zona presenta una compleja evolución sedimentológica y tectónica, pasando de facies carbonatadas del Jurásico-Cretácico a secuencias siliclásticas del Terciario con una gran aportación de sedimentos arenosos con espesores que alcanzan hasta los 6,000 metros hacia la zona costera y que son derivados de la erosión de las zonas continentales altas (Velázquez-Aguirre & Ordaz-Ayala, 1993; Padilla y Sánchez, 2007). El promedio de la elevación del nivel estático, con base en la red piezométrica de la Comisión Nacional del Agua (CONAGUA), es de 12 m s. n. m. y corresponde a flujos intermedios. Interactuando con la superficie se identifican flujos subterráneos locales en zonas focalizadas de altos topográficos que funcionan como zonas locales de infiltración. Se considera un acuífero libre de buena permeabilidad. En un registro geofísico de un pozo en Cunduacán, Tabasco se interpreta que el acuífero presenta buenas propiedades en una secuencia alternante de arenas, arcillas y limos, donde a partir de los 150-250 metros de profundidad registrados existen capas de arena gruesa, arcillas, y arena media con diferentes espesores (Aurora Geofísica, 2016).

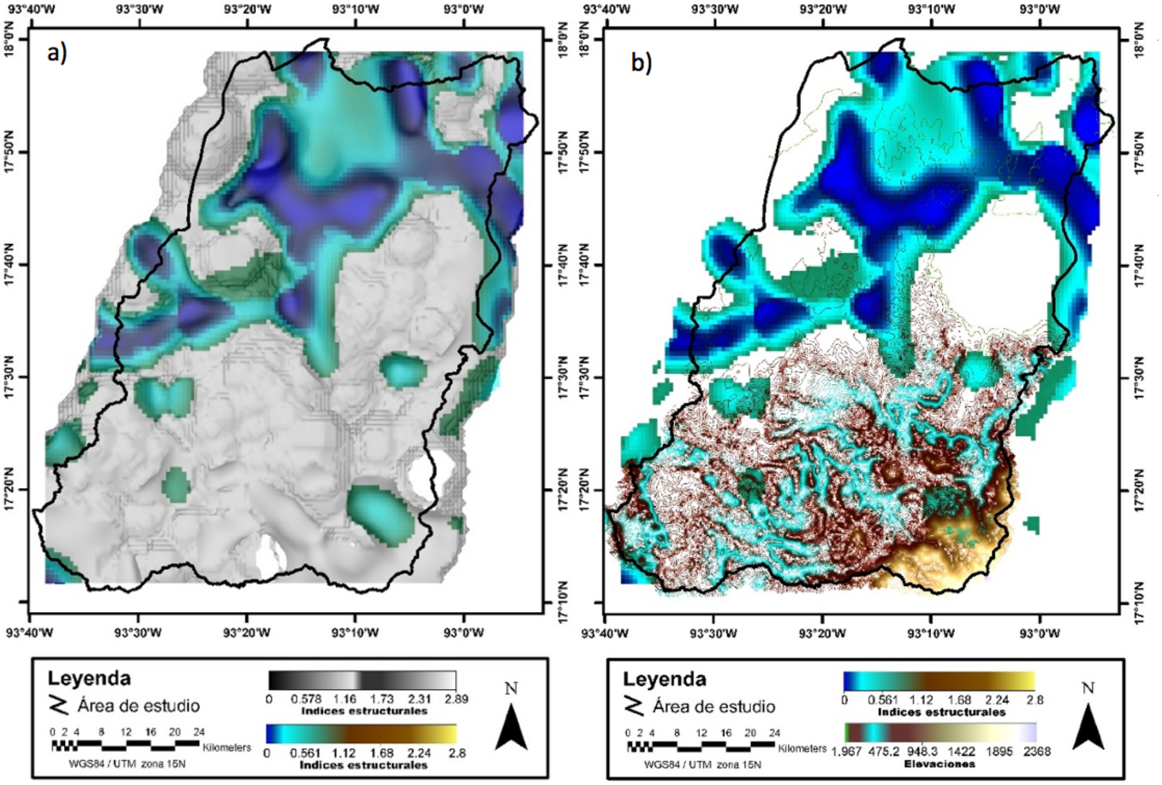

Figura 8. a) Superposición del modelo de basamento y las soluciones correspondientes a las zonas de mayor espesor sedimentario; b) Superposición de las zonas de mayor espesor sedimentario y los escurrimientos potenciales provenientes de las partes más altas [m].

En este contexto, la zona de estudio se encuentra ubicada principalmente en la provincia hidrogeológica Sierras y Valles del Sureste, donde predominan altos niveles de precipitación y riqueza hídrica superficial de abundantes caudales (Grijalva y Usumacinta), siendo las zonas bajas las receptoras de los escurrimientos superficiales y del almacenamiento subterráneo proveniente de las zonas altas (Velázquez-Aguirre & Ordaz-Ayala,1993). A todo ello, respecto a la litología mostrada previamente, el área de estudio se caracteriza por materiales permeables y de alta infiltración, destacando la arenisca-lutita en la parte alta de la zona chiapaneca y una llanura de materiales aluviales en la parte baja del estado de Tabasco.

Con base en los resultados mostrados se evidencia que el método magnetométrico identifica las zonas potenciales acuíferas regionales, por lo que para una mejor caracterización de los acuíferos se recomienda se realicen otros estudios geofísicos como gravimetría y el método transitorio electromagnético para poder corroborar los espesores sedimentarios y el potencial hídrico en la zona, así como una testificación de las zonas con notables características de almacenamiento para un control estratigráfico y para fines de explotación sostenible del agua subterránea de los acuíferos regionales de la zona.

Adicionalmente, cabe señalar que, según datos a febrero 2019 del Registro Público de Derechos de Agua (REPDA) de la CONAGUA, en la zona de estudio se tienen otorgadas 273 concesiones de agua con un volumen total de 62.2 hectómetros cúbicos/año, concentradas fundamentalmente en la agricultura (34%), industria (41%), y tan solo un 15.4% en abastecimiento doméstico. Asimismo, estas concesiones se encuentran ubicadas en el área media-baja de la zona de estudio (Figura 9), por lo que los resultados de la presente investigación confirman la idoneidad de la metodología usada para el análisis de las aguas subterráneas, así como para la identificación preliminar de áreas y estructuras geológicas que podrían albergar un potencial acuífero a nivel cuenca.

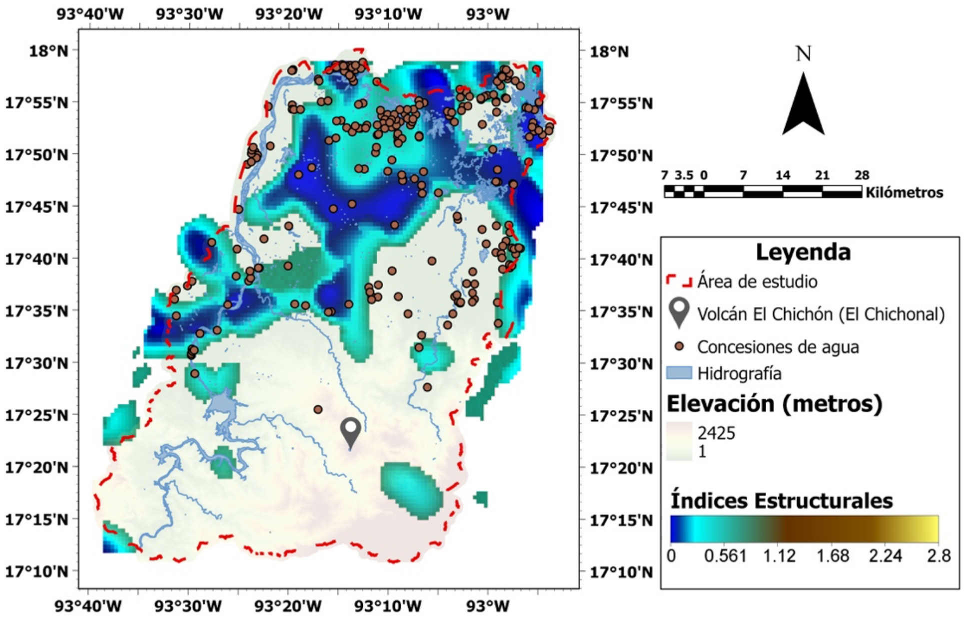

Figura 9. Concesiones de agua en el área de estudio (REPDA-CONAGUA) y las zonas de mayor espesor sedimentario.

Desde esa perspectiva, y teniendo en cuenta los resultados obtenidos, el uso de la magnetometría puede ser clave en la delineación de los rasgos estructurales de las rocas (fallas, intrusiones o la morfología) que configuran a los acuíferos. No obstante, la aplicación geohidrológica de las técnicas magnetométricas no se encuentran muy extendidas en México, fundamentalmente por dos razones: 1) Se trata de un método auxiliar o complementario a otros más determinativos para la detección de rocas que albergan agua y 2) Por el mayor grado de difusión que poseen otros métodos geofísicos, como los eléctricos, en los estudios geohidrológicos (CONAGUA, 2007). Por tanto, más allá de las diferencias entre los métodos geofísicos, la fortaleza de los métodos magnetométricos radica en que permiten analizar grandes superficies, y, por ende, reducir el costo para el uso de sondeos eléctricos verticales (SEV's) en áreas específicas, teniendo así un conocimiento previo sobre las unidades de rocas que contienen acuífero en la zona estudiada. De tal manera, podrían utilizarse como método complementario en el análisis y conocimiento de las aguas subterráneas.

En tal sentido, los resultados obtenidos en la presente investigación puede representar una herramienta preliminar y de bajo coste para el análisis y conocimiento de las aguas subterráneas, así como para la toma de decisión en torno al ordenamiento, protección y manejo territorial de áreas específicas de las cuencas hidrológicas, con la finalidad, entre otras cosas, de garantizar eventuales o futuras fuentes para el abastecimiento de agua ante la ocurrencia de eventos climáticos extremos y contaminación de las actuales, respectivamente. Por tanto, los resultados de este trabajo se enmarcan como una contribución en esa dirección.

CONCLUSIÓN

Los resultados muestran las características y rasgos sobresalientes de las principales fuentes magnéticas que fueron interpretados de las diferentes configuraciones obtenidas al aplicar a los datos los algoritmos matemáticos propuestos. Aunado a lo anterior, el análisis del modelo 3D del basamento magnético construido, confirman que el método magnetométrico representa una herramienta factible para la identificación preliminar de zonas constituidas por unidades rocosas con posible potencial acuífero, siendo este el caso para la zona considerada en esta investigación. En la zona de estudio cabe destacar dos puntos importantes:

1) Los resultados obtenidos por la derivada TILD muestran una serie de altos magnéticos de distinta naturaleza, siendo los de mayor importancia aquellos distribuidos en la región norte. Estos muestran una dirección preferencial NE-SW y rasgos estructurales de interés hídrico observados en las anomalías positivas de menores dimensiones, los cuales pueden representar contactos entre cuerpos magnéticos traducidos como zonas de fallamiento y/o fracturas; y
2) Los escurrimientos provenientes de las partes más altas, al sur de la zona estudiada, descargan en las zonas de espesor sedimentario más profundo, al centro y norte de la zona estudiada, sugiriendo la presencia de zonas con potencial acuífero.

No obstante, para un mayor detalle y conocimiento de la profundidad de la zona de estudio se requiere la aplicación complementaria de métodos más resolutivos que indiquen la presencia del recurso hídrico, como los sondeos eléctricos verticales (SEV's). Por tanto, la metodología aplicada podría reducir los costos asociados a la planeación de campañas de exploración por métodos directos e indirectos. En tal sentido, la presente investigación es un aporte al conocimiento y comprensión de las aguas subterráneas, y a su vez, una contribución para la toma de decisiones en los temas geohidrológicos, ordenamiento territorial, protección y conservación del recurso agua, y las políticas públicas asociadas.

AGRADECIMIENTOS

Los autores agradecen al Centro del Cambio Global y la Sustentabilidad, A.C. (CCGS) por las facilidades durante la realización de esta investigación. Además de expresar su agradecimiento a los revisores anónimos por sus comentarios y recomendaciones en la mejora de esta investigación. ORMP también desea agradecer al programa Cátedra-CONACYT y al proyecto Cátedras-CCGS no. 963 "Hacia un manejo sustentable del agua en el sureste de México y áreas adyacentes de Centroamérica".

REFERENCIAS

Alatorre-Zamora, M., Campos-Enríquez, J., Rosas-Elguera, J., Peña-García, L., Maciel-Flores, R., & Fregoso-Becerra, E. (2015). Chapala half-graben structure inferred. A magnetometric study. *Geofísica Internacional*, 54(4). doi: http://dx.doi.org/10.22201/igeof.00167169p.2015.54.4.1699

Alatorre-Zamora, M., Rosas-Elguera, J., Pérez-Rodríguez, G., Campos-Enríquez, J., & Maciel-Flores, R. (2012). Contribución de la deconvolución de Euler y la señal analítica en 3D al análisis de riesgos por fallas en el graben de valle de banderas. *e-Gnosis*, 10, 1-31. Recuperado el 12 de julio de 2019, en: http://www.redalyc.org/articulo.oa?id=73026905001

Allred, B., Daniels, J. J., & Ehsani, M. R. (2008). Handbook of Agricultural Geophysics, 432 pp., CRC Press, Boca Raton, Florida, USA.

Álvarez-Soberano, A., & Medrano-Pérez, O. R. (2020). Caracterización geomorfológica de la subcuenca río Mezcalapa, región hidrológica Grijalva-Usumacinta (RH-30) en sureste de México. *Investigación y Ciencia de la Universidad Autónoma de Aguascalientes*, 28(80), 32-44. doi: https://doi.org/10.33064/iycuaa2020803002

Arango-Galván, C., Flores-Márquez, E., Hernández-Espriú, A., Arias-Paz, A., & Sagahón-López, E. (2016). Shallow geoelectrical characterization of a small portion of the Basin of Mexico aquifer: Towards a better resource management. *Geofísica Internacional*, 55(3). doi: http://dx.doi.org/10.22201/igeof.00167169p.2016.55.3.1723

Aurora Geofísica. (2016). Registro geofísico de pozos. (Reporte técnico consultoría).

Belmonte-Jiménez, S.I., Bortolotti-Villalobos, A., Campos-Enríquez, J.O., Pérez-Flores, M.A., Delgado-Rodríguez, O., & M. d. L. A. Ladrón de Guevara-Torres. (2014). Electromagneti methods for characterizing a site contaminated by leacheates. *Revista Internacional de Contaminación Ambiental*, 30(2), 317-329.

Belmonte-Jiménez, S.I., Jiménez-Castañeda, M.E., Pérez-Flores, M.A., Campos-Enríquez, J.O., López-Reyes, J.A., & L. Salazar-Peña. (2012). Characterizing of a leachate contaminated site integrating geophysical and hydrogeological information. *Geofísica Internacional*, 51(4), 309-321. DOI: http://dx.doi.org/10.22201/igeof.00167169p.2012.51.4.1228

Binley, A., Hubbard, S. S., Huisman, J. A., Revil, A., Robinson, D. A., Singha, K., & Slater, L. D. (2015). The emergence of hydrogeophysics for improved understanding of subsurface processes over multiple scales. *Water Resources Research*. 51, 3837–3866. doi:10.1002/ 2015WR017016.

Brocca, L., Ciabatta, L., Massari, C., Camici, S., & Tarpanelli, A. (2017). Soil Moisture for Hydrological Applications: Open Questions and New Opportunities. *Water*, 9(2), 140. doi: https://doi.org/10.3390/w9020140

Campos-Enríquez, J.O., Delgado-Rodríguez, O., Chávez-Segura, R., Gómez-Contreras, P., Flores-Márquez, E.L., and F.S. Birch. (1997). The subsurface structure of the Chalco sub-basin (Mexico City) inferred from geophysical data. *Geophysics*, 62, 23-35. DOI: http://dx.doi.org/10.1190/1.1444123

Campos-Enríquez, J.O., Flores-Márquez, E.L., and R. Chávez. (1997). Geophysical characterization of hydrogeologic systems. *The Leading Edge*, 16(12), 1,769-1,773. DOI: https://doi.org/10.1190/1.1437576

Carrillo-de la Cruz, J. L., Prol-Ledesma, R. M., Gómez-Rodríguez, D., & Rodríguez-Díaz, A. A. (2020). Analysis of the relation between bottom hole temperature data and Curie temperature depth to calculate geothermal gradient and heat flow in Coahuila, Mexico. *Tectonophysics*, 228397. DOI: https://doi.org/10.1016/j.tecto.2020.228397

CONAGUA (Comisión Nacional del Agua). (2018). Atlas del Agua en México. Comisión Nacional del Agua, Secretaría de Medio Ambiente y Recursos Naturales. Ciudad de México, México. Recuperado el 04 de julio de 2019. Disponible en: https://agua.org.mx/wp-content/uploads/2019/04/AAM_2018.pdf

_______. (2007). Manual de agua potable, alcantarillado y saneamiento. Exploración gravimétrica y magnetométrica. Secretaría de Medio Ambiente y Recursos Naturales (Editor). México.

Cortés F.I.A., Pérez M.L., & Mogollón H.M. (2012). Mexico's Water Challenges for the 21st Century. In: Oswald Spring Ú. (Eds.), *Water Resources in Mexico* (pp. 21-38). Hexagon Series on Human and Environmental Security and Peace, vol. 7. Springer, Berlin, Heidelberg.

Dena O., O., C., G., Leyva, J., Domínguez A., M., Rascon., E., Gómez, F., & Doser., D. (2013). Uso de métodos geofísicos subsuperficiales en el control de inundaciones: un estudio de resistividad para definir la capacidad de almacenamiento subterráneo de un cuerpo de arena en Ciudad Juárez, México. *Geofísica Internacional*, 51 (3). doi: http://dx.doi.org/10.22201/igeof.00167169p.2012.51.3.1194

DOF (Diario Oficial de la Federación). (20/04/2015). Actualización de la disponibilidad media anual de agua en el acuífero Reforma (0702), Estado de Chiapas. Publicado en el Diario Oficial de la Federación en fecha 20 de abril de 2015. Recuperado el 17 de julio de 2019, en https://www.gob.mx/cms/uploads/attachment/file/102903/DR_0702.pdf

Ernstson, K. (2006). Magnetic, geothermal, and radioactivity methods. In: Kirsch R. (eds.), *Groundwater Geophysics* (pp. 275-294). Springer, Berlin, Heidelberg. doi: https://doi.org/10.1007/3-540-29387-6_9

ESRI. (2019). ArcGIS and ArcMap (*ArcMap 10.5*). Software Esri. Disponible en: www.esri.com

ESRI. (2020). ArcGIS Pro. Software Esri. Disponible en: https://www.esri.com/es-es/arcgis/products/arcgis-pro/overview

Flores-Márquez, E.L., Campos-Enríquez, J.O., Chávez-Segura, R. and J.A. Castro-García. (1998). Saltwater intrusión of the Costa de Hermosillo aquifer, Sonora, Mexico: A numerical simulation. *Geofísica Internacional*, 37(3). DOI: http://dx.doi.org/10.22201/igeof.00167169p.1998.37.3.392

Florsch, N., Muhlach, F., & Kammenthaler, M. (Eds.). (2019). Everyday Applied Geophysics 2: Electromagnetics and Magnetics. ISTE Press - Elsevier. doi: https://doi.org/10.1016/C2017-0-01434-9

GEOSOFT. (2019). Oasis Montaj (software: versión 8.4). Visit: www.geosoft.com

Golden Software. (2019). Voxler (software: versión 4.1). Visit: www.goldensoftware.com

Guevara-Mansilla, Ó., Ventura-Houle, R., & Andrade-Limas, E. (2017). Uso de sondeos electromagnéticos en la caracterización hidrológica del acuífero del altiplano de Tula, Tamaulipas. *Investigación y Ciencia*, 25 (70), 23-30. Recuperado en 11 de julio de 2019, de http://www.redalyc.org/articulo.oa?id=67451351003

Hatch-Kuri, G. (2017). El agua subterránea en México: retos y pendientes para la transformación de su gestión. En Christian Denzin, Federico Taboada y Raúl Pacheco-Vega (Eds.), *El agua en México. Actores, sectores y paradigmas para una transformación social-ecológica* (pp. 149-170). Friedrich-Ebert-Stiftung, Proyecto Regional Transformación Social-Ecológica. Consultado el 1 de julio de 2019. http://library.fes.de/pdf-files/bueros/mexiko/14377.pdf

Henderson, R. J. (1992). Urban Geophysics — A Review. *Exploration Geophysics*, 23:4, 531-542. doi: 10.1071/EG992531

Hubbard, S. & Rubin, Y. (2005). Chap. 1. Introduction to hydrogeophysics. In Y. Rubin and S. Hubbardin (eds.), *Hydrogeophysics* (pp. 3 – 23). Springer, New York.

Huizar-Álvarez, R., Campos-Enríquez, J.O., Lermo-Samaniego, J.F., Delgado-Rodríguez, O. and A. Huidobro-González. (1977). Geophysical and hydrogeological characterization of the sub-basins of Apan and Tochac (Mexico Basin). *Geofísica Internacional*, 36(4), 217-233.

JAXA/METI ALOS PALSAR L 2011. Accessed through ASF DAAC 11 July 2019.

Kirsch, R. (Ed.). (2009). Groundwater geophysics a tool for hydrogeology. 2nd Ed. Springer-Verlag Berlin Heidelberg, Berlin.

López-Morales, C. A. (2017). El estado del agua en México: retos, oportunidades y perspectivas. En Christian Denzin, Federico Taboada y Raúl Pacheco-Vega (Eds.), *El agua en México. Actores, sectores y paradigmas para una transformación social-ecológica* (pp. 13-42). Friedrich-Ebert-Stiftung, Proyecto Regional Transformación Social-Ecológica. Consultado el 1 de julio de 2019. http://library.fes.de/pdf-files/bueros/mexiko/14377.pdf

López-Loera, H., & Tristán-González, M. (2013). Geología y magnetometría aérea del Graben de Villa de Reyes, San Luis Potosí, Mesa Central de México: implicaciones tectónicas y geohidrológicas. *Boletín de la Sociedad Geológica Mexicana*, *65*(1), pp. 137-156. Recuperado en 11 de julio de 2019, de http://www.scielo.org.mx/scielo.php?script=sci_arttext&pid=S1405-33222013000100012&lng=es&tlng=es.

López-Loera, H. (2014). Geofísica para la localización de Agua Subterránea en Ambientes Volcánicos Áridos de la Mesa Central. Caso La Dulcita, Villa de Ramos, San Luis Potosí, México. *Boletín de la Sociedad Geológica Mexicana*, 66 (1), pp. 165-181.

Miller, H. G. & Singh, V. (1994). Potential field tilt - a new concept for location of potential field sources. *Journal of Applied Geophysics*, 32 (2–3): 213-217. doi: https://doi.org/10.1016/0926-9851(94)90022-1

Nabighian, M. N. (1972). The analitic signal of two- dimensional magnetic bodies with polygonal cross-section: its properties and use for automated anomaly interpretation. *Geophysics*, 37 (3), 507-517. doi: https://doi.org/10.1190/1.1440276

Ndougsa-Mbarga, T., Manguelle-Dicoum, E., & Campos-Enríquez, J. (2010). Gravity anomalies, sub-surface structure and oil and gas migration in the Mamfe, Cameroon-Nigeria, sedimentary basin. *Geofísica Internacional*, 46(2). doi: http://dx.doi.org/10.22201/igeof.00167169p.2007.46.2.22

Ojeda-Olivares, E. A., Sandoval-Torres, S., Belmonte-Jiménez, S., Campos-Enríquez, J.O., Zignol, F., Reygadas, Y., & J. Tiefenbaher. (2019). Climate Change, land use/land cover change, and population growth as drivers of groundwater depletion in the central valleys, Oaxaca, Mexico. *Remote Sensing*, 11(11),1290. DOI: https://doi.org/10.3390/rs11111290

Padilla y Sánchez, R. J. (2007). Evolución geológica del sureste mexicano desde el Mesozoico al presente en el contexto regional del Golfo de México. *Boletín de la Sociedad Geológica Mexicana*, *59*(1), 19–42. doi: https://doi.org/10.18268/bsgm2007v59n1a3

Peñuela-Arévalo, L., & Carrillo Rivera, J. (2013). Definición de zonas de recarga y descarga de agua subterránea a partir de indicadores superficiales: Centro-Sur de la Mesa Central, México. *Investigaciones Geográficas, 0*(81), pp. 11-32. doi: http://dx.doi.org/10.14350/rig.30518

Pérez-Corona, F., López-Loera, H., Fregoso-Becerra, E., Yutsis, V., Martínez-Ruíz, V., & Dávila-Harris, P. (2017). Caracterización de lineamientos estructurales y sus implicaciones hidrogeológicas en la cuenca de Villa Hidalgo (San Luis Potosí) integrando métodos geofísicos potenciales. *Boletín de la Sociedad Geológica Mexicana*, 69 (3), 555-576. Recuperado en 11 de julio de 2019, de http://www.redalyc.org/articulo.oa?id=94353719003

Phillips, J. D. (2000). Locating magnetic contacts: a comparison of the horizontal gradient, analytic signal, and local wavenumber methods. *Proceedings 70th Annual International Meeting, Society of Exploration Geophysics*, Expanded Abstracts, 402-405. Calgary. doi: https://doi.org/10.1190/1.1816078

Plascencia, H., González-Espinosa, M., Ramírez-Marcial, N., Álvarez-Solís, D., & Musalem, K. (2014). Características físico-bióticas de la cuenca del río Grijalva. En: González-Espinosa M., Brunel-Manse M. C. (Eds.), *Montañas, pueblos y agua: dimensiones y realidades de la cuenca Grijalva* (pp: 29-79). Editorial Juan Pablos. México.

Randall-Roberts, J. A. (2000). Métodos alternos de geofísica en la búsqueda de agua subterránea In: 1st Joint World Congress On Groundwater, 2000, Fortaleza. Anais do 1st Joint World Congress on Groundwater. *Revista Águas Subterrâneas*, v.1. Recuperado en 12 de julio de 2019, de https://aguassubterraneas.abas.org/asubterraneas/article/view/24307

Reynolds, J.M. (2011). An Introduction to Applied and Environmental Geophysics, 2nd edition. John Wiley & Sons, England.

Registro Público de Derecho de Agua (REPDA). 2019. Consulta la base de datos del REPDA. Comisión Nacional del Agua (CONAGUA). México. Disponible en: https://app.conagua.gob.mx/consultarepda.aspx

Robinson, D. A., Binley, A., Crook, N., Day-Lewis, F. D., Ferré, T. P. A., Grauch, V. J. S., Knight, R., Knoll, M., Lakshmi, V., Miller, R. Nyquist, J., Pellerin, L., & Singha, K. (2008). Advancing process-based watershed hydrological research using near-surface geophysics: a vision for, and review of, electrical and magnetic geophysical methods. *Hydrological Processes*, 22/18, pp. 3604 - 3635. doi: https://doi.org/10.1002/hyp.6963

Roest, W.E., Verhoef, J., & Pilkington, M. (1992). Magnetic interpretation using 3-D analytic signal. *Geophysics*, 57, 116-125. doi: https://doi.org/10.1190/1.1443174

Roest, W. R. & Pilkington, M., (1993). Identifying remanent magnetization effects in magnetic data. *Geophysics*, 58 (5): 653-659. doi: https://doi.org/10.1190/1.1443449

Romero-Ruiz, A., Linde, N., Keller, T., & Or., D. (2018). A review of geophysical methods for soil structure characterization. *Reviews of Geophysics*, 56. doi: https://doi.org/10.1029/2018RG000611

Shevnin, V., Delgado-Rodríguez, O., Fernández-Linares, L., Zegarra-Martínez, H., Mousatov, A., & Ryjov, A. (2012). Geoelectrical characterization of an oil-contaminated site in Tabasco, Mexico. *Geofísica Internacional*, 44(3). doi: http://dx.doi.org/10.22201/igeof.00167169p.2005.44.3.197

Silva, L. I. (1974). Criterios usados en la selección de los métodos geofísicos de prospección. *Revista geológica de Chile: An international journal on andean geology*. ISSN-e 0717-618X, ISSN 0716-0208, Nº. 1, 1974, págs. 37-63.

Spring, Ú.O. & Cohen, I.S. (2012). Water Resources in Mexico: A Conceptual Introduction. In: Oswald Spring Ú. (Eds.), *Water Resources in Mexico* (pp. 5-17). Hexagon Series on Human and Environmental Security and Peace, vol. 7. Springer, Berlin, Heidelberg.

Thompson, D. T. (1982). EULDPH: A new technique for making computer-assisted depth estimates from magnetic data. *Geophysics*, 47(1), 31–37. doi:10.1190/1.1441278

Tinivella, U., Giustiniani, M., & Cassiani, G. (2013). Geophysical Methods for Environmental Studies. *International Journal of Geophysics*, vol. 2013, Article ID 950353, 2 pages, 2013. doi: https://doi.org/10.1155/2013/950353.

Velázquez-Aguirre, L. & Ordaz-Ayala, A. (1993). Provincias Hidrogeológicas de México. *Boletín de la Sociedad Geológica Mexicana*, 52(1-2), pp. 15-33. doi: http://dx.doi.org/10.18268/BSGM1993v52n1a3

Vereecken, H., Binley, A., Cassiani, G., Revil, A., & Titov, K. (Eds.). (2006). Applied Hydrogeophysics. First edition, Springer Netherlands.